FEDERAL UNIVERSITY OF TECHNOLOGY - PARANÁ
POSTGRADUATE PROGRAM IN MECHANICAL AND MATERIALS ENGINEERING

ANGEL DE JESUS RIVERA JIMENEZ

VISUALIZAÇÃO DO REINICIO DE ESCOAMENTO DE MATERIAIS VISCOPLÁSTICOS EM TUBOS HORIZONTAIS USANDO VELOCIMETRIA POR IMAGEM DE PARTÍCULAS

Dissertation

CURITIBA
2021

ANGEL DE JESUS RIVERA JIMENEZ

VISUALIZAÇÃO DO REINICIO DE ESCOAMENTO DE MATERIAIS VISCOPLÁSTICOS EM TUBOS HORIZONTAIS USANDO VELOCIMETRIA POR IMAGEM DE PARTÍCULAS

Start-Up Flow Visualization Of Viscoplastic Materials In Horizontal Pipes Using Particle Image Velocimetry

MSc dissertation presented to the Postgraduate Programme in Mechanical and Materials Engineering from the Federal University of Technology - Paraná, as fulfilment of the requirements for Master degree in Engineering - Concentration Area: Thermal Engineering.

Advisor: Prof. Dr. Admilson Teixeira Franco

CURITIBA
2021

Ministério da Educação
Universidade Tecnológica Federal do Paraná
Câmpus Curitiba

ANGEL DE JESUS RIVERA JIMENEZ

VISUALIZAÇÃO DO REINICIO DE ESCOAMENTO DE MATERIAIS VISCOPLÁSTICOS EM TUBOS HORIZONTAIS USANDO VELOCIMETRIA POR IMAGEM DE PARTÍCULAS

Trabalho de pesquisa de mestrado apresentado como requisito para obtenção do título de Mestre Em Engenharia da Universidade Tecnológica Federal do Paraná (UTFPR). Área de concentração: Engenharia Térmica.

Data de aprovação: 10 de Fevereiro de 2021

Prof Admilson Teixeira Franco, Doutorado - Universidade Tecnológica Federal do Paraná

Prof Cezar Otaviano Ribeiro Negrao, Doutorado - Universidade Tecnológica Federal do Paraná

Prof Edson Jose Soares, Doutorado - Universidade Federal do Espírito Santo (Ufes)

Prof Guilherme Henrique Fiorot, Doutorado - Universidade Federal do Rio Grande do Sul (Ufrgs)

Documento gerado pelo Sistema Acadêmico da UTFPR a partir dos dados da Ata de Defesa em 08/04/2021.

ACKNOWLEDGEMENTS

I aknowledge my parents, who gave me the most precious teaching, for her support and guidance. They have always been my motivation and has encouragement bestowed upon me.

To my siblings, who always supported me in the stages of this learning process.

To my supervisor, Admilson T. Franco, and my co-supervisor, Eduardo M. Germer, for the opportunity, guidance, dedication, patience, and confidence in my capacity.

The LabFlow trainees and employees, who helped me in the construction of the experimental setup and for the invaluable support in doing this work.

"If you would be a real seeker after truth, it is necessary that at least,
once in your life you doubt, as far as possible, all things."
René Descartes.

RESUMO

RIVERA, Angel De Jesus.**Visualização do Reinicio de Escoamento de Materiais Viscoplásticos em Tubos Horizontais Usando Velocimetria por Imagem de Partículas.** Dissertação de Mestrado. Programa de Pós-Graduação em Engenharia Mecânica e de Materiais, Universidade Tecnológica Federal do Paraná, Curitiba, Brasil, 118 páginas, 2021.

O escoamento de materiais viscoplásticos pode ser encontrado em inúmeros setores industriais, como o processamento de polímeros, bombeamento de comida, indústria de óleos parafínicos, entre outros. Em situações de fechamento devido a emergências ou manutenção, o material restante apresenta uma estrutura gelificada após determinado intervalo de tempo. Objetivando reiniciar o escoamento são aplicadas altas pressões, como no caso de óleos parafínicos em reservas marítimas, situação na qual sobrestimar as pressões pode causar o aumento das dimensões da tubulação e, consequentemente, os custos de produção. Dessa forma faz-se necessária uma predição estimada da pressão mínima para o reinício de circulação como requisito operacional. O objetivo desse estudo experimental é investigar e visualizar o reínicio de escoamento de materiais de tensão limite. Para uma melhor compreensão da dinâmica de escoamento desses materiais são utilizados como montagem experimental uma seção de teste de comprimento 0,980 m com seção circular de raio interno de 0,011 m conectada a dois reservatórios para controle de pressão de entrada e saída e um sistema de visualização por velocimetria por imagens bi dimensionais de partículas (PIV). Duas soluções aquosas de Carbopol® (25 e 50 wt%) são utilizadas como fluidos viscoplásticos. Os perfis de velocidade, a presença de uma estrutura de plug e a transição sólido-fluído são analisadas antes do fluido começar a escoar. A relação entre a mínima queda de pressão de reinício e a evolução do campo de velocidade é observada para diferentes soluções. Ademais, o tempo necessário para reiniciar uma linha bloqueada depende principalmente da queda de pressão aplicada e da viscosidade que aumenta em função do tempo. Finalmente, foi observado que a que a velocidade de escorregamento aumenta exponencial com a tensão cisalhante na parede e com o gradiente de velocidade.

Key words: Fluido viscoplástico. Reinício de escoamento. Tensão límite de fluência. Estudo experimental. PIV.

ABSTRACT

RIVERA, Angel De Jesus.**Start-up Flow Visualization of Viscoplastic Materials in Horizontal Pipes Using Particle Image Velocimetry.** Master of Science Dissertation. Postgraduate Program in Mechanical and Materials Engineering, The Federal University of Technology - Paraná, Curitiba, Brazil, 118 pages, 2021.

The flow of viscoplastic materials is widely found in various industrial sectors, such as polymer processes, food pumping, paraffin oil industry, among others. In shutdown situations due to emergency or maintenance, the material at rest exhibits a gel-like structure after a period of time. In order to restart the flow high pressures are applied which result in a overestimation of the dimensions of the pipeline and the production costs. Therefore, an accurate prediction of the minimum pressure to restart the flow is necessary as an operational requirement. The objective of this experimental study is to investigate and visualize the start-up flow of yield stress materials in pipes. For a better understanding of the flow dynamics of these materials, a test section of length 0.980 m with a circular cross-section of inner radius 0.011 m attached to two reservoirs to control the inlet and outlet pressure and Two-dimensional Particle Image Velocimetry (PIV) visualization system is used as an experimental setup. Two aqueous solutions of Carbopol® (25 and 50 wt%) are used as viscoplastic fluids. The velocity profiles, the presence of plug structure and the solid-fluid transition are analyzed before the fluid begins to yield. A relationship between the minimum start-up flow pressure drop and velocity field evolution is observed for the different solutions. Moreover, the time required to restart the jammed line depends mainly on the applied pressure drop and the viscosity that decreases with time. Finally, it was observed that the slip velocity increases in an exponential way with the wall shear stress and velocity gradients.

Keywords: Viscoplastic fluid. Start-up flow. Wall slip. Yield stress. Experimental study. PIV.

LIST OF FIGURES

LIST OF TABLES

LIST OF ABBREVIATIONS AND ACRONYMS

APHA	Americam Public Healt Association Color Scale
CERNN	Center for Research in Rheology and Non-Newtonian fluids
CMOS	Complementary Metal-Oxyde-Semiconductor
CH-PP	Cross-Hatched Parallel Plate
DPIV	Digital Particle Image Velocimetry
HGS	Hollow Glass Spheres
HB	Herschel-Bulkley
IA	Interrogation Area
LabFlow	Non-Newtonian Fluid Flow Laboratory
LDV	Laser Doopler Velocimetry
Nd:Yag	Neodymium-doped Yttrium aluminum garret
PIV	Particle Image Velocimetry
PMMA	Polymethyl Methacrylate
PVC	Polivinyl Cloride
PP	Polypropylene
RSD	Relative Standard Deviation
S-PP	Smooth Parallel Plate
S/R	Root Mean Square of Negative Values
UDV	Ultrasonic Doppler Veocimetry
WRC	Weissenberg Rabinowitsch Correction
UTFPR	Federal University of Technology-Parana

NOMENCLATURE

Roman letters and symbols

c	Velocity of light in vacuum	$[m\ s^{-1}]$
C_n	Fourier - Bessel series coefficient	$[-]$
C_c	Combined correction	$[-]$
D	Diameter	$[m]$
d_τ	Seeding particle diameter in pixel	$[pixel]$
d_τ	Seeding particle diameter	$[\mu m]$
d	Gap between geometries for rheometric tests	$[mm]$
f	Fanning friction factor	$[-]$
e_s	Sampling error for PIV technique	$[-]$
G	Uncertainty Magnitude	$[-]$
k	Consistency index	$[Pa\ s^n]$
k'	Noise intensity parameter	$[-]$
k_b	Consistency index of binder fluid	$[Pa\ s^n]$
L	Characteristic lenght	$[m]$
M_t	Measurement time	$[s]$
n	Power-law index	$[-]$
n_b	Power-law index of binder fluid	$[-]$
n_{ref}	Refraction index	$[-]$
N_T	Number of total images	$[-]$
P_{in}	Entrance pressure	$[Pa]$
P_{out}	Out pressure	$[Pa]$
Q	Volumetric flow rate	$[m^3\ s^{-1}]$
Q_{ns}	Volumetric flow rate no-slip condition	$[m^3\ s^{-1}]$
Q_s	Volumetric flow rate with slip condition	$[m^3\ s^{-1}]$
R	Pipe radius	$[m]$
r_0	Yielding position	$[m]$
r_i	Radial position	$[m]$
r	Radius ratio	$[m]$
r_p	Plug radius	$[m]$
t	time	$[s]$
t_{shear}	Shear time	$[s]$
t_{rest}	Resting time	$[s]$
t_c	Critical time	$[s]$

t'	Dimensionless time	$[-]$
u_z	Velocity profile at z-direction	$[ms^{-1}]$
u_{zp}	Plug velocity	$[m\ s^{-1}]$
$\bar{U}$	Mean velocity at the test section	$[m\ s^{-1}]$
u_i	Local axial velocity at the radial position	$[m\ s^{-1}]$
u'_s	Dimensionless slip velocity	$[ms^{-1}]$
v	Velocity of light in the fluid	$[m\ s^{-1}]$
$\bar{x}$	Arithmetic mean	$[-]$
X_D	Length of the view size in the axial direction	$[m]$
x_{theo}	Theoretical data	$[-]$
x_{exper}	Experimental data	$[-]$

Functions

$\mathbf{J_0}$	Bessel function of the first kind
$\mathbf{J_1}$	Bessel function of the second kind

Greek letters

β	Slip coefficient	$[-]$
$\dot{\gamma}$	Shear rate	$[s^{-1}]$
$\dot{\gamma}_{xy}$	Shear rate xy-coodinates	$[s^{-1}]$
$\dot{\gamma}_{aw}$	wall apparent shear rate	$[s^{-1}]$
$\dot{\gamma}_{corr}$	Corrected shear rate	$[s^{-1}]$
$\dot{\gamma}_c$	Critical shear rate	$[s^{-1}]$
$\delta\alpha$	Small angles	$[rad]$
δt	Time interval	$[s]$
δl	Differential distance in x-direction	$[m]$
δu	Differential constant velocity	$[m\ s^{-1}]$
δy	Differential distance in y-direction	$[m]$
δA_y	Differential area	$[m^2]$
δF_x	Differential force in x-direction	$[N]$
δ	Slip layer thickness	$[\mu\ m]$
Δp	Pressure drop	$[Pa]$
Δt	Time between pulses	$[s]$
η	Apparent viscosity	$[Pa\ s^n]$
η^C	Apparent viscosity for Casson model	$[Pa\ s^n]$
η^B	Apparent viscosity for Herschel-Bulkley model	$[Pa\ s^n]$
λ	Wavelength	$[nm]$
μ	Absolute (or dynamic) viscosity	$[Pa\ s]$
ν	Kinematic viscosity	$[m^2\ s^{-1}]$

ρ	Density	$[kg\ m^{-3}]$
σ_x	Standard deviation	$[-]$
$\bar{\sigma}$	Standard error	$[-]$
τ_{xy}	Shear stress at xy-coordinates	$[Pa]$
τ_{rz}	Shear stress at rz-coordinates	$[Pa]$
τ_0	Yield stress	$[Pa]$
τ_0^B	Yield stress for Bingham model	$[Pa]$
τ_0^H	Yield stress for Herschel-Bulkley model	$[Pa]$
τ_0^C	Yield stress for Casson model	$[Pa]$
ϕ	Shear stress ratio	$[-]$

Non-dimensional parameters

Re	Reynolds number	$[-]$

Subscripts

$(\ )_r$	Evaluated at the radius
$(\ )_w$	Evaluated at the wall

Operators

$d(\ )/d(\ )$	Gradient
$\delta\,(\ )$	Uncertainty value for a variable
$\partial(\ )/\partial(\ )$	coefficient of sensitivity for a variable

CONTENTS

1 INTRODUCTION

1.1 Context

The flow of non-Newtonian materials in pipes is commonly encountered in several practical and engineering applications such as moldings, injection, extrusion, polymer processes, personal care products, food industry, pumping of waxy crude oil, among others. In the last application, when operations are carried out in marine environments (*Offshore*) the non-Newtonian behavior is present in different processes, such as in the exploration and production stages. Regarding waxy crude oil, the non-Newtonian behavior of waxy crude oil represents significant challenges during transport from reservoirs to the surface. Waxy crude oil exposed to a cold environment loses heat and may experience large temperature drops that cause paraffinic precipitation and subsequently obstruction of the pipeline if it remains at rest for long periods of time. Consequently, high pressures must be applied to start-up flow, which causes damage to the transport pipeline network. This last problem is the reason for the oversizing of the pipelines (RØNNINGSEN, 1992; SIERRA et al., 2016), and associated with other problems, they are reflected in high operating costs that sometimes make projects unviable (GAO et al., 2020). Figure 1.1 shows a diagram of paraffinic oil transport from the reservoir and the main changes before reaching the surface.

Figure 1.1 – *Offshore* production system with producing wells, subsea pipelines, oil production ship, export pipeline, and *Onshore* oil terminals. Points 1, 2 and 3 indicate the behavior of material as it is transported to the surface.

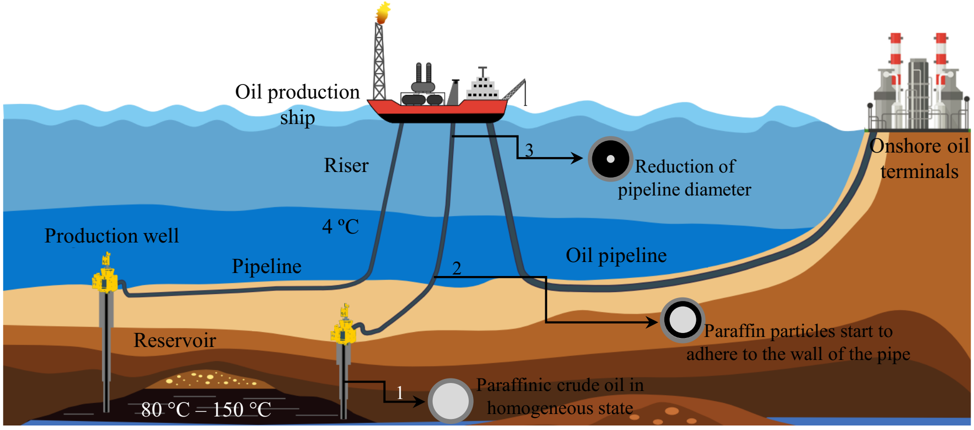

Source: Adapted from DALLA (2018)

In the context of the obstruction in the transport pipeline due to the paraffinic precipitated, the fluid has a gel-like structure. In consequence, a complex non-Newtonian behavior arises that includes thixotropy and elasto-viscoplasticity (MARCHESINI et al., 2012; BALMFORTH et al., 2014; BONN et al., 2017). This complex behavior is one of the reasons why it is difficult to calculate the pressure drops that accurately must be applied to start-up flow after shutdowns in production (CHANG et al., 1998; MENDES et al., 2015).

In order to understand the complexity of the gel-like structure formed, several researchers have studied their rheological properties separately, as in Mendes (2009), Mendes (2011), and Mendes and Thompson

(2013), where the thixotropic behavior was studied using aqueous solutions of Laponite®. Whereas the viscoplastic behavior was studied by Visintin et al. (2005), Sierra et al. (2016), Liu and Bruyn (2018), and Abedi et al. (2019) using aqueous solutions of Carbopol®. This last material has been considered for many years as a model yield stress fluid due to good micro-structural stability, negligible thixotropy, and optical transparency (OVARLEZ et al., 2013).

1.2 Problem assessment

As discussed in the previous section, after long periods of the paraffinic crude oil being at rest, a gel-like structure is formed. To break this structure, it is necessary to impose pressure, but the value of this pressure is not precisely known due to the rheological complexity of paraffinic crude oil. Considering this problem and the possibility of study it separately, this research focuses on analyzing the viscoplastic behavior of paraffinic oil in smooth pipes and provides relevant information to be extrapolated to the operations fields. In other words, the start-up process and the phenomena involved before and during the flow of a viscoplastic material in a smooth wall pipe are analyzed. It should be mentioned that viscoplastic materials are characterized by shows yield stress, that is, critical stress value below which no flow occurs, but above which the viscosity decreases drastically (BARNES, 1999; ABEDI et al., 2019), for this reason, they are also well-known as yield stress fluids, and throughout this investigation, the two terms will be used to refer to the same material. Figure1.2 shows the behavior of a yield stress fluid in a smooth wall pipe when an external force is applied.

Figure 1.2 – Diagram of the transient flow of a yield stress fluid under the application of a driving force. Where R_p is the radius of the plug, R is the radius of the pipe, u_z is the total velocity in axial direction, u_{zp} is the velocity of the plug, and u_s is the wall slip velocity.

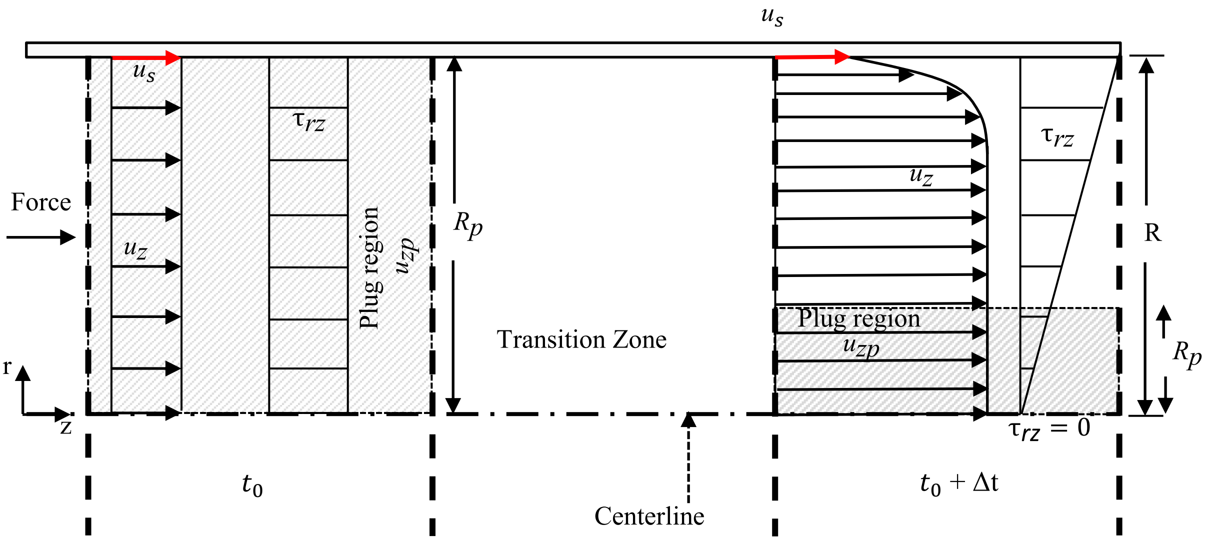

Source: Adapted from Chhabra and Richardson (2011)

From Fig. 1.2 (t_0) it can be seen that for $\tau_{rz} > \tau_0$ the fluid initially does not present any variation in its central structure (R_p), and the fluid flows as a rigid body (plug flow) due to just to the wall slip. Beyond the yield stress value, a zone of coexistence of solid and fluid states is identified, that is, a zone in which destructuring processes are taking place. Finally, the velocity profile presents the shape of a plug given in the central region and with a shear-thinning near the wall ($t_0 + \Delta t$). For the described process, it is observed that the wall slip phenomenon was always coupled to the flow velocity.

Although viscoplastic fluid flows are widely used to represent the viscoplastic behavior of paraffinic oil, as well as to represent the flow of other industrial applications, there are few studies focused on the dynamics of this type of flow that provide a better understanding of their transient behavior in the solid, transition, and fluid zones. The scale of wall slip with other hydrodynamic quantities such as shear stress and velocity gradients in the region near the wall is also less understood, which is paramount important in order to explain the flow of viscoplastic materials in the presence of sliding and get at least a simple phenomenological picture of wall slip. For example, studies carried out by Liu and Bruyn (2018) and Abedi et al. (2019) analyzed the laminar flow of viscoplastic fluids but did not report a scale relationship between the hydrodynamic quantities, on the other hand, the scale reported by Pérez-González et al. (2012) between the slip velocity and shear stress does not coincide with the analytical scales reported in Piau (2007).

Based on this lack of quantitative knowledge that can be used to better understand the behavior of yield stress fluids, such as paraffinic crude oil, this research uses Particle Image Velocimetry (PIV) as a non-intrusive technique to visualization and measurement of flow. Through this technique, an idea of the evolution of the material's flow and deformation fields over time and correlations between the main hydrodynamic quantities will be obtained, which will help to understand the flow of viscoplastic materials in the presence of wall slip.

1.3 Objectives

1.3.1 General objective

An experimental investigation of the start-up flow of viscoplastic fluids in the presence of wall slip. Two aqueous solutions of Carbopol (ultrasound gel) will be used, namely, 25wt% and 50wt%. Carbopol® is chosen as viscoplastic fluid because it is considered a model yield stress fluid. (CURRAN et al., 2002; OVARLEZ et al., 2013). Rheometric tests and visualization tests of start-up flow by pressure rises using an experimental setup, and the optical method of flow visualization Particle Image Velocimetry (PIV) will be performed to study materials' behavior in transient flow regime. At the end of chapter 3 (section 3.5), after the definition of fundamental concepts in the theoretical framework and literature review of works related to the study problem, the specific objectives are defined and detailed.

1.4 Document outline

The content of this work is organized in 6 chapters. This chapter presents the introduction, the problem under study, and the general objective.

For the development and understanding of work, Chapter 2 presents the theoretical framework of main concepts on the flow of Newtonian and non-Newtonian fluids and exposes a brief overview of PIV technique. Chapter 3 presents the literature review of works focused on the start-up flow of viscoplastic materials. The literature review is divided into rheometric studies of viscoplastic fluids, start-up flow studies involving experimental setups, and flow visualization techniques, focusing on the Particle Image Velocimetry (PIV) technique. In this chapter after definition, reviews, and consolidation of concepts related to research, the specific objectives of the dissertation are presented.

In chapter 4, the working fluids and formulation are described. The experimental setup, types of equipment, and instrumentation used is detailed. Subsequently, the methodology of start-up flow tests are explained. Besides, the main aspects of the PIV technique are defined, such as the type of particles and image correlation parameters. The error analysis method involved in this experimental study is also explicated. In chapter 5, the results obtained are discussed. The dissertation ends with chapter 6 where the final considerations and suggestions for further work are summarized. In sequence, papers related to the topic of this dissertation published in scientific journals and presented at conferences are exhibited as bibliographic references.

Appendix A presents the measured and calculated experimental uncertainties.

2 THEORETICAL FRAMEWORK

In this chapter, the fundamental concepts for Newtonian and non-Newtonian fluids are presented. The laminar Poiseuille flow in the presence of slip for yield stress fluids in pipes in response to an external stimulus is described. Additionally, a description of the primary mechanisms that affect the sliding on the wall are presented and some principles of the Particle Image Velocimetry (PIV) technique are exposed.

2.1 Rheological behavior

2.1.1 Viscosity

To understand what is a Newtonian and non-Newtonian fluid is necessary to know first, which means viscosity. According to Bird et al. (1983) and Fox et al. (2020), a question then arises, where do stresses come from? For a solid, stresses develop when the material is elastically deformed or strained; for a fluid, shear stresses arise due to viscous flow. Hence, we say solids are elastic, and fluids are viscous (and it is interesting to note that many biological tissues are viscoelastic, meaning they combine features of a solid and a fluid). For a fluid at rest, there will be no shear stresses. We will see that each fluid can be categorized by examining the relationship between the applied shear stresses and the flow (specifically the rate of deformation) of the fluid.

Figure 2.1 – a) fluid element at time *t* and b) deformation od fluid element at time *t*+*δt*.

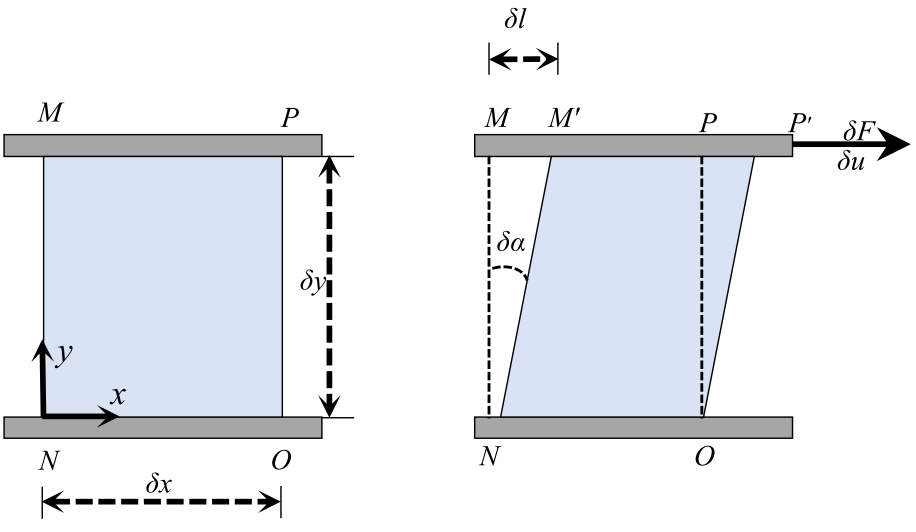

a) b)

Source: Adapted from Macosko and Larson (1994) and Pritchard and Mitchell (2016).

Consider the behavior of a fluid element between the two infinite plates shown in Fig. 2.1a. The rectangular fluid element is initially at rest at time *t*. Let us now suppose a constant rightward force δF_x is applied to the upper plate so that it is dragged across the fluid at constant velocity δu. The relative shearing action of the infinite plates produces shear stress, τ_{yz}, which acts on the fluid element and is given by

$$\tau_{yx} = \lim_{\delta A_y \to 0} \frac{\delta F_x}{\delta A_y} = \frac{dF_x}{dA_y} \tag{2.1}$$

where δA y is the area of contact of the fluid element with the plate and δF$_x$ is the force exerted by the plate on that element. Snapshots of the fluid element, shown in Fig. 2.1a-b, illustrate the deformation of the fluid element from position MNOP at time t, to M′NOP′ at time *t*+δt due to the imposed shear stress. It is the fact that a fluid continually deforms in response to applied shear stress that sets it apart from solids.

Focusing on the time interval δt (Fig. 2.1b), the deformation of the fluid is given by

$$\dot{\gamma} = \lim_{\delta t \to 0} \frac{\delta \alpha}{\delta t} = \frac{d\alpha}{dt} \tag{2.2}$$

We want to express $\delta\alpha$/δt in terms of readily measurable quantities. This can be done easily. The distance, δl, between the points M and M′ is given by δl=$\delta u \delta t$. Alternatively, for small angles, δl=$\delta y \delta \alpha$ and the equating these two expressions for δl gives

$$\frac{\delta \alpha}{\delta t} = \frac{\delta u}{\delta y} \tag{2.3}$$

Taking the limits of both sides of the equality, we obtain

$$\frac{d\alpha}{dt} = \frac{du}{dy} \tag{2.4}$$

Thus, the fluid element of Fig. 2.1, when subjected to shear stress τ_{yz}, experiences a rate of deformation (shear rate) given by *du/dy*. We have established that any fluid that experiences a shear stress will flow (it will have a shear rate). What is the relation between shear stress and shear rate? Fluids in which shear stress is directly proportional to the rate of deformation are *Newtonian fluids*. The term *non-Newtonian* is used to classify all fluids in which shear stress is not directly proportional to shear rate.

2.1.2 Newtonian fluids

According to (CHHABRA; RICHARDSON, 2011), simple organic liquids, and molten metals exhibit a Newtonian behavior under normal conditions, and that for gases, viscosity increases with temperature, whereas for liquids, viscosity decreases with increasing temperature. If the fluid of Fig. 2.9 is Newtonian, then

$$\tau_{yx} \propto \frac{du}{dy} \tag{2.5}$$

The constant of proportionality in Eq.(2.5) is the *absolute (or dynamic) viscosity*, μ. Thus in terms of the coordinates of Fig. 2.1, Newton's law of viscosity give for one-dimensional flow by

$$\tau_{yx} = \mu \frac{du}{dy} \tag{2.6}$$

Note that, since the dimensions of τ_{yx} are [*F/L*^{2}] and the dimensions of *du/dy* are [*1/t*], μ has dimensions [*Ft/L*^{2}*]*. Since the dimensions of force, F, mass, M, length, L, and time, t, are related by Newton's second law of motion, the dimensions of μ can also be expressed as [*M/Lt*].

2.1.2.1 Reynolds number for Newtonian fluids

The Reynolds number is one of the most important dimensionless quantities in fluids. It correlates the inertia forces to the viscous forces. The Reynolds number was first described by Reynolds in 1883, although others have used the quantity before, e.g., Stokes. It is defined as:

$$R_e = \frac{\rho \bar{U} D}{\mu} \tag{2.7}$$

when ρ is liquid density, $\bar{U}$ is the average velocity, D is the pipe internal diameter and μ is the absolute viscosity. This important dimensionless parameter is used in classifying the type of flow in pipelines. Depending on the Reynolds number, the through pipes will fall into one of these three flow regimes. Typically, an R_e value of 2100 is used as the laminar flow limit, which is the case in this experimental study.

2.1.3 Non-Newtonian fluids

Fluids that do not follow the linear law of Eq.(2.6) are called Non-Newtonian fluid (BIRD et al., 1983). Two familiar examples are toothpaste and Lucite® paint. The latter is very "thick" when in the can, but becomes "thin" when sheared by brushing. Toothpaste behaves as a "fluid" when squeezed from the tube. However, it does not run out by itself when the cap is removed. There is a threshold or yield stress below which toothpaste behaves as a solid (FOX et al., 2020). Strictly speaking, the definition of a fluid is valid only for materials that have zero yield stress. Non-Newtonian fluids are commonly classified as time-independent or time-dependent (DESHPANDE, 2010). Examples of time-independent behavior are shown in the rheological diagram of Figure 2.2

Numerous empirical equations have been proposed (MACOSKO; LARSON, 1994; TANNER, 2000) to model the observed relations between τ_{yx} and *du/dy* for time-independent fluids. They may be adequately represented for many engineering applications by the power-law model, which for one-dimensional flow becomes

$$\tau_{yx} = k \left(\frac{du}{dy} \right)^n \tag{2.8}$$

Figure 2.2 – Rheological flow curves for Newtonian and non-Newtonian fluids.

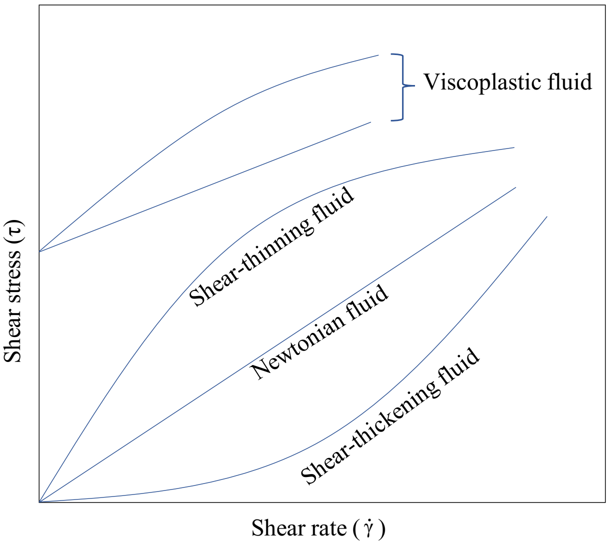

Source: Retrieved from Bird et al. (1983).

where the exponent, *n*, is called the flow power-law index and the coefficient, *k*, the consistency index. This equation reduces to Newton's law of viscosity for *n*=1 and *k*=μ. To ensure that τ_{yx} has the same sign as *du/dy*, Eq.(2.8) is rewritten in the form

$$\tau_{yx} = k\left|\frac{du}{dy}\right|^{n-1}\frac{du}{dy} = \eta\frac{du}{dy} \tag{2.9}$$

The term η=*k*$|du/dy|^{n\text{-}1}$ is referred to as the *apparent viscosity*. The idea behind Eq. 2.17 is that we end up with a viscosity η that is used in a formula that is the same form as Eq.(2.6), in which the Newtonian viscosity μ is used. The big difference is that while μ is constant (except for temperature effects), η depends on the shear rate. Most non-Newtonian fluids have apparent viscosities that are relatively high compared with the viscosity of water.

Fluids in which the apparent viscosity decreases with increasing shear rate ($n < 1$) are called *shear-thinning* (or *pseudoplastic*). Colloids, polymers are examples of shear-thining fluids. Mathematical models such as power-law and Carreau describe the behavior of this type of non-Newtonian fluids (CHHABRA; RICHARDSON, 2011). If the apparent viscosity increases with increasing deformation rate ($n > 1$) the fluid is termed *shear-thickening or dilatant*. Suspensions of starch and sand are examples of dilatant fluids (CHHABRA; RICHARDSON, 2011; FOX et al., 2020). These fluids can be represented by power law mathematical models (FRITZ et al., 2002). Furthermore, according to Bingham (1922) a fluid that behaves as a solid-like until minimum yield stress, τ_0, is exceeded is a viscoplastic fluid. Such material behaves solid-like, i. e., deform elastically for shear stress values below the yield stress, and like a viscous fluid for stress values above the yield stress (MEWIS; SPAULL, 1976; BIRD et al., 1983; COUSSOT et al., 2017). Materials such as mayonnaise, ultrasound gels, shaving foams, among others, exhibit a viscoplastic behavior. The Bingham and Herschel-Bulkley models represent the behavior of these fluids. Figure 2.2 shows the behavior of the types of non-Newtonian fluids described. Viscoplastic fluids behavior is detailed in the next subsection of this chapter, also the mathematical models represent this type of material.

2.2 Viscoplastic fluid behavior

As previously explained, this type of fluid is characterized by the existence of a yield stress τ_0, which must be exceeded before the fluid flows (CHHABRA; RICHARDSON, 2011). This kind of behavior can be explained if the substance at rest is considered as a group of rigid three-dimensional structures that resist any external stress less than τ_0. For stress greater than τ_0, the structure breaks down, and the substance behaves like a viscous material. In some cases, the build-up and breakdown of the structure have been found to be reversible, i.e., the substance may regain its initial value of the yield stress (CHHABRA; RICHARDSON, 2011).

The viscoplastic materials display an apparent viscosity, which decreases with shear rate. At very low shear rates, the apparent viscosity is considered as infinite at the instant before the substance yields and begins to flow. It is thus possible to regard these materials as a particular class of shear-thinning fluids. It is virtually impossible to ascertain whether any real material has a true yield stress or not, but the concept of the yield stress is convenient in practice due to some materials approximate very close to this type of behavior (CHHABRA; RICHARDSON, 2011). The advent of constant-stress rheometers has made it possible to scrutinize the behavior of materials at very low shear rates. Common examples of viscoplastic fluid behavior include particulate suspensions, emulsions, foodstuffs, blood, gels, drilling fluids, and muds (BARNES, 1999).

2.2.1 Mathematical models

Many empirical expressions have been proposed as a result of curve-fitting examinations. There are three commonly used models to describe yield stress fluids, and they are presented in the following subsections.

2.2.1.1 The Bingham plastic model

The most model common to describe the behavior of a fluid with yield stress is the Bingham plastic model, which has two parameters that are the yield stress and plastic viscosity of the fluid. As it is shown in Fig. 2.3, the fluid initially resists flowing until the shear stress exceeds a specific value. After the fluid flow start-up, there is a linear relationship between shear stress and shear rate (MACOSKO; LARSON, 1994). The model is expressed as:

$$
\begin{aligned}
\tau_{yx} &= \tau_0 + \mu \left(\dot{\gamma}_{yx}\right) && \text{for} \quad |\tau_{yx}| > \tau_0 \\
\dot{\gamma}_{yx} &= 0 && \text{for} \quad |\tau_{yx}| < \tau_0
\end{aligned}
\tag{2.10}
$$

Where τ_0 is the yield stress, μ is plastic viscosity, and $\dot{\gamma}_{yx}$ is the component of the shear rate in x direction perpendicular to y direction. Importantly, note that Bingham fluids do not ordinarily exhibit true y-intercept threshold stress (or yield stress) but are elastic before the linear plastic portion occurs.

Nonetheless, in the oil industry, the Bingham model is very helpful in field quality control checks of the mud system.

2.2.1.2 The Herschel-Bulkley fluid model

The Herschel-Bulkley model is one of the complex models whith three parameters and defines the behavior of non-Newtonian fluids such as the drilling fluids, with a good representation of the behavior compared to the other models (MACOSKO; LARSON, 1994). The model is expressed as:

$$\begin{aligned} \tau_{yx} &= \tau_0 + k\left(\dot{\gamma}_{yx}\right)^n && \text{for} \quad |\tau_{yx}| > \tau_0 \\ \dot{\gamma}_{yx} &= 0 && \text{for} \quad |\tau_{yx}| < \tau_0 \end{aligned} \tag{2.11}$$

In this model, k and n are two empirical curve-fitting parameters and are known as the fluid consistency coefficient and the flow behavior index, respectively.

The Herschel-Bulkley model is a general model that can be reduced to the Bingham and power-law model. If the τ_0 is zero, then the Herschel-Bulkley reduces to the power-law model. If n is equal to 1, then the Herschel-Bulkley reduces to the Bingham plastic model.

Figure 2.3 – Typical sketch of the fit curves of rheological models.

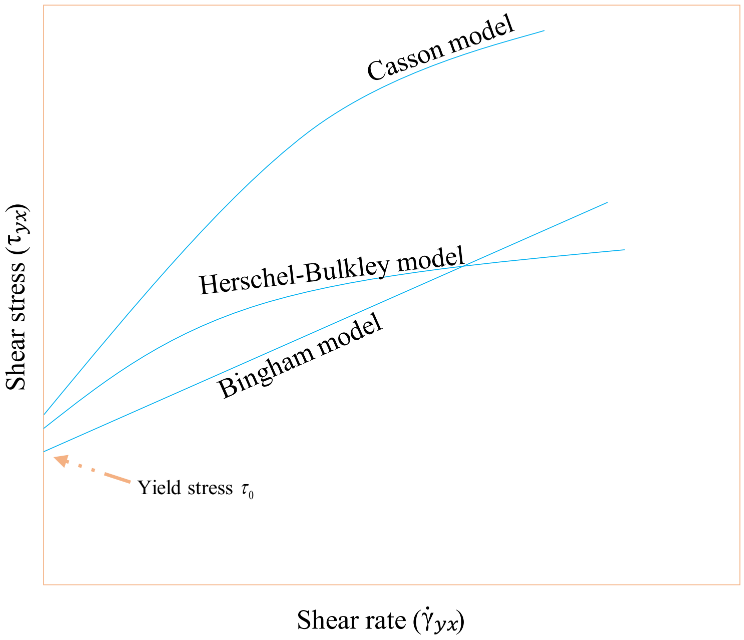

Source: Retrieved from Chhabra and Richardson (2011).

2.2.1.3 The Casson fluid model

This model has often been used for describing the steady shear stress and shear rate behavior of some fluids as blood, molten chocolates, and also some particles suspensions that have a behavior closely described by this model, where η_C is the plastic viscosity determined for this model (CHHABRA; RICHARDSON, 2011; MALKIN, 1994),

$$\begin{aligned} (|\tau_{yx}|)^{1/2} &= \left(\tau_0^C\right)^{1/2} + (\eta_C|\dot{\gamma}_{yx}|)^{1/2} && \text{for} \quad |\tau_{yx}| > \tau_0^C \\ \dot{\gamma}_{yx} &= 0 && \text{for} \quad |\tau_{yx}| < \tau_0^C \end{aligned} \tag{2.12}$$

The three models for viscoplastic fluid behavior are sketched in Fig.2.3. At each model τ_{yx} is represented and tried carefully to write the stress expressions as a function of the shear rate. Other emperical models contain yield stress, such as the modified Casson equation, the generalized Casson equation, the Crowley-Kitzes model, the Shul'man equation, among others (BIRD et al., 1983).

2.2.2 Wall slip

Following Sochi (2011) in the flow of viscous fluids over solid surfaces, the 'no-slip' at the solid-fluid interface is a widely-accepted boundary condition with many significant consequences. The essence of this condition is the continuity of the tangential component of the velocity at the wall due to the fact that viscous fluids stick to the solid surface (TANNER, 2000). Strictly speaking, no-slip means that the instantaneous relative velocity between the fluid and surface, as well as its time average, is zero (LAM et al., 2007). The absence of slip at the surface creates a boundary layer in the flow field, where the viscous effects and velocity gradients are substantial. This is particularly important in non-Newtonian fluid systems where shear rate effects, such as shear-thinning, can be amplified. The thickness of the boundary layer is directly related to the fluid viscosity (MACIEL et al., 2002).

Slip may be divided into positive, which increases the flow throughput of the flow system, and negative, which decreases the flow throughput. The latter occurs, for example, when the slip layer is more viscous than the bulk, which results in hindering the flow, or when there is a stagnant layer or a back-flow at wall (RUIZ-VIERA et al., 2006). Positive wall slip contributes to the total flow throughput, and hence the total flow in slippery systems has contributions from slip and bulk deformation (JR; JR, 1970). This may be quantified by the slip fractional flow rate, which is the ratio of the volumetric flow rate of slip contribution to the total flow rate (COHEN; METZNER, 1986). In some systems, such as microfluidic and viscoplastic, and over certain deformation rate regimes, the contribution of wall slip to the total flow rate could be substantial (KALYON, 2005). In some extreme cases of plug flow, the flow is due to wall slip, and hence the fractional flow rate becomes unity. Below is a brief review of the mechanisms that affect slip, how it is estimated, and the relationship with non-Newtonian behavior

2.2.2.1 Slip Mechanisms

Slip is a diverse phenomenon with different physical causes depending on the flow system and surrounding conditions. The solid-fluid interaction affect several static and dynamic factors that influence the adherence and slip. There is no general theory to describe wall slip in all situations; however, there many mechanisms proposed to explain slip in certain circumstances and for certain flow systems (LUK et al., 1987). One of these mechanisms is the depletion of the boundary layer where the particles in a sheared dispersed system, such as emulsions and suspensions, migrate away from the boundary region resulting in a very thin low viscosity layer adjacent to the wall, which acts as a lubricating film that facilitates fluid movement (CHURAEV et al., 1984; BERKER; ARSDALE, 1992). Some statements in the literature may suggest that this is the only viable mechanism for wall slip. However, it is more appropriate to regard this as the main slip mechanism for the apparent slip in a certain category of fluids, such as suspensions and emulsions, especially those whose viscosity is highly-dependent on concentration. In other systems, apparent slip can arise from other mechanisms; furthermore, true slip can also occur with no need for a depleted or even a slip layer (SOCHI, 2011).

Another proposed mechanism for wall slip, which is also viable for multicomponent fluids such as colloids, is devoloping a layer of adsorbed particles on the solid surface due to strong attractive forces between these dispersed particles and the surface. This layer acts as a 'soft cushion' over which the particles in the fluid slide (SETH et al., 2008). Sedimentation due to gravitational or other forces could also be at the origin of this mechanism. A third mechanism for slip at the wall is the formation of a thin lubricating film at the wall due to the presence of additives which migrate to the boundary region to form the film or to reduce the viscosity of the mixture in that region (KISSI; PIAU, 1996). Several other mechanisms have also been proposed to explain wall slip. These include adhesive failure at the interface, cohesive failure in the vicinity of the interface, chain disentanglement, de-bonding and desorption events (ROBERT et al., 2004). Some of these mechanisms are essentially the same or can originate from other mechanisms. Adhesive failure at the interface, cohesion failure in the vicinity of the interface, unraveling of the chain, disbanding and desorption events (WALLS et al., 2003). Some of these mechanisms are essentially the same or may have their origin in other mechanisms, but they are also considered potential facilitators of wall slip. However, the validity of any proposed mechanism is solely dependent on observational confirmation in real-life experiments (BARNES, 1995).

2.2.2.2 Slip quantification

The wall slip is quantified by the relative solid-fluid velocity at the interface. An approximate estimate of the slip velocity (u_s) may be obtained from non-linear adjustments of the velocity fields measured through the use of visualization techniques, such as the PIV technique, LDV (Laser Doppler Velocimetry), among others. It is also possible by modifying equations such as Eyring's equation for the shear rate across a layer of molecules. As pointed out earlier, slip velocity is a function of the wall shear stress (HATZIKIRIAKOS, 1994; KOZICKI et al., 1966). The thickness of the slip layer is also a function of the wall shear stress (BALMFORTH et al., 2014). The correlation between the slip velocity and wall shear stress, which in many cases is assumed to be linear although it may be non-monotonic with deformation rate variation, is linked through the slip coefficient. But nonlinear correlations have also been reported, such as quadric (SETH et al., 2008), cubic (BARNES, 1995), and power-law dependencies (MACIEL et al., 2002), have also been proposed in the literature. In the case of power-law dependence, which is the most common form, the exponent of the power-law, as well as its coefficient, usually vary depending on the solid-fluid system and ambient conditions (COHEN; METZNER, 1986; KALYON, 2005; CHEN et al., 2009).

Since slip velocity depends on several factors, such as fluid and surface properties as well as the surrounding conditions like pressure and temperature, the slip coefficient β is system-dependent (LAWAL; KALYON, 1998). This dependency allows the above-mentioned simplification of the relation between slip velocity and wall shear stress as a direct proportionality. According to (KALYON, 2005), this direct relationship allows obtaining a simple phenomenological picture of the wall slip behavior and to obtain an estimate of the thickness of the slip layer as:

$$u_s = \beta(\tau_w)^{\frac{1}{n_b}} \tag{2.13}$$

where β is expressed as:

$$\beta = \frac{\delta}{k_b^{\frac{1}{n_b}}} \tag{2.14}$$

and β relates the thickness of the slip layer (δ) to the consistency index k_b and the power-law index n_b of binder fluid. The thickness of the slip layer varies depending on the solid-fluid system characteristics (such as viscosity, elastic modulus, bulk density, particle size, concentration, surface composition, surface roughness, and flow geometry) as the deformation rate and surrounding conditions. Most values reported in the literature give an estimate of the slip layer thickness in the order of a micron with some exceptionally low values in the nanometer range (KALYON et al., 1993; RUIZ-VIERA et al., 2006)

2.2.2.3 Slip and non-Newtonian behavior

Wall slip occurs in Newtonian as well as non-Newtonian fluid systems (CHURAEV et al., 1984), although its occurrence in non-Newtonian is more common than in Newtonian. The reason is that the complexity of non-Newtonian fluids, especially multi-component fluids, allows the introduction of many factors that promote this phenomenon. Slip seems to be the exception in Newtonian systems and the norm in, at least, some types of non-Newtonian systems such as dispersions and yield-stress fluids (SCHOWALTER, 1988). The slip effects are particularly important in non-Newtonian systems as the steep velocity gradients at the boundary layer mean high shear rates with subsequent amplification of shear rate-induced effects such as shear-thinning, shear-thickening, and time-dependency (MACIEL et al., 2002).

Experimental observations indicate that the slip contribution to the flow rate increases with increasing wall shear stress in the shear-thickening fluids, while it decreases in the shear-thinning fluids (COHEN; METZNER, 1986). Although the general trend in wall slip is that it normally results in an apparent drop in the bulk viscosity (NGUYEN; BOGER, 1992) and hence in an increase in the flow throughput, in the case of shear-thinning fluids the slip could, in principle, result in an increase in the apparent viscosity and a drop in the flow throughput if the extra flow due to slip does not compensate for the loss of flow due to the lack of deformation and consequent shear-thinning. Finally, a similar argument may also apply to yield-stress fluids in the case of partial yield with a mixed plug and bulk flow due to slip-related inhomogeneous stress distribution (SOCHI, 2011).

2.2.2.3.1 Relationship between yield stress and slip

Wall slip is commonplace in yield-stress fluid systems. One consequence of this is that there is normally an apparent yield due to slip at lower stress than the bulk yield-stress. This could obscure the viscoplastic nature of the material because the apparent flow due to slip hides the yield-stress behavior (LINDNER et al., 2000). In these cases, direct observation techniques, such as visualization, may be required to clarify the situation. Slip could also result in a misleading lower value of yield-stress because although the material appears to flow at a lower value of stress, it does so by sliding rather than by undergoing bulk deformation (MAGNIN; PIAU, 1990; WALLS et al., 2003). Because the local stress is below the yield value except possibly at the boundary region, no yielding occurs except at a very thin layer adjacent to the surface, which serves as a lubricating slip film. There is also the possibility that the sliding occurs through a depleted inhomogeneous layer from the continuum phase, or through a film from another phase which exists on the surface before the contact or is deposited on the surface from the bulk phase (NGUYEN; BOGER, 1992). The lower yield-stress value due to slip may be called ‘sliding’ or ‘apparent’ yield-stress (MEEKER et al., 2004). Slip can also lead to large errors in viscosity estimations and flow rate predictions in these systems (MAGNIN; PIAU, 1990). It should be remarked that slip could also happen at high deformation rate regimes following bulk-yielding in association with the bulk flow (LINDNER et al., 2000). However, depending on the value of the applied stress three regimes of slip have been detected: at low stress (at and below yield stress) the flow is entirely due to wall slip, slightly above the yield-stress both bulk flow and slip have significant contribution to the fluid motion, and well above the yield stress the slip is negligible and the flow is almost entirely due to bulk deformation. Similar observations have been reported in other studies. Although this behavior trend is quite logical and may be valid for other types of yield-stress systems, experimental verification is required to generalize these results to other systems (SOCHI, 2011).

Figure 2.4 – a) Sketch velocity profile of a viscoplastic fluid and the shear stress profile in a pipe. b) Derivative of a viscoplastic fluid velocity profile for the radial position. Vertical dashed lines indicate the yielding position (r_0) in the velocity and shear rate profiles, respectively.

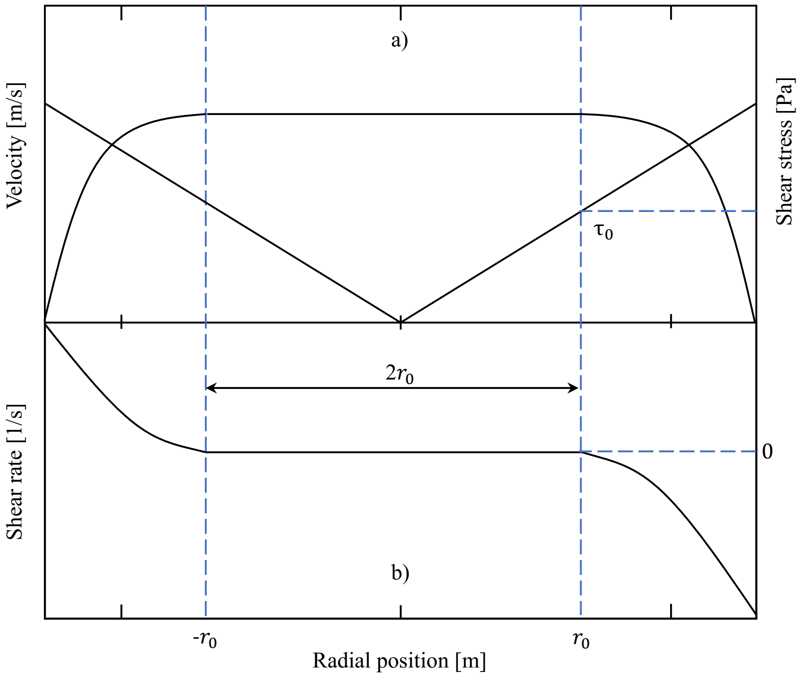

Source: Retrieved from López-Durán et al. (2013).

It is noteworthy that wall slip may be exploited beneficially to measure the yield stress of viscoplastic materials. Real yield in viscoplastic materials usually marks the transition from plug flow to bulk flow where deformation-induced flow dominates and the significance of slip contribution to the total flow rate reduces dramatically (NGUYEN; BOGER, 1992). This transition can be used to estimate the yield-stress value of viscoplastic materials (DIVOUX et al., 2010). Furthermore, according to Pérez-González et al. (2012), the yield stress can also be calculated directly from the velocity profiles via their first derivative.

According to the shape of a velocity profile, its first derivative, which also represents the true shear rate for a unidirectional flow, must become zero at the position where the shear stress reaches the yield value. Fig. 2.4b shows the first derivative of the velocity as a function of the radial position (dv/dr) for the profile sketched in Fig. 2.4a. The position at which $dv/dr = 0$ in Fig. 2b is found as r_0 and then τ_0=$r_0\tau_w/R$.

The numerical derivative of the velocity profiles for the radial position may be calculated by central difference approximation as show below:

$$\left(\frac{\partial u_z}{\partial r}\right) = \frac{1}{2}\left(\frac{u_{i+1} - u_i}{r_{i+1} - r_i} + \frac{u_i - u_{i-1}}{r_i - r_{i-1}}\right) \tag{2.15}$$

where u_i indicates the local axial velocity at the radial position, r_i, respectively ($i = 1, ...N$, where N indicates the total points in the experimental velocity profile). This method was used in the present study to obtain the yield stress of the fluids used.

2.2.3 Hagen-Poiseuille flow in the presence of wall slip

The fully developed, steady flow of an incompressible fluid in a tube of radius, *R*, is shown in Figure 2.5a. The flow is caused by the pressure difference imposed across the two ends of the pipe. Since there is no angular velocity and the fluid is flowing at a steady-state, the linear momentum balance (in the direction of flow, *z*) on a fluid element ABCD of radius *r* and length *l*, may be written as:

$$p\left(\pi r^2\right) - (p + \Delta p)\,\pi r^2 = \tau_{rz} 2\pi r L \tag{2.16}$$

solving for τ_{rz},

$$\tau_{rz} = \left(\frac{-\Delta p}{L}\right)\left(\frac{r}{2}\right) \tag{2.17}$$

Equation. 2.17 shows the linear variation of the shear stress across the tube cross-section, increasing from zero at the axis of the tube to a maximum value at the wall of the tube. It should be emphasized here that equation Eq. (2.17) is applicable to both laminar and turbulent flow of any incompressible fluid in steady, fully developed conditions since it is based merely on a force balance and no assumption has been made regarding either the type of fluid or the flow pattern. Equation (2.17) thus provides a convenient basis for determining the shear stress at the wall of the tube τ_w as:

$$\tau_w = \left(\frac{-\Delta p}{L}\right)\left(\frac{R}{2}\right) \tag{2.18}$$

The shear stress may then be evaluated in terms of the shear rate at the wall, $\dot{\gamma}_w$ or $(-du_z/dr)_w$ to yield steady shear stress–shear rate data for a fluid. This relationship may be obtained, however, because the *z*-component of the velocity is a function only of the radial coordinate, this is, $u_z(r)$. The volumetric flow rate through the annulus is formed by two concentric fluid elements at radial positions of *r* and (*r*+*dr*), as shown in Fig. 2.5b.

The volumetric flow rate is given by:

$$dQ = 2\pi r u_z(r) dr \tag{2.19}$$

Figure 2.5 – Sketch of a steady unidirectional laminar flow for time-dependent fluids in a circular pipe.

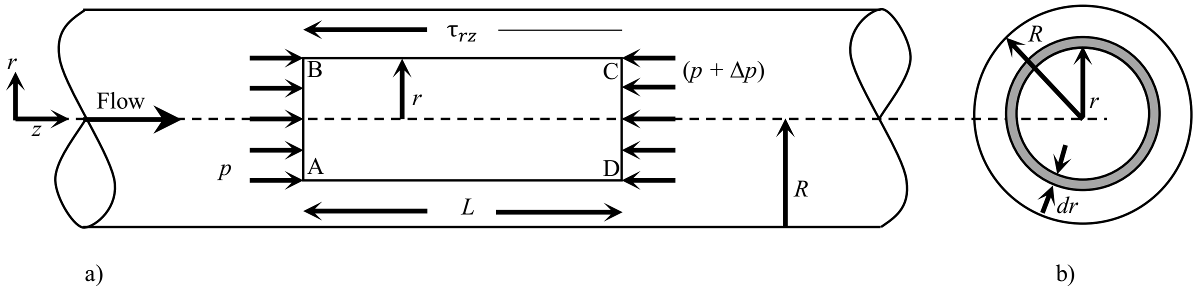

Source: Retrieved from Chhabra and Richardson (2011).

For the sake of simplicity, $u_z(r)$ will now be written as u_z. The total volumetric flow rate is obtained by integrating Eq. (2.19) over the cross-section of the tube as:

$$Q = \int_0^R 2\pi r u_z dr \tag{2.20}$$

Carrying out the integration in Eq. (2.20) by parts

$$Q = 2\pi \left\{ \left[\frac{r^2}{2} u_z \right]_0^R + \int_0^R \frac{r^2}{2} \left[\frac{-du_z}{dr} \right] dr \right\} \tag{2.21}$$

First the no-slip condition at the wall of the tube, i.e., $u_z = 0$ when $r = R$, the first term on the right-hand side of Eq. (2.21) is identically zero at both limits of integration. Thus, Eq. (2.21) simplifies to:

$$Q = \pi \int_0^R \frac{r^2}{2} \left[\frac{-du_z}{dr} \right] dr \tag{2.22}$$

It is then necessary to make assumptions regarding the nature of the flow and of the characteristics of the fluid. For a laminar flow time-independent fluids, the shear rate (-du_z/dr) is determined only by the value of the shear stress, i.e. the corresponding value of τ_{rz}. Thus, without any loss of generality, it is convenient to write this functional relationship as:

$$\frac{-du_z}{dr} = \mathbf{f}\tau_{rz} \tag{2.23}$$

where f is a unspecified function. Also, combining Eq. (2.17) and Eq. (2.18):

$$\frac{\tau_{rz}}{\tau_w} = \frac{r}{R} \tag{2.24}$$

On differentiation (for constant values of R and τ_w),

$$dr = \left(\frac{R}{\tau_w} \right) d\tau_{rz} \tag{2.25}$$

Now substituting Eq. (2.23-2.25) into Eq. (2.22), the volumetric flow rate Q is now given as:

$$Q = \frac{\pi R^3}{\tau_w^3} + \int_0^{\tau_w} \tau_{rz}^2 f(\tau_{rz}) d\tau_{rz} \tag{2.26}$$

Equation (2.22) can be used in ways: 1) By integration directly for a specific fluid model and 2) to establish general shear stress-shear rate characteristics of a time-independent fluid to developed rheological data for a fluid. For this study, only the first way will be developed, but before of integrating Eq. (2.26) and find the final expressions of the velocity for the laminar flow of Herschel–Bulkley model fluids, the contribution of wall slip to the flow rate is analyzed. It is customary (MOONEY, 1931) to quantify the slip's effect by assuming that a slip velocity, u_s, exists at the wall. Figure Fig. 2.6 shows the displacement flow of a yield stress fluid under a driving pressure drop. This implies that at the tube wall ($r = R$), the fluid has a velocity u_z=u_s instead of $u_z = 0$.

Figure 2.6 – Axisymetric Poiseuilli flow of a yield stress fluid at steady-state. Here, u_z is the velocity profile, u_{zp} is the plug velocity, u_s is the wall slip velocity, and τ_{rz} is the shear stress.

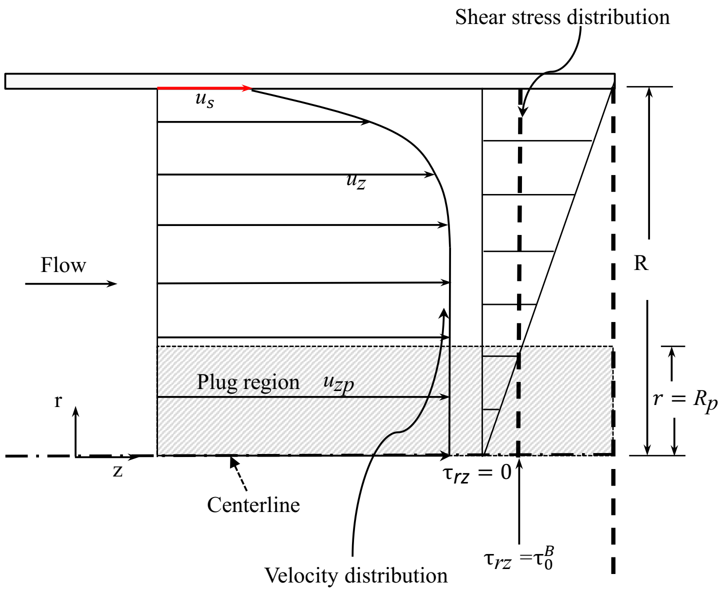

Source: Adapted from Chhabra and Richardson (2011).

From Eq. (2.21) when the fluid is flowing at a slip velocity u_s at the wall, the yields:

$$Q = \pi R^2 u_s + \pi \int_0^R r^2 \left[\frac{-du_z}{dr}\right] dr \tag{2.27}$$

On the right-hand side of Eq. (2.27), the two terms can se indetified as the contributions to the total flow rate stemming from slip (Q_s) and that occurring when there is no-slip (Q_{ns}). The Q_{ns} would still be expected to be given by Eq. (2.26), which is only a function of the wall shear stress, τ_w. Furthermore, the slip velocity is generally assumed to be a function of the wall shear stress only, albeit there is some evidence that it might be a function of tube diameter also (JASTRZEBSKI, 1967). Equation (2.27) can therefore be rearranged as:

$$\frac{Q}{\pi R^3 \tau_w} = \frac{u_s}{R\tau_w} + \frac{Q_{ns}}{\pi R^3 \tau_w} \tag{2.28}$$

Re-writing Eq. (2.28) in terms of the apparent wall shear rate:

$$\left[\frac{8u}{D}\right]\frac{1}{\tau_w} = \frac{8u_s}{D\tau_w} + \frac{32Q_{ns}}{\pi D^3 \tau_w} \tag{2.29}$$

where $u = Q/\pi R^2$ and D is pipe diameter. The term $(8u/D)$ is the nominal (or apparent) shear rate, and is the result of the application of Leibnitz's rule for Eq. (2.26) (for better understanding the reader is referred to Chhabra and Richardson (2011)). In the present study tThe shear rate at wall is derived from the velocity gradient (PIV system), which is estimated by comparing neighboring vectors with each other. A central difference scheme is used, and the resulting gradient corresponds to the slope of a 2^{nd} polynomial (i.e. parabolic) fit to three neighboring velocities, and therefore with 2^{nd} accurate. Then the gradient at the point (m, n) of the velocity component U in the direction x will be calculated as follows:

$$\frac{\partial U}{\partial x}(m,n)_{Central} \cong \frac{U_{m+1n} - U_{m-1n}}{x_{m+1n} - x_{m-1n}} = \frac{U_{m+1n} - U_{m-1n}}{2\Delta x} \tag{2.30}$$

Then, the shear rate at the wall was determined by averaging of the polynomial fits (Eq. (2.31)) of the values close to the wall on two sides of the velocity gradients. We have used a classical Levenberg-Marquardt iteration algorithm, implemented under Matlab® and OriginLab® software to obtain this values.

$$y = ax^2 + bx + c \tag{2.31}$$

Now we focus on the pipe flow for a yield stress fluid. According to Chhabra and Richardson (2011), it is possible to calculate the expressions of velocity and flow rate for the Bingham model from Eq. (2.26) and extend them to a Herschel-Bulkley fluid. Then, the Eq. (2.10)

$$\tau_{rz} = \tau_0^B + \eta_B\left(-\frac{du_z}{dr}\right) \tag{2.32}$$

Combining equations Eq. 2.17 and Eq. 2.32 and integrating concerning r, results in the following expression for the velocity distribution:

$$u_z = -\frac{1}{\eta_B}\left\{\left(-\frac{\Delta p}{L}\right)\frac{r^2}{2} - r\tau_0^B\right\} + C \tag{2.33}$$

where *C* is a constante.

At the walls of the circular pipe, when $r = R$, the velocity u_z must be zero in order to satisfy the no-slip condition. Substituting this value by u_z at $r = R$ in the equation Eq. 2.33, the value obtained for the constant is:

$$Constant = \frac{1}{\eta_B}\left\{\left(-\frac{\Delta p}{L}\right)\frac{R^2}{2} - R\tau_0^B\right\} \tag{2.34}$$

and, therefore, velocity distribution in the full viscous state is described by:

$$u_z = \left(-\frac{\Delta p}{L}\right)\frac{R^2}{4\eta_B}\left(1-\frac{r^2}{R^2}\right)-\frac{\tau_0^B}{\eta_B}R\left(1-\frac{r}{R}\right) \tag{2.35}$$

Which is valid only when $|\tau_{rz}| > |\tau_0^B|$ and $r \geq R_p$. The velocity in the plug flow region, $0 \leq r \leq R_p$ is obtained by substituting $r = R_p$, in Eq. 2.35, where is obtained:

$$U_{zp} = \left(-\frac{\Delta p}{L}\right)\frac{R^2}{4\eta_B}\left(1-\frac{R_p}{R}\right)^2 \tag{2.36}$$

To obtain the volumetric flow rate Q, the following integral is evaluated

$$Q = \int_0^R 2\pi r u_z dr = \int_0^{R_p} 2\pi r u_z dr + \int_{R_p}^R 2\pi r u_z dr \tag{2.37}$$

Performing substitutions for Eq. (2.35) and Eq. (2.36) is obtained the expression

$$\begin{aligned} Q = &\int_0^{R_p}\left(-\frac{\Delta p}{L}\right)\left(-\frac{R^2}{4\eta_B}\right)\left(1-\frac{R_p}{R}\right)^2 2\pi r dr \\ &+\int_{R_p}^R\left[\left(-\frac{\Delta p}{L}\right)\left(-\frac{R^2}{4\eta_B}\right)\left(1-\frac{r^2}{R^2}\right)-\frac{\tau_0^B R}{\eta_B}\left(1-\frac{r^2}{R^2}\right)\right]2\pi r dr \end{aligned} \tag{2.38}$$

calculating the integrals in Eq. 2.38 is obtained the expression

$$\begin{aligned} Q = 2\pi\left[\frac{-\Delta p}{L}\right]\left[\frac{R^2}{8\eta_B}\right]\left[1-\frac{R_p}{R}\right]^2\left\{\frac{r^2}{2}\right\}_0^{R_p} + 2\pi\left[\frac{-\Delta p}{L}\right]\left[\frac{R^2}{8\eta_B}\right]\left\{\frac{r^2}{2}-\frac{r^4}{4R^2}\right\}_0^{R_p} - \\ 2\pi\frac{\tau_0^B R}{\eta_B}\left\{\frac{r^2}{2}-\frac{r^3}{3R}\right\}_0^{R_p} \end{aligned} \tag{2.39}$$

Now writing $\tau_0^B/\tau_w = R_p/R = \phi$, the equation Eq. 2.39 is reduced to:

$$Q = \frac{\pi R^4}{8\eta_B}\left(-\frac{\Delta p}{L}\right)\left[2\phi^2\left(1-\phi\right)^2+2\left(1-\phi^2\right)-\left(1-\phi^4\right)-8\phi\left(\frac{1-\phi^2}{2}-\frac{1-\phi^3}{3}\right)\right] \tag{2.40}$$

For better presentation Eq. 2.40 can be reduced, and the volumetric flow rate is expressed as:

$$Q = \frac{R^4}{8\eta_B}\left(-\frac{\Delta p}{L}\right)\left(1-\frac{4}{3}\phi+\frac{1}{3}\phi^4\right) \tag{2.41}$$

Rewriten Eq. 2.41 in terms of the mean velocity, $\bar{U} = Q/\pi R^2$,

$$\bar{U} = \frac{(D/2)^2}{8\eta_B}\left(\frac{-\Delta p}{L}\right)\left\{1-\frac{8}{3}\frac{\tau_0^B}{f\rho\bar{U}^2}+\frac{1}{3}\left(\frac{2\tau_0^B}{f\rho\bar{U}^2}\right)^4\right\} \tag{2.42}$$

where f is the friction factor given as:

$$f = \frac{\tau_w}{\left(\frac{1}{2}\right)\rho \bar{U}^2} \tag{2.43}$$

As was mentioned above, this analysis can apply readily to the laminar flow of Hershel-Bulkley model from Eq. 2.11, and the resulting final expressions for the point velocity, the plug velocity, and volumetric flow rate (BIRD et al., 1983; DAMIANOU et al., 2014)

$$u_z = \frac{nR}{(n+1)}\left(\frac{\tau_w}{k}\right)^{1/n}\left\{(1-\phi)^{(n+1)/n} - \left(\frac{r}{R}-\phi\right)^{(n+1)/n}\right\} \tag{2.44}$$

The plug velocity, u_{zp} is given as:

$$u_{zp} = \frac{nR}{(n+1)}\left(\frac{\tau_w}{k}\right)^{1/n}(1-\phi)^{(n+1)/n} \tag{2.45}$$

and the volumetric flow rate Q, as:

$$Q = \pi R^3 n\left(\frac{\tau_w}{k}\right)^{1/n}(1-\phi)^{(n+1)/n}\left\{\frac{(1-\phi)^2}{3n+1} + \frac{2\phi(1-\phi)}{2n+1} + \frac{\phi^2}{n+1}\right\} \tag{2.46}$$

where ϕ for Herschel-Bulkley case is the ratio τ_0^H/τ_w. As the Bingham case, these expressions are implicit in the pressure gradient.

However, some dimensionless relations can be described for fluids through the Herschel-Bulkley model. When the viscosity varies as the fluid is deformed, an appropriate viscosity is necessary to define a generalized Reynold number for the different viscoplastic fluid. Then, te mean wall viscosity (η_w) is calculated form τ_w and using the Eq. (2.17) as:

$$\eta_w = m^{1/n}\frac{\tau_w}{(\tau_w - \tau_0^H)^{1/n}} \tag{2.47}$$

then, the expression of R_e can be generalized for non-Newtonian fluids as:

$$Re_g = \frac{\rho \bar{U} D}{\eta_w} \tag{2.48}$$

The Eq. (2.17), Eq. (2.47) can be replaced at Eq. (2.48), and its obtained a nwe general expression for R_e, given by:

$$Re_g = \frac{\rho \bar{U}^2}{\tau_w} \tag{2.49}$$

This expression is the most suitable to calculate the R_e, for Hershel-Bulkley fluids at laminar regime.

Finally, and according to Poumaere et al. (2014), Damianou et al. (2014), and Liu and Bruyn (2018) the equation of velocity for Herschel-Bulkley fluid in the presence of wall slip can be expressed as:

$$u = u_s + \left\{\begin{array}{ll} \frac{nR}{(n+1)}\left(\frac{\tau_w}{k}\right)^{1/n}(1-\phi)^{(n+1)/n} & \text{for } |\mathrm{r}| < \mathrm{R_p} \\ \frac{nR}{(n+1)}\left(\frac{\tau_w}{k}\right)^{1/n}\left[(1-\phi)^{(n+1)/n} - \left(\frac{r}{R}-\phi\right)^{(n+1)/n}\right] & \text{otherwise} \end{array}\right\} \tag{2.50}$$

where u_s is the wall slip velocity in $r = \pm R$. The wall slip velocity is obtained by extrapolating polynomial fit given by Eq. 2.51. We have used a classical Levenberg-Marquardt iteration algorithm, implemented under Matlab® and OriginLab® software.

$$y = ax^2 + bx + c \tag{2.51}$$

2.3 Particle Image Velocimetry Technique

In the field of fluid dynamics, highly accurate experiments are indispensable for a better understanding of complex flow phenomena. To meet these needs, various computational methods and sophisticated techniques have been devised and developed in recent years to advance the experimental investigation of flow fields. Particle Image Velocimetry (acronym PIV), it is one of the technique developed and has become an essential measurement technique in fluid mechanics laboratories in both research institutes and industry. This technique is particularly promising because it can instantaneously provide comprehensive and quantitative information about the whole flow field, its primary advantage being the ability to capture spatial velocity distributions simultaneously and non-invasively to study the structure of fluid flow. (STAMHUIS, 2006; RAFFEL et al., 2018).

The PIV technique allows to measure flow velocity at many locations simultaneously, making it a unique diagnostic tool to measure flow structures in different settings. Then, the velocity profile of the flow field is determined by first digitally recording particle (microspheres or bubble) images within the flow over multiple successive video frames and then conducting flow pattern identification and analysis of the data (GREATED et al., 1993).

2.3.1 Principle of Particle Image Velocimetry (PIV)

In the following, the basic features of the Particle Image Velocimetry (PIV) measurement technique will be described briefly. The experimental set-up of a PIV system typically consists of several subsystems.

- Seeding: when particles have a good traceability behavior to a fluid flow, the particle velocities usually represent the local fluid velocities. The small particles seeded in the fluid to trace its flow should (a) be distributed as homogeneous as possible in the fluid. (b) be well reflecting, (c) accurately follow the motion of the fluid, (d) not alter the properties of the fluid and its flow.
- Illumination: the flow field of light scattering tracer particles is illuminated by a uniform light sheet. Usually, the light source is a laser, whose beam is guided by a triangular prism and a cylindrical lens. The tracer particles in the flow field have to be illuminated at least twice within a short and known time interval.
- Recording: the images of particle motions following the fluid flow are recorded by high-resolution camera. In general, accurate velocity measurements require a short time interval Δt between two consecutive images. The optical axis of the camera lens must be perpendicular to the plane of the light sheet. However, it is difficult to set up the camera precisely. Hence, the camera should be calibrated to determine its parameters before photographing.

- Calibration: in order to determine the relationship between the particle image displacement in the image plane and the tracer particle displacement in the flow, a calibration is required.
- Evaluation: the displacement of the particle images between the light pulses has to be determined through evaluation of the PIV recordings.
- Post-Processing: image processing is the most critical stage in a PIV measurement. First, the images that record the particles' motion are transmitted to a converter to obtain digital images. Then, the digital images are processed. The processing includes removing noise, smoothing, converting the gray-scale images to binary images, labeling the particles, and calculating the center of gravity coordinates of the particles. Then, the coordinates of the particles are transferred from the image plane to the physical plane. Finally, the particle velocity vectors are calculated.

Figure 2.7 – Experimental arrangement for planar 2D PIV in a wind tunnel.

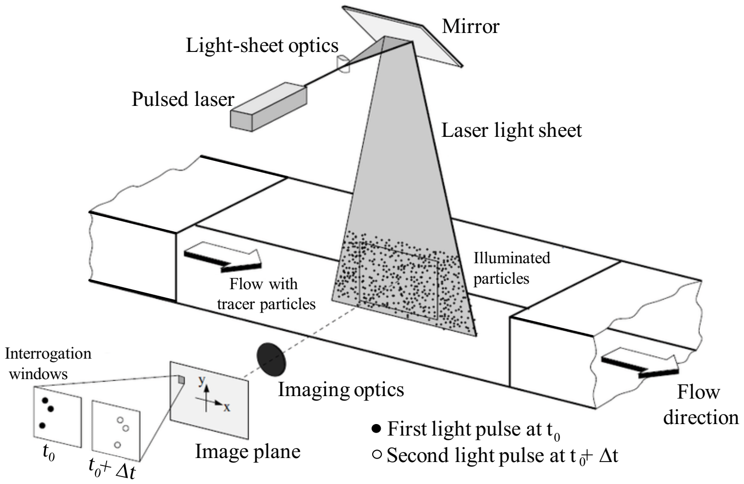

Source: Retrieved from Raffel et al. (2018).

Then, based upon the definition of velocity, i.e., the first derivative of position with respect to time, the technique consists of measuring the displacement of fluid (Δx) over a given time interval (Δt). The position of the fluid is imaged through the light scattered by liquid or solid particles illuminated by a laser light sheet. In most applications, such particles are not naturally present in the flow which has to be seeded with tracer particles, assumed to be sufficiently small and light to move with local flow velocity. Figure 2.7 briefly sketches a typical set-up for PIV recording of two velocity components within the flow field. A plane within the flow is illuminated twice fusing two superimposed laser light sheets. The light scattered by the particles is recorded on two separate frames on a special camera sensor. The digital PIV recording is divided into small areas called "interrogation windows".

The local displacement vector of the particle images between the two illuminations is determined for each interrogation window utilizing a spatially statistical correlation function. Given the time interval between the two laser pulses and the image magnification obtained from camera calibration, the projection of the local flow velocity vector onto the plane of the light sheet, attributed to the center of the interrogation window, can then be deduced. Finally, each velocity vector forms a flow velocity vector map as shows in Fig. 2.8.

Figure 2.8 – Velocity field calculated using cross-correlation algorithms.

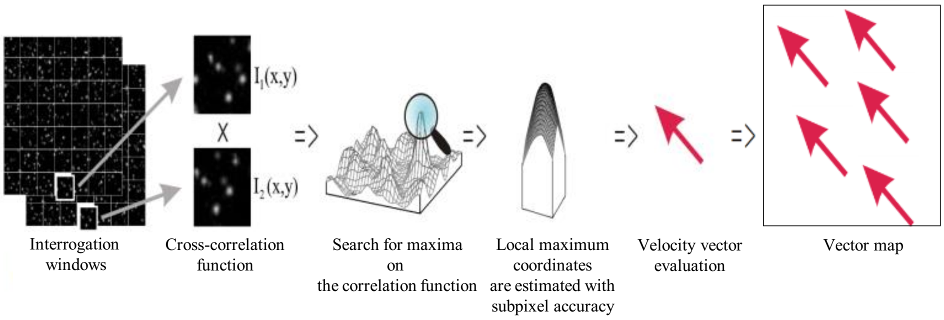

Source: Retrieved from Siberian Branch of the Russian Academy of Sciences.

It is noteworthy that the major merit of the PIV technique is its capacity to deliver a quantitative and instantaneous measurement of the velocity not only at one point, like Laser Doppler Velocimetry, but over a whole plane simultaneously: both visualization and quantification of the 2D flow structure become available. This, together with advances in electronic imaging and computing tools explains its success over the past two decades.

2.4 Chapter summary

In this chapter, the concepts of viscosity and shear stress were discussed and the behavior of fluids was classified as Newtonian and non-Newtonian. The Bingham and Herschel-Bulkley rheological models were described as the most suitable for fit the viscoplastic behavior of a non-Newtonian fluid. The volumetric flow rate and velocity profile equations were presented for Hagen-Poiseuille flow in the presence of wall slip for viscoplastic fluids. On the other hand, some of the main wall slip mechanisms in the pipe flow were exposed, their relationship with non-Newtonian fluids was described, and a method to calculate the yield stress in the presence of this phenomenon was presented.

Finally, a brief explanation of PIV technique was also presented in order to highlight the importance of using this technique for the visualization of fluid flows in experimental studies, and was an emphasis on the potential of the PIV can be shown to provide detailed, qualitative and quantitative information on flow structure.

3 LITERATURE REVIEW

In this chapter, a brief review of rheometric studies evaluating the rheological properties of viscoplastic fluids is presented. Subsequently, studies involving the start-up flow of yield stress in different experimental configurations are discussed. Finally, this chapter discussed relevant works that use visualization techniques to study the dynamics of viscoplastic fluids in pipes.

3.1 Carbopol® -rheometric studies

One of the main rheological properties that must be determined for viscoplastic fluids through rheometric studies is the yield stress. There are many methods to determine this value, but none is recognized as a standard procedure (DZUY; BOGER, 1983; NGUYEN; BOGER, 1992; PASHIAS et al., 1996; LARSSON et al., 2013; DINKGREVE et al., 2016; MALKIN et al., 2017). Some studies measuring the yield stress and other rheological properties of carbopol solutions can be found in the literature.

Roberts and Barnes (2001) obtained steady flow curves of aqueous Carbopol® for a range of concentrations from 0.045 to 1.0wt%, through a controlled stress rheometer. The results showed that the viscosity of solutions decreased when shear stress increased beyond the critical range and this decrease could be caused by the breakdown of microgel structure being unstructured progressively as the shear stress is increased. This would explain slip effects, which are the usual cause of problems at smooth walls (BARNES, 1995). On the other hand, the steady flow curves obtained for each solution showed an abrupt transition with a decrease of concentration over a relatively narrow range of shear stress. The results were fitted to the Herschel-Bulkley model, which assumes apparent yield stress.

Benmouffok-Benbelkacem et al. (2010), investigated the viscoelastic properties outside the linear viscoelastic regime and above yield stress, performing rheologic tests in yield stress fluids. The results showed that the Carbopol® have an almost constant elasticity below and above the yield stress, even for applied stresses several times larger than the yield stress, i.e., the elasticity module far from disappearing when the material starts to flow, stays remarkably constant. This finding can be mainly observed in the Carbopol® flows in pipes, where for shear stresses low than the yield stress of the material, oscillatory behavior and flow reversal movement are observed (LIU; BRUYN, 2018).

Poumaere et al. (2014) analyzed an unsteady rheometric flow between parallel plates (smooth and serrated) for Carbopol® solution 0.3 wt% (Carbopol® 980 provided by BF Goodrich). The material presents low thixotropy, and deviate slightly from the behavior of an ideal viscoplastic fluid. Also, with the smooth parallel plate geometry, slip in the wall was observed, and the apparent yield stress measured is nearly an order of magnitude smaller than cross-hatched parallel plates geometry (no slip). The authors mainly report that independent of the slip condition, three deformation regimes as a function of shear stress are identified: Solid (F), low shear stress, solid-fluid transition (S+F), shear stress slightly greater than the stress yield, and completely fluid, for shear stresses beyond yield stress. This finding is consistent with the deformation regimes reported by Putz and Burghelea (2009), in rheometric tests performed with Carbopol® solution.

Dinkgreve et al. (2017), studied the response of yield-stress material Carbopol® to examine the response of the Carbopol to a variety of deformations to elucidate how the mechanics of the unyielded material manifest themselves in some standard rheological tests. The results obtained showed that for the simple yield-stress fluid considered, the transition appears to be based on a critical strain, with the possibility of dissipative deformations in a viscoelastic solid that make the critical stress under transient conditions deformation dependent. From the results, it was also possible to elucidate that the appearance of a Newtonian fluid regime at stresses below the yield stress is an artifact that would be observed with the simplest viscoelastic solid representation, namely a Kelvin–Voigt solid. This fact may indicate that the fluid may suffer state changes during its yielding process.

A common phenomenon and some times ignored in the rheometric studies of yield stress materials are the slip in the wall, which causes practical difficulties during the experiments and simultaneously introduces large errors in the yield stress calculation results. Several signatures reveal the existence of movement about the solid surface when the applied stress is less than the yield stress, which avoids observing the true behavior of yield stress material (WALLS et al., 2003; SOCHI, 2011).

3.2 Studies involving the start-up flow in the experimental setup

A fluid that is initially at rest and then is restarted has been the theme of study for many years. One of the first to analyze this problem was Stokes when proposing the solution of a viscous impulse-driven fluid (BROMWICH, 1930). Sometimes later, a fluid start-up flow of Newtonian fluid in a circular pipe displaced by the imposition of pressure, was studied by Szymanski (1932). These studies showed that the start-up flow of Newtonian fluid is controlled by viscosity. In the case of Carbopol® and other viscoplastic fluids, elasticity and the yield stress play an important role. In this way, a better understanding of it is rheological behavior due to it is industrial importance aroused the interest of researchers.

Sierra et al. (2016) evaluated the start-up flow of a yield stress fluid in an experimental setup. Carbopol® solutions were displaced by a Newtonian fluid, under application of several pressure rates until start-up flow. The minimum pressure required to restart the flow was obtained, and the results showed good agreement between the rheological measurements and experimental. The authors also reported two crucial aspects: the first is related to the start-up time of the fluids, which varies depending on the viscosity. In their tests, they observed that the start-up time for the fluid with the highest viscosity was 2.5 times longer compared to the fluid with the lowest viscosity. The second aspect involves the avalanche effect (COUSSOT et al., 2002), i.e., where initially, the elasto-viscoplastic fluid is fully structured at rest. Then, it is subjected to a stress that increases linearly until it exceeds the yield stress, and eventually, the gelled fluid microstructure collapses.

In a study performed through a helical pipeline and assuming non-slip conditions in the pipeline, Mitishita et al. (2018) evaluated pressure transmission and pressurization in glycerine and Carbopol® solutions. The glycerine solution showed that the pressure is fully transmitted in Newtonian fluids, remaining uniform during pressurization. For Carbopol® gel, the pressure distribution is not uniform and with the increased yield stress of material during fluid pressurization, the pressure gradually increases from the inlet to the outlet of the coil. The authors also concluded that the fluid elasticity seems to play a role when the pressure starts to propagate along the pipeline. As the time elapses, the elasticity fades, and the pressure propagation evolves based on two concurrent effects: pressure wave inertia and viscous dissipation.

Pereira et al. (2019), using the same experimental setup as Mitishita et al. (2018), studied the start-up flow of distilled pure glycerine and a Carbopol aqueous solution and evaluated the viscous and viscoplastic effects during the start-up flow. Tests were performed by applying volumetric flow rates. The compressibility of the material influences the restart of flow, because the material only flows after a uniform pressure drop is established in the pipe. In the case of glycerine, the gradient is almost immediate. In contrast to the Carbopol aqueous solution, where it is observed that the response of the material indicated a significant delay about the evolution of pressure. These pressure transmission results are in good agreement with Mitishita et al. (2018). The experimental results for both fluids were compared with the De Oliveira model (OLIVEIRA; NEGRAO, 2015), and a good agreement was observed.

Finally, Abedi et al. (2019), investigated the non-thixotropic behavior of hair gel (Carbopol®) in the start-up flow. In a flow loop with a roughened inner surface, the viscoplastic fluid was displaced by application a fixed pressure value for a certain time until flow start-up. The minimum pressure drop required for the start-up flow of viscoplastic fluid was obtained, and this value was consistent with the results of the yield stress determined in rheometrical experiments and the force balance that relates the yield stress to the pressure drop. However, the authors reported an interesting fact, that for the viscoplastic fluid tested, the equation of the balance of forces $\tau_0 = R\Delta p_{min}/2L$ is not satisfied with precision when the R equal to the radius of the pipeline. This disagreement is explained because the viscoplastic fluid does not flow through the valleys of the pipe. According to his report, the force balance equation is only satisfied with accuracy when the peak-to-peak radius of the rough pipe is used. This fact is controversial because a rough pipe should, in theory, avoid slip and the true yield stress would be found.

An essential result of the investigations performed is the unequivocal evidence of the existence of yield stress (BARNES, 1999; ROBERTS; BARNES, 2001; PHAM et al., 2006; DIVOUX et al., 2011), but the knowledge about the dynamics of the yielding transition is a topic that is still being studied (PUTZ; BURGHELEA, 2009). Particularly the interest for researchers and theorists focuses on realistic flow situations that normally involve the phenomenon of the wall slip, as in the case of pasty materials, dispersions, among others. This fact brings additional experimental and theoretical difficulty in exploring the solid–fluid transition and modeling realistic flows of such materials in industrially relevant settings (POUMAERE et al., 2014).

3.3 Visualization of viscoplastic fluid flow by PIV technique

As it was presented in the previous sections, rheometric studies and experimental configurations are used to investigate the influence of yield stress and other rheological properties on the start-up flow viscoplastic fluids in pipes. However, analyze the flow kinematics of these fluids is also vital to better understand the rheological behavior. Flows of viscoplastic fluids in circular and concentric pipes have been studied for many years (FORDHAM et al., 1991). The main interest to better understand the flow dynamics of these materials is motivated mainly by performance in the oil and gas industry (LITVINOV; FILATOV, 1980). But, to analyze the flow kinematics, visualization tools are necessary, the first investigations of the visualization of flow are from 1867, using the High-Speed Photography technique (TASAKA et al., 1867). But it is in 1997 when Particle Image Velocimetry (PIV) was used for the first time (RAFFEL et al., 2018).

Pérez-González et al. (2012) studied the flow of Carbopol® in a sliding capillary using the technique Particle Image Velocimetry (PIV). They concluded that the yield stress to start the flow obtained from the velocity profiles follows the trend of the rheometrical ones very well. Experimental observations also indicated that the slip increases with increasing shear stress.

In Taghavi et al. (2012) the displacement of Carbopol® by a Newtonian fluid in slightly inclined tube was studied. The displacement occurs only by gravitational effects. The Ultrasonic Doppler Velocimeter (UDV) technique was used to obtain the velocity profiles and characterize the different aspects of start-up flow. Two flow regimes were identified, one of the central type, where the displacing fluid propagates along the center of the tube and another in which the displacement fluid moves along the lower generatrix of the tube. Subsequently, Alba et al. (2013) extended the study to other slopes, identifying a third regime referred to as turbulent-mixed flow. In this case, despite the yield stress, the flow is very similar to that for a Newtonian displacement. In both investigations, static residual viscoplastic layers were reported that played an essential role in the flow dynamic characterization that was consistent with instability identified in the deformation regimes. Using the same technique to measure velocity profiles for the Carbopol solution flow but in a horizontal pipeline Moisés et al. (2018) analyzed the start-up flow. In his work, they reported that for $t < 0$, the velocity was zero for each value of r, but for $t \approx 0$ a short and abrupt transient response is observed. In steady-state, the flow was characterized by present a plug region in the center of the pipe, i.e., plug velocity. On the other hand, when the r approached the pipe's radius, the velocity tends to zero. In contrast to Taghavi et al. (2012) and Alba et al. (2013), the authors did not report phenomena that affected the dynamics of the flow.

Poumaere et al. (2014) studied yielding of unstable laminar flows of yield stress fluid (Carbopol®980) using a horizontal experimental setup and a Digital Particle Image Velocimetry (DPIV) system. The results of the characterization of the flow fields using the PIV technique showed several flow regimes as a function of the applied pressure. Corresponding to the lowest values pressure a solid-like flow regime was observed. This regime is characterized by an elastic solid plug and large fluctuations near the center-line. For the largest values of the pressure, a fluid regime is observed. Within this regime, a stable state is reached. However, the transition between the regime as solid-like regime to the fully yielded regime is not direct but mediated by an intermediate solid-fluid coexistence regime. Besides, the presence of wall slip during the entire yielding process is reported as the main characteristic, and that this phenomenon is scaled as a power-law with hydrodynamic quantities such as wall shear stress and velocity gradients in $r = R$.

Liu and Bruyn (2018) studied the displacement of Carbopol® 940 solutions by an immiscible Newtonian fluid from below at low and high volumetric flow rates in a vertical pipe with rough and smooth boundary conditions. The PIV technique was applied to measure the velocity field. The process of start-up flow with rough walls involved a long transient regime with several steps: elastic deformation, wall slip, yielded flow near the wall, and finally plug flow which is well described by the Herschel-Bulkley model. The applied shear stress presented results consistent with the obtained by rheometry when a rough tube was used. On the other hand, in the smooth inner tube, only the first two steps occurred, and the wall shear stress for flow start-up was substantially lower than the yield stress, possibly due to the response elastically to the applied pressure. Finally, the experimental results were compared with the elasto-viscoplastic model (MENDES; THOMPSON, 2013), and showed the same multi-step yielding process, and a good agreement was observed.

It is essential to highlight that the start-up flow of viscoplastic materials is a transient process and is directly influenced by rheological properties such as yield stress, elasticity, and phenomena such as wall slip and the avalanche effect. However, the main conclusion is that by visualizing the flow dynamics, it is possible to evaluate all these factors and obtain a start-up pressure value that is more consistent with realistic viscoplastic flows of industrial relevance. Table 3.1 presents a summary of works that use visualization techniques to analyze the start-up of flow and their main conclusions.

3.4 Chapter summary

This chapter presented the works that cover studies on rheometry and experimental setups with approach the PIV technique involving the viscoplastic fluids. Due to the complexity of the rheological behavior of viscoplastic fluids, the number of studies that use the PIV technique to analyze the start-up flow in experimental setups is smaller. Moreover, many researchers still ignore the phenomenon of wall slip in yield stress materials and its influence on the minimum pressure drop for restart flow, on the average flow velocity, and on the transition from a solid behavior to a viscous one (fully yielded), despite its omnipresent nature and tremendous importance from a fundamental and applied perspective. Based on the studies presented, it is possible to observe a knowledge gap in this area, in which the present study can contribute with experimental data as a source of validation for future experimental projects and numerical simulations, using as viscoplastic fluid a solution of a commercial gel (Ultrasound gel) composed by Carbopol®.

3.5 Specific objectives

Based on the literature review and the main objective determined in Chapter 1 (section 1.3), the specific objectives of this dissertation are to:

- Visualize and analyze the temporal evolution of the deformation fields and flow profiles in the presence of the wall slip in order to identify the flow regimes in the start-up of viscoplastic fluids as a function of the wall shear stress.
- Determine the dependence of the wall slip velocity on time, the velocity gradients at the wall, and with wall shear stress, to obtain a simple phenomenological picture of the slip phenomenon in viscoplastic fluids.
- Calculate the yield stress of viscoplastic fluids from the velocity profiles obtained by PIV technique and find a relationship between the behavior of plug radius and the wall shear stress.

Table 3.1 – Characteristics and main conclusions of studies that analyze the start-up flow of viscoplastic fluid in circular pipes by means of visualization techniques.

Author	Fluid analyzed	Technique used	Analisys	Conclusions
Taghavi et al. (2012)	Carbopol	Ultrasonic Doppler Velocimeter (UDV)	Displacement flows of a yield stress fluid by a Newtonian fluid, where the yield stress is significantly larger than a typical viscous stress in the displacing fluid.	1) Two flow regimes were observed a central-type regime that propagates along the centre of the pipe and slump regime where the displacing fluid moves along the bottom of the pipe. 2) Due to the great yield stress, in both regimes, it was found residual layers of displaced fluid present at long times and these residual layers are completely static.
Pérez-González et al. (2012)	Carbopol	Particle image velocimetry (PIV)	Flow kinematics of a yield-stress fluid in a capillary with slip at the wall.	1) It was found that flow behavior consists of a purely plug-like flow before yielding, followed by the solid-liquid transition when critical shear stress is exceeded. 2) The slip velocity was found to increase in a power-law way with the shear stress.
Alba et al. (2013)	Carbopol	Ultrasonic Doppler Velocimeter (UDV)	Displacement flows of a yield stress fluid by a Newtonian fluid for differents inclinations, where the yield stress is significantly larger than a typical viscous stress in the displacing fluid.	1) The flow regime is not determined for the inclination angle directly but it contributes to the range of secondary flow behavior observed at higher inclinations. 2) A turbulent/mixed regime was found, which is generated when the flow rate is high and buoyancy parameter Re cosbeta/Fr, is great sufficiently. 3) The viscoplastic layer presented a range of different behaviour, while more dense Newtonian fluid was to slump under the gel layer.
Poumaere et al. (2014)	Carbopol	Particle image velocimetry (PIV)	1) The solid-fluid transition of a no-Newtonian fluid observed during unsteady flow ramps in the presence of wall slip. 2) Unsteady yielding in a laminar unsteady pipe flow in the presence of wall slip by means pressure ramps.	1) With slip and no-slip, the transition from a solid behavior to a fully yielded, is not direct but mediated by an intermediate solid-fluid regime. 2) The slip velocity during controlled pressure ramps with various degrees of steadiness reveal a clear coupling between the irreversible solid-fluid transition and the slip phenomenon.
Liu and Bruyn (2018)	Carbopol	Particle image velocimetry (PIV)	Displacement of solutions of no-Newtonian fluid by an immiscible Newtonian fluid at low and high volumetric flow rate in a vertical pipe with rough and smooth boundary conditions	The start-up flow and yielding of Carbopol in rough vertical pipes require a lengthy transient with some steps: elastic deformation, the wall slip, yielding at the wall, and finally a steady-state plug flow that is well-described by the predictions of the Herschel–Bulkley model. While in the smooth pipe, the wall shear stress never exceeds the yield stress, so that only is observes elastic deformation followed by wall slip.

Source: Author (2021).

4 METHODOLOGY

The chapter describes the steps developed to meet the objectives set. These steps include the choice of fluids used in the experimental tests, an overview of the experimental setup, design and execution of the experiments, analysis of the data, and validation of the PIV methodology.

4.1 Working fluid

In choosing the fluids that were used as Newtonian fluid to validate the PIV methodology in the transient regime and as viscoplastic fluid to visualize the start-up of yield stress fluids, some considerations were made regarding viscosity, density, chemical compatibility, chemical stability, safety, and price. Finally, the index of refraction is also considered an important property in the study problem. The following section describes the fluids that will be used in the experimental tests and their preparation procedure, based on these considerations.

4.1.1 Glycerine

Glycerine, also known as glycerol, is a viscous substance, completely soluble in water and alcohols but is insoluble in hydrocarbons. In general, it has a unique combination of physical and chemical properties (Tab. 4.1). One of the most important physical properties is the variation in viscosity with temperature. According to Takamura et al. (2012), it is highly sensitive in the temperature range between 20ºC and 50ºC. Furthermore, due to its good optical transparency, stable properties, and Newtonian behavior, it is the ideal candidate to evaluate the transient regime methodology. In terms of production and costs, it is a product that does not require a complex process to produce and it is easy to buy in chemical product markets (BAGNATO et al., 2017). In the Center for Research in Rheology and Non-Newtonian fluids (CERNN) it is generally used to represent the behavior of a Newtonian fluid (PALACIOS, 2011; MITISHITA et al., 2017; PEREIRA et al., 2019). Therefore, pure glycerine was used for the purposes of this study. For the sake of simplicity throughout the text, it refers to pure glycerine as glycerine

4.1.2 Ultrasound gel

As shown in Table 4.2, the pH of the ultrasound gel is neutral and has a strong influence on Carbopol® stabilization, for that reason, distilled water with a pH closed to 7.0 used to formulate the solutions (ISLAM et al., 2004). A neutral pH guarantees a maximum initial viscosity and good stability for the fluid (GIUSEPPE et al., 2015). The process to obtain the fluids at this pH and concentration (50wt% and 25wt%) followed the steps described in Blanco (2019), where water was used as the binder fluid. Every solution was agitated for a least 12 hours to ensure the homogenization of the fluid and avoiding the absorption of humidity. Then, the recipient was covered, and the fluid was let to rest for 12 hours before starting the experimental tests to remove the air bubble that could be trapped into the solution during the homogenization process. A pH meter was used to check the pH during each stage of the solution.

Table 4.1 – Glycerine properties at 20 ºC.

General information	Composition	Glycerine 83.41 wt%, methanol (ND), Soap 1.28 wt%, Water 11.59 wt%, ash 2.69 wt%, others 1.03 wt%
	Toxicological	Acute toxicity
	Category	Flammable liquids
	Fire extinguishing agent	Foam, dry powder, carbon dioxide
Chemical-physical properties	pH	7.0 - 7.5
	Appearance	Colorless liquid (hygroscopic)
	Color	APHA: $\leq$ 20
	Density	1261 Kg/m^3
	Viscosity	1.069 Pa·s
	Surface tension	63.4 Mn.m^{-1}

Source: Retrieved from Liu et al. (2011), Pagliaro and Rossi (2010).

The ultrasound gel has high water solubility and neutral pH, so there were no changes in the pH value measured during the solutions' preparation.

After fluid preparation, rheological tests were performed on fluid samples, before each test, taken from the experimental setup to observe behavior viscoplastic and fluid stability. These tests were performed at a temperature of 22 °C, in order to represent the same conditions set in the laboratory. The procedure for performing the rheometric tests is detailed in section 5.2. Also, for the sake of simplicity, as described in 4.1.1, viscoplastic fluids with concentration 50wt% and 25 wt% were referred to throughout this document as fluid C-50 and C-25, respectively.

Table 4.2 – Ultrasound commercial gel properties.

General information	Composition	carboxivinyl polymer 5 wt%, purified water 91.5 wt% preservatives and thickening agent 3.5 wt%
	Toxicological	Not registered
	Ecologic information	Biodegradable product
Chemical - physical properties	pH	6.5 - 7.0
	Appearance	Crystal clear gel
	Density	950 - 970 kg/m^3
	Viscosity	44 - 48 Pa·s

Source: Retrieved from Clarke et al. (2007).

4.2 Refraction index

Concerning the PIV technique, an important property to allow the visualization of the fluid flow is the refraction index. The success of an exemplary data acquisition for this project depends on the refractive properties of the fluid and the visualization region (acrylic). The refractive index or index of refraction of a material is a dimensionless number that describes how fast light travels through the material. It is defined as:

$$n_{ref} = \frac{c}{v} \tag{4.1}$$

Where (c) is the velocity of light in vacuum and (v) is the velocity of light in the fluid. According to the studies performed with the PIV technique and related in the literature review, mostly experimental studies use transparent fluids and materials in the test section, to obtain the highest clarity of visualization of the study phenomenon. Table 4.3 shows the refractive index of the fluids that will be analyzed in this study and of the manufacturing materials of the test section.

Table 4.3 – Refractive properties of some materials and fluids for test regions in visualization studies.

Material/fluids	n_{ref}	Description
Borosilicate glass	1.47 – 1.49	Plates, Sheets, bars, tubes, and special forms
Acrylic	1.49	Plates, tubes, and bars
Water	1.33	Fluid
Glycerine	1.33 – 1.47	Fluid
Ultrasound gel solution	1.4 – 1.5	Gel or fluid

Source: Retrieved from Raffel et al. (2018), Nimdeo et al. (2016), .

For physical investigations executed with PIV technique, the ideal would be a perfect match between the sample fluid, the medium, and the material that delimitates the study fluid. From the information provided by Table 4.3, it can be seen that the refractive indexes of the sample fluids and the materials with which the test section was fabricated do not have a perfect relation, but they are close. Another possible difficulty is the pipeline curvature that also affects the flow visualization. These effects are shown in Fig.4.1.

Figure 4.1 – Simulation of ray paths for parallel light rays emitted vertically downwards and passing through a cylindrical sample of refraction index 1.5. (a) The sample is not surrounded by any matching fluid and the rays are severely refracted. (b) There is a perfect match between the surrounding fluid and the sample. (c) There is a 0.3% mismatch between the refractive indices of the fluid and the sample.

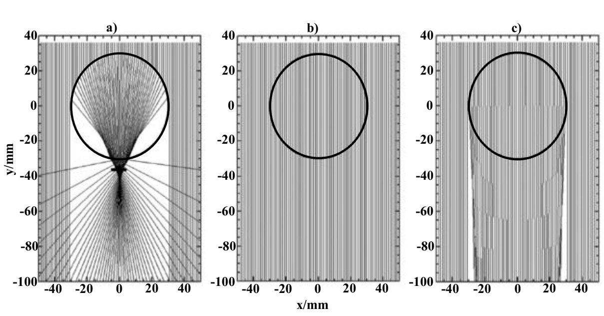

Source: Retrieved from Doran and Yatigammana (2012).

Fig.4.1(a), shows optical distortions are caused by the wall curvature effects and the different refraction indices. Fig.4.1(b) indicates that when the medium, the pipe, and the fluid inside the pipe have the same refractive index, there is no optical distortion of the light rays. Finally, Fig.4.1(c) reveals that the distortion of the light rays is not high and the mismatch between the refractive indices of the samples involved (medium, pipe, and fluid) is low.

As reported by Westerweel et al. (1996) the curvature of the pipeline affects the flow visualization, but this effect can be reduced using a water-filled box. This experimental study uses a test section immersed in water contained in a visualization box to reduce these effects and avoid distortion in the images (PALACIOS, 2011; BLANCO, 2019).

4.3 Experimental Setup

To achieve the main objectives, an experimental setup was designed to study the start-up flow of fluids C-50 and C-25. Fig.4.2 shows a schematic illustration that identifies the main components and the subcomponents of the experimental setup.

The experimental setup was installed in CERNN's non-Newtonian fluid flow laboratory (LabFlow). The device is basically made up of two systems: hydraulic and control/acquisition. Descriptions of the systems are detailed in the next section.

Figure 4.2 – Schematic illustration of the components of the experimental setup.

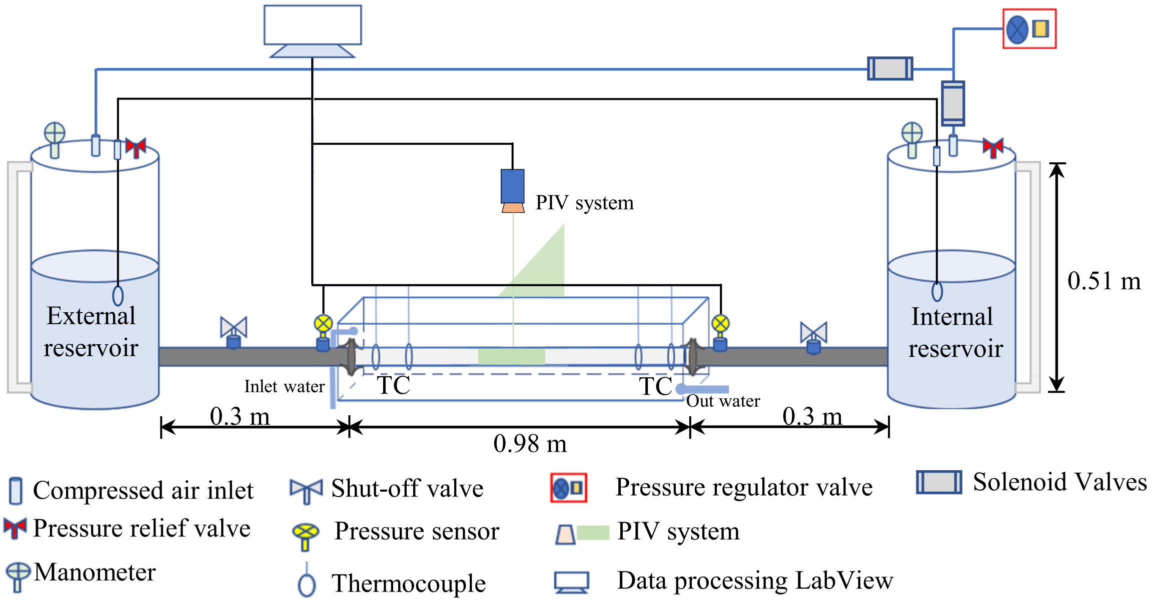

Source: Author (2021).

4.3.1 Hydraulic system

In this experimental setup, the hydraulic system is integrated into three parts: the main pipe, two axial pipes, and two reservoir tanks. Fig.4.3 details the parts that constitute each system of the experimental apparatus. The main pipe (Fig.4.3 - Item C) is constructed by a clear and extruded acrylic tube made of Polymethyl-Methacrylate (PMMA), which gives the acrylic tubes greater mechanical strength, transparency, and gloss. The tube has a length of 0.98±0.003 meters and an internal diameter of 0.022±0.002

meters. Additionally, two auxiliary sections (Fig.4.3 - Item B) made of PVC (Polyvinyl chloride), with a length of 0.3 meters, connect the main pipeline to the reservoir tanks.

Figure 4.3 – Schematic illustration of the components that constitute each system of the experimental setup.

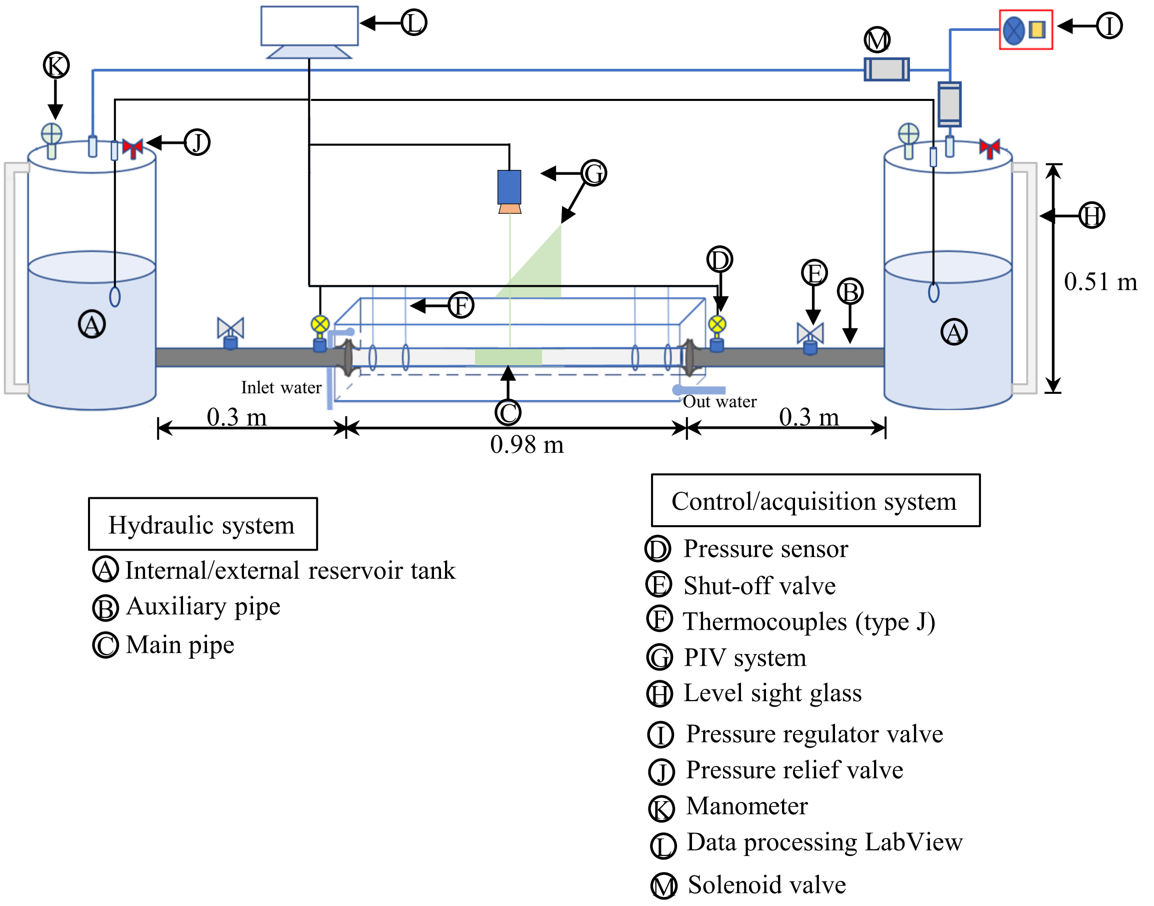

Source: Author (2021).

Two identical tanks (working pressure 1.6 bar), 5 liters each, made of Polypropylene (PP) were used to store the sample fluids (Fig.4.3 - Item A). Polypropylene is among the lowest specific weight thermoplastics (920 kg/cm^3) and the highest chemical resistance available. Hermetic to liquids and gases, it does not react with the mighty majority of industrial and pharmaceutical chemical agents. Maximum temperature of 120 ºC for some time according to the needs of the project. These tanks were identified the external tank and the internal tank. Therefore, the tank placed before the test section (right) was named the external reservoir tank (or external reservoir), and the opposite side (left) internal reservoir tank (or internal reservoir). Both tanks had a quick coupler adapter on the top cap for filling with compressed air, and also had manometer type Bourdon (Fig.4.3-Item K), model 213.54-E supplied by WIKA with 0 to 1.6 bar operating range, a pressure relief valve also supplied by WIKA model PN250 (Fig.4.3 - Item J and Fig.4.4 c) calibrated to operate up to 1.6 bar. Finally, to visualize the changes in the tanks' level due to the start-up of fluid, a level sight glass was installed (Fig.4.3 - Item H).

4.3.2 Measuring and control systems

The measuring and control systems (Fig.4.3) are made up of various devices to monitor the parameters of pressure and temperature. To record the pressure difference during the flow restart, two model P-30 pressure sensors (Fig.4.4 a) supplied by WIKA were used. These pressure sensor operate between a range of 0 to 0.6 bar and guarantees precision measurements with a maximum measuring deviation of as low as 0.05 % of span. To record the pressure variation, one was installed at the inlet and the other at the outlet of the tests section, next to the visualization box (Fig.4.3). The pressure signals were transmitted to a model NI9213 data acquisition module (Fig.4.4 h), provided by National Instruments.

Figure 4.4 – Instruments that constitute the measuring and control systems: a) pressure sensor, b) thermocouples (type J), c) manometer, d) pressure regulator valve, e) shut-off valves and f) pressure relief valve model PN250, g) selenoid valve, and h) data acquisition module.

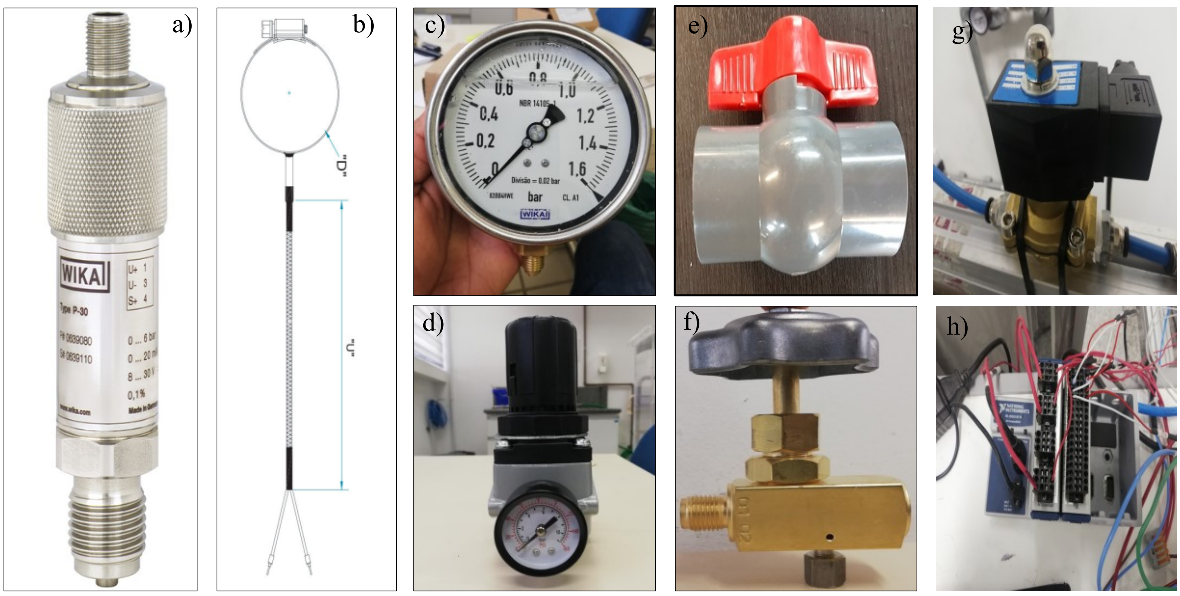

Source: Author (2021).

Temperature monitoring is done by four thermocouples (type J) (Fig.4.3 - Item F) with an operating range from -50 °C to 150 °C externally attached to the acrylic tube by clamps. Figure (4.4 b), it is possible to see a sketch of the thermocouple design that was custom-made by CAMPCONTROLES and was used in this study. Temperature information was captured by a NI9219 data acquisition module (Fig.4.4 h), supplied by National Instruments.

The pressurization system consisting of a pressure regulator valve WSCHOTT-1/2, model TA322-R33C2 (Fig.4.4 d), provided by Tecnovapor, a manometer model 213.54-E (Fig.4.4 c) supplied by WIKA with operating range 0 to 1.6 bar, and two solenoid valves model 2W160-15-15 (Fig.4.4 g), supplied by Tecnovapor, were connected to the compressed air system of the LabFlow of CERNN's allowed to impose the pressure required for start-up flow during the tests. The pressure values imposed were controlled through a program developed in LabVIEW (Fig.4.5), which allowed that the set pressure values to be applied with greater precision.

Two manual shut-off valves made of PVC were located in the auxiliary sections of the hydraulic system, one at the inlet and one at the outlet of the test section (Fig.4.3 - Item F). These shut-off valves

(Fig.4.4 e) can operate at a pressure of 2 bar and between a temperature range of 5 ºC to 45 ºC. Depending on the test procedure used, these valves are kept closed or open during restart tests.

LabVIEW software, supplied by National Instruments, was used to monitor and record the pressure and temperature data acquired by the pressure sensor and thermocouples (type J) during start-up flow tests. Figure 4.5 shows the interface created and the main functions that were configured. For example activation and deactivation of the solenoid valves and control of the pressure entering the system.

Figure 4.5 – LabVIEW interface for system monitoring during the start-up test.

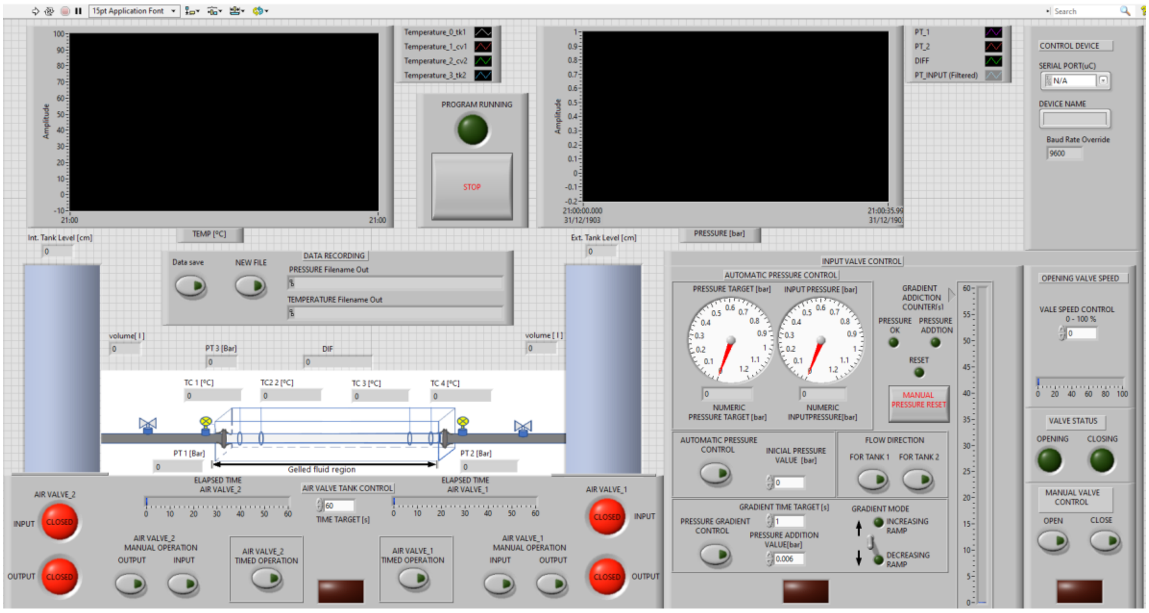

SERIAL PORT(uC) N/A

Baud Rate Override 9600

TIME TARGET [s] 60

PRESSURE ADDITION VALUE[bar] 0.006

Source: Author (2021).

4.3.3 Test section

For the visualization of the start-up flow, the experimental setup will have a test section, which is formed by a square box and the main pipe, previously described. This box is made of acrylic material with mechanical and thermal properties of special interest for the project. The dimensions of the visualization box, will have a length of 1 meter, a height of 0.15 meters and a depth of 0.23 meters. Figure 4.5 shows the test section.

According to Tab. 4.3 the refraction index of the acrylic and the fluids to be used is not equal, but close. This difference in the refraction index can lead to slight distortions of the captured image. To correct the image distortions some features of the *Dynamic Studio* software was used, as exposed further in following section.

4.3.4 PIV Setup

The PIV system is composed of plenty of systems, as it was described in section 2.3. The main parts are:

Figure 4.6 – Top view of the test section with dimensions expressed in millimeters (mm). The test section is made of sheets of the acrylic piece and tube acrylic.

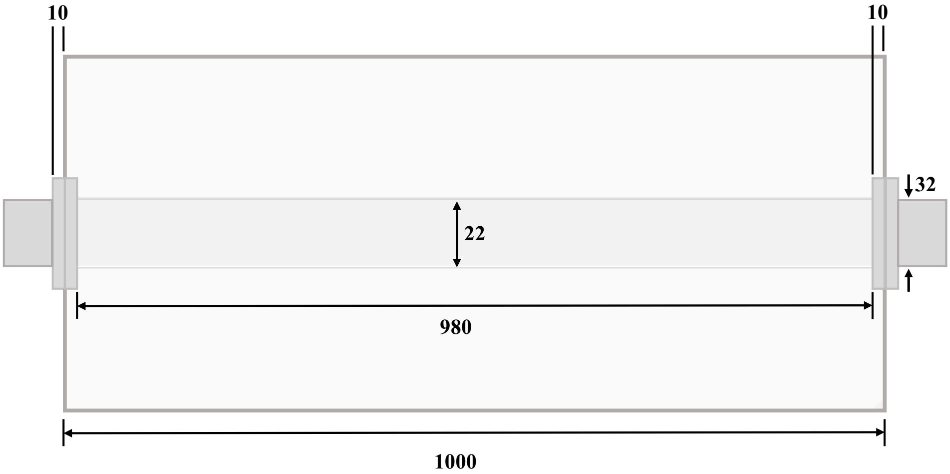

Source: Author (2021).

- Pulsed laser Nd:YAG with *Dual Power 100-500* cavities from *Litron Laser Ltd.* This laser system has a wavelength (λ) of 532 nm (green light), a maximum power of 60 mJ per pulse and a maximum pulse rate of 100 Hz.
- CMOS Nanosense MkIII camera, a maximum resolution of 2352×1728 pixels. Storage capacity of 8136 MB, maximum frequency data acquisition of 100 Hz and a *Micro-Nikkor AF* (*Nikon*) 60 mm objective lens.
- Timer box 9080N0771 from *Dantec Dynamics* to synchronize the laser emission with the camera image acquisition.
- *Dynamic Studio* software for the image capturing and post-processing.

The PIV devices were set in order to guarantee 90º degrees between the laser system and the CMOS camera, this configuration allows the camera to capture images from the plane generated by the laser beam in the flow. Figure 4.7 shows the most suitable configuration assemblage for the present study. In the next subsection, the main parameters for the PIV technique are detailed.

4.3.4.1 Seeding particles

The PIV technique is based on the measurement of the average displacement of particles added to the fluid. For that reason, it is essential a suitable selection of particles to allow a high correlation with the fluid velocity field, i.e., the particle has to follow the flow of the fluid. Therefore, considering that previous studies validated that the use of hollow glass sphere particles (HGS) with a diameter (d_p) of 10 μm are adequate to follow the flow (BLANCO, 2019), particles with this diameter were used to perform the experimental tests. The results obtained show a good correlation indicating that the diameter of the particle chosen was adjusted to the conditions of the flows studied.

Figure 4.7 – Laser and visualization system, the plane of the laser beam and the visualization plane of the camera are set in a perpendicular configuration. Red lines show the positions of planes.

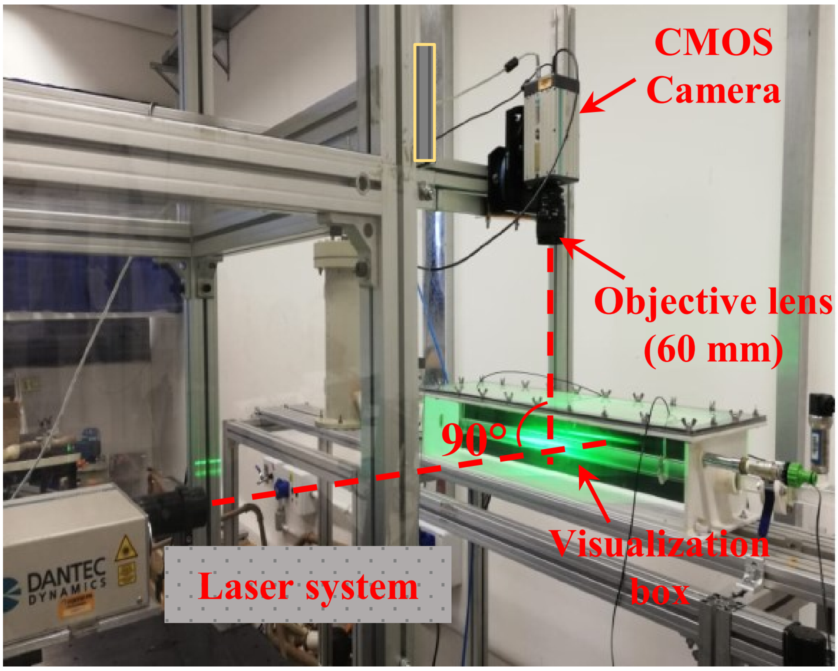

Source: Author (2021).

4.3.4.2 Method for image acquisition

PIV technique records the position over time of small tracer particles introduced into the flow to extract the local fluid velocity. Thus, PIV represents a quantitative extension of the qualitative flow-visualization techniques that have been practiced for several decades. To record the PIV trace particle record, use two methods: (1) methods that capture the images of the illuminated particles at multiple times onto a single frame and (2) methods which provide a single image of the illuminated particle distribution for each time of illumination (RAFFEL et al., 2018). These branches refer to *single frame/multi-exposure* PIV and *multi-frame/single exposure* PIV.

In this project, Dynamic Studio software allowed setting single or multi-frame mode for the PIV system. Due to the characteristic of the phenomenon, the two image recording techniques were used. First, the image recording was performed through double frame/single exposure that is widely used for steady-state phenomena, and then single frame / single exposure was used, which helped us study the phenomenon in the transient regime. This ensured a good correlation and minimized noise error.

4.3.4.3 Image correlation

For the correlation of the images, the Adaptive PIV method was used, which is a method automatic and adaptive for calculating velocity vectors based on particle images. In other words, Adaptive PIV iteratively adjusted the size and shape of the individual interrogation areas (IA) to adapt to local seeding densities and flow gradients.

This correlation method presents some options that allow configuring the adaptive process, such as

Figure 4.8 – Scheme of the recording methods for: a) multiple frame technique: double frames with single exposure, and b) single-frame technique: single exposure. The open circles indicate the particle position in the previous frame.

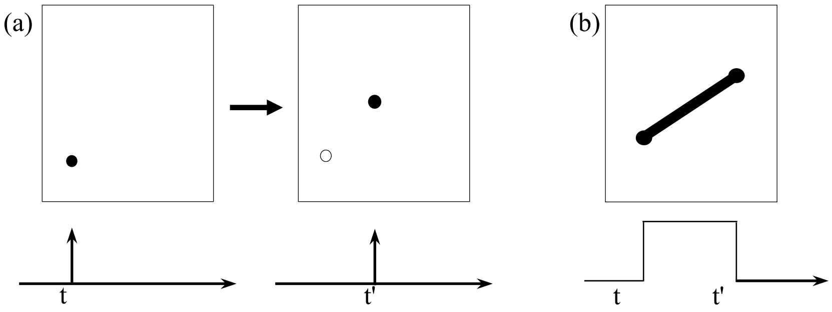

Source: Adapted from Raffel et al. (2018).

the interrogation area that allows establishing the maximum and minimum sizes of the area, as well as the grid step to reach the minimum IA size. To mitigate wall's bias, the filtering option is used, which uses a normally Gaussian function and a signal and noise intensity parameter (k') between 0 and 1, where for high k-values, the bias is low. On the other hand, to prevent outliers from disturbing the iterations and thus the velocity measurements the option validation is used. The validation is done by first applying peak validation on the image cross-correlation and secondly by comparing each vector to its neighbors using the Universal outlier detection algorithm. Finally, the parameters that affect the adaptive adjustment are configured in the adaptability option. In this option, it is possible for example to enable/disable adaptivity of the size of the interrogation area based on particle density. Table 4.4 presents the parameters that were set for the correlation of the images in the present study using adaptative PIV. It should be noted that some of the values were established by default in *Dynamic Studio* software.

Table 4.4 – Main parameters set for the adaptive PIV method. Here S/R- ratio is the root mean square of the negative correlation values and Particle/IA is the number de particles in de interrogation windows.

Fluid	Process	Set parameter
C-50 C-25	IA	Maximum IA size= 64 Minimum IA size=32 Grid step size= 32
	Window/Filter	Window function: Gaussian Filter function: default
	Validation	S/R-ratio=4 Comparison with neighborhood=3x3
	Adaptivity	Particle detection limite=1 Particles/IA=5

Source: Author (2021).

4.3.4.4 Uncertainty analysis

In physical experiments, uncertainty analysis or experimental uncertainty assessment, deals with assessing the uncertainty in a measurement. An experiment designed to determine an effect, demonstrate a law or estimate the numerical value of a physical variable will be affected by errors due to instrumentation, methodology, presence of confounding effects, etc. Experimental uncertainty estimates are needed to assess the confidence in the results (ROCQUIGNY et al., 2008). In this experimental study, uncertainty arises due to the equipment involved and the propagation of error in the quantities derived through the calculations process. The variables measured in this study are pressure, temperature, and velocity.

4.3.5 Uncertainty analysis for measurement devices

4.3.5.1 Type A uncertainty analysis

According to Taylor (1997), type A uncertainty is the “evaluation of a component of measurement uncertainty by a statistical analysis of measured quantity values obtained under defined measurement conditions.”

Essentially, type A uncertainty is data collected from a series of observations and evaluated using statistical methods associated with the analysis of variance. For most cases, the best way to evaluate Type A uncertainty data is by calculating the:

- Arithmetic Mean ($\bar{x}$):The central number of set of numbers that is calculated by adding quantities together and then dividing the total number of quantities. Then, $\bar{x}$ is expressed as:

$$\bar{x} = \sum_{i=1}^{N} \frac{x_i}{N} \tag{4.2}$$

  x_i is each point measured and N is number of measurements.

- Standard Deviation (σ_x): A measure of the dispersion of a set of data from its mean (i.e. average) calculated as:

$$\sigma_x = \sqrt{\frac{\sum_{i=1}^{N}(x_i - \bar{x})^2}{N}} \tag{4.3}$$

- The standard error ($\bar{\sigma_x}$): is the approximate standard deviation of a statistical sample population. The standard error is a statistical term that measures the accuracy with which a sample distribution represents a population by using standard deviation. Normally, is expressed as:

$$\bar{\sigma_x} = \frac{\sigma_x}{\sqrt{N}} \tag{4.4}$$

The type A uncertainty analysis corresponding to the variables measured in this study is described and presented in detail in the Appendix A.2.

4.3.5.2 Type B uncertainty analysis

Any data experimentally obtained through measuring devices and sensors necessarily implies uncertainties related to the precision of each instrument. Therefore, uncertainty analysis is essential to identify potential error sources or even to quantify the precision and validity of the results. For quantities obtained through calculation operations, such as pressure difference Δp, velocity V, temperature T, among others, there will be considered the magnitude and error or each variable involved. Coleman and Steele (2018) indicate that for a magnitude defined by:

$$G = f\left\{x_1, x_1, x_1, ..., x_M\right\} \tag{4.5}$$

where M is the number of independent variables, so, the magnitude G is given by:

$$G = \bar{G} \pm \delta\left(G\right) \tag{4.6}$$

where $\bar{G}$ is the average value defined as $\bar{G} = \left\{\bar{x}_1, \bar{x}_2, \bar{x}_3, ..., \bar{x}_M\right\}$, and $\delta\left(G\right)$ is the uncertainty of G. This uncertainty value is defined by Coleman and Steele (2018) by the following equation:

$$\delta\left(G\right) = \pm\left\{\sum_{i=1}^{M}\left[\left.\left(\frac{\partial G}{\partial x_i}\right)\right|_{x_i=\bar{x}} \delta\left(x_i\right)\right]^2\right\}^{1/2} \tag{4.7}$$

Then. the uncertainty value for the variable is represented by $\delta\left(x_i\right)$ and the coefficient of sensitivity by x_i, and $\partial G/\partial x_i$, which describes how the value of G varies with changes of the variable x_i. The uncertainty value and coefficient of sensitivity can be obtained from the specification data given by the manufacturer of each instrument involved in the measurement process. The type B uncertainty analysis corresponding to the measured variables in this study is presented in Appendix A.3.

4.3.5.3 Uncertainty analysis for PIV technique

Errors in PIV measurements may be introduced at different phases of the measurement chain, e.g. due to the specific flow facility used, setup of the experimental apparatus, image recording process and choices of the data evaluation methods. Sciacchitano (2019) highlights that while all error sources are encoded in the recorded images, some of them remain 'hidden' and their uncertainty cannot be quantified by analyzing the image recordings. Those error sources, typically systematic in nature, include tracer particle response, hardware timing and synchronization, perspective errors, and calibration errors. Instead, the uncertainty associated with error sources such as particle image size and shape, camera noise, seeding density, illumination intensity variation, particle motion, and image interrogation algorithm can be quantified from the image recordings via the uncertainty quantification methods (WESTERWEEL et al., 1996; WESTERWEEL, 2000; RAFFEL et al., 2018).

The two well known and most documented error sources are the out-of-plane motion and particle image diameter (ADRIAN, 1991; WESTERWEEL, 1997). A form of error is related to the high density of seeding that causes a bias displacement or commonly denominated *peak-locking* and leads to a random error of 0.1 pixel. (NOBACH; BODENSCHATZ, 2009). The second form causes a low particle image density and leads to camera read-out noise.

On the other hand, Sciacchitano et al. (2013) report that the error due to the particle image diameter d_τ decreases sharply or increase the particle image diameter in the range between a fraction of one pixel and 2 pixels. For any further increase of d_τ, the error increases approximately linearly. This agrees with known results from Westerweel (1997), who reports that *peak-locking* errors dominate for $d_\tau \leq 1$ pixel and random errors prevail for $d_\tau \gg 1$ pixel. Sciacchitano et al. (2013) also reports that for a discrete displacement technique, i.e., when d_τ is larger than a pixel, a marked difference is observed: the actual error continues decreasing in the observed range, in contrast, Westerweel et al. (2013) report that the RMS error always increases with the d_τ, irrespective of the interrogation method used for the analysis.

As discussed above, measurement errors in PIV depend upon several factors of the flow characteristics, experimental setup and image processing algorithm. Most of these factors vary in space and time, leading to non-uniform errors and uncertainties throughout the flow fields. Several approaches have been proposed for the calculation of PIV uncertainties, and typically classified into indirect methods (BHATTACHARYA SAYANTAN Y CHARONKO,), which make use of pre-calculated information obtained by calibration, and direct methods, which instead extract the measurement uncertainty directly from the image plane using the estimated displacement as prior information. Westerweel et al. (1996), proposes a simple way to quantify the uncertainty of the PIV measurement as a function of a measurement time that can be expressed in a scale integral time. The measurement time is estimated by dividing the total length of the data set in the axial direction (size of the view area in the axial direction multiplied by the number of recorded images) by the average velocity ($\bar{U}$). The integral time scale may be estimated by dividing the pipe diameter by the average velocity ($D/\bar{U}$). So, the sampling error for the flow statistic is inversely proportional to the square root of the corresponding measurement time. The following equations show the different expressions for these parameters,

- Measurement time:

$$M_t = \frac{X_D N_T}{\bar{U}} \tag{4.8}$$

where N_T is the total of images captured, X_D is the length of the view size in the axial direction.

- Integral time scale:

$$I_t = \frac{D}{\bar{U}} \tag{4.9}$$

- Sampling error:

$$e_s = \frac{1}{\sqrt{\frac{M_t}{I_t}}} \tag{4.10}$$

It is noteworthy that for the phenomenon studied in this project, the number of images is reduced, less than 800, this value affects the results of equation 4.10, as can be seen in the calculations of the uncertainties presented in Appendix A.4 for each flow conditions analyzed.

4.4 Experimental procedures

This section emphasizes on the two types of measurements performed in the present experimental study: the first is the pressure measurement required for the start-up flow and the second is the mean velocity vector field and its derived quantities acquired using PIV technique, for example, axial velocities and patterns for deformation.

4.4.1 Experimental procedure to perform rheological tests

To analyze the rheological behavior of the viscoplastic fluids used in this study, rheometric tests of steady flow curve and creep flow were performed. The procedure to perform each test is described below and the results obtained are presented in the section 5.2.

4.4.1.1 Steady flow curves tests

To perform the flow curve tests, the HR-3 rotational rheometer (TA Instruments) was used. The rheological tests were carried out at a temperature of 22 ºC, in order to represent the same conditions defined in the laboratory. To obtain the data of shear stress by shear rate, the implemented procedure consisted in the application of decreasing shear rate ramps, from 100 and 170 to 0.02 s^{-1} for the fluid C-25 and C-50 respectively, which was chosen since the material responds quickly to imposed stresses, minimizing the time between tests. Two different geometries were used to carry out the tests: cross-hatched parallel plates (CH-PP) and smooth parallel plates (S-PP). For the fluid C-25, the tests were carried out only for a smooth plate, diameter D=40 mm and gap d=1 mm because the yield stress is low and the results obtained for CH-PP were not consistent (not shown). For the fluid C-50 in order to avoid the wall slip at low shear rates, between 0.02 and 5 s^{-1} CH-PP with D=40 mm and d=1 mm were used, for shear rates between 5 and 170 s^{-1}, were used S-PP (FERNANDES et al., 2019).

The results with parallel plate geometries require correction of the measured stresses, due to the shear rate varies with the radius of the plate (MACOSKO; LARSON, 1994).

$$\tau_{cor} = \tau_{rheo}\left(3 + \frac{\mathbf{dln}\tau_{rheo}}{\mathbf{dln}\dot{\gamma}_{rheo}}\right) \tag{4.11}$$

where τ_{cor} is the corrected shear stress, τ_{rheo} and $\dot{\gamma}_{rheo}$ are the shear stress and shear rate obtained from the rheometer. For used fluids, dlnτ_{rheo} was fitted as a second degree polynomial for the two fluids.

4.4.1.2 Creep flow tests

This section presents the procedure for the creep tests, which were performed in order to determine the behavior of the fluid before start-up flow. The creep test consists of applying constant homogeneous shear stress and then measuring the resulting shear rate variation in time. When the shear rate drop monotonically approaching zero, the applied shear stress is considered to be below the yield stress, then when another stress is applied and the shear rate tends to a steady-state value, then the applied shear stress is greater than yield stress (BARNES, 1999; ABEDI et al., 2019).

The rheological tests were performed at a temperature of 22 ºC and using a rotational HR-3 rheometer (TA Instruments). Two geometries were used to evaluate the effects of slip on the applied shear stress: S-PP and CH-PP with diameter D = 40 mm and gap d = 1mm. The measurements were carried out according to the following protocol: initially, the fluids were left at rest for a time of 120 seconds (s), at the end of rest time shear stress is applied to the material for the time of 600 s, determined as enough time to verify the material flow. After the imposition time, the fluid was again left at rest for another 120 s. The same procedure was repeated for various values of shear stress. It is necessary to mention that the value of the yield stress obtained by creep tests depends on the duration of applied shear stress, which was set as 600 s in the present investigation. In this case, if the shear stress of value 20 Pa (CH-PP) had remained imposed for a time of 1200 s, the curve would tend to a non-zero shear rate. The impossibility of determining an independent value of the test is well known because, for longer durations, such as days, for example, unstable flows only occur for lower stresses, characterized by very low shear rates that continue to decrease (COUSSOT et al., 2002; CATON; BARAVIAN, 2008; MØLLER et al., 2009; MENDES; THOMPSON, 2013). Then, a moderate time was determined that will facilitate the duration of the rheological tests and that could also be used in the tests with the experimental setup.

4.4.2 Pressure measurement to analyze transient start-up flow

Before the transient start-up flow tests, pre-tests for pressure stabilization, and tests to obtain steady flow curves for each sample fluid were performed. The purpose of tests steady flow curves was the rheological characterization of the fluids and to validate the effectiveness of the experimental setup.

4.4.2.1 Pre-test

The first step in the procedure to perform the pre-tests is the homogenization of the fluids, the sample (5 liters) was agitated at 150 rpm for 30 minutes to avoid the generation of air bubbles and then transferred to the internal reservoir tank. About glycerine, this process was not necessary.

Table 4.5 – Summary of the pre-test for each material

Fluid	Δp [Pa]	t $_{shear}$ [s]	t$_{rest}$ [s]
C-25	2×10^3	60	600
C-50	10×10^3	60	600

Source: Author (2021).

After the homogenization procedure, the LabFlow temperature was set at 22°C, in order to reproduce the same conditions for the tests. With uniform temperature conditions, pre-tests were performed to standardize the initial pressure distribution for all tests with the same fluid and to provide better results. First, the fluid found in the internal reservoir is displaced to the external reservoir until the two reach the same level of fluid, which allows completely fill the test section. This step is possible by opening the two shut-off valves (SOV1 and SOV2) located in the auxiliary sections and connecting the reservoir tanks with the test section, as shown in Fig. 4.9. The pressure relief valve (PRV2) located on the upper part of the external reservoir is opened to the atmosphere to facilitate fluid movement. The pre-test consists of applying a certain pressure value set by the pressure regulating valve (PRV) for a time, followed by a rest time, as shown in Table 4.5. During the rest time, the PRV1 and PRV2 valves are opened to the

Figure 4.9 – Schematic illustration of fluid flow in the tests of steady flow curves and transient start-up flow by ramps of driving pressure.

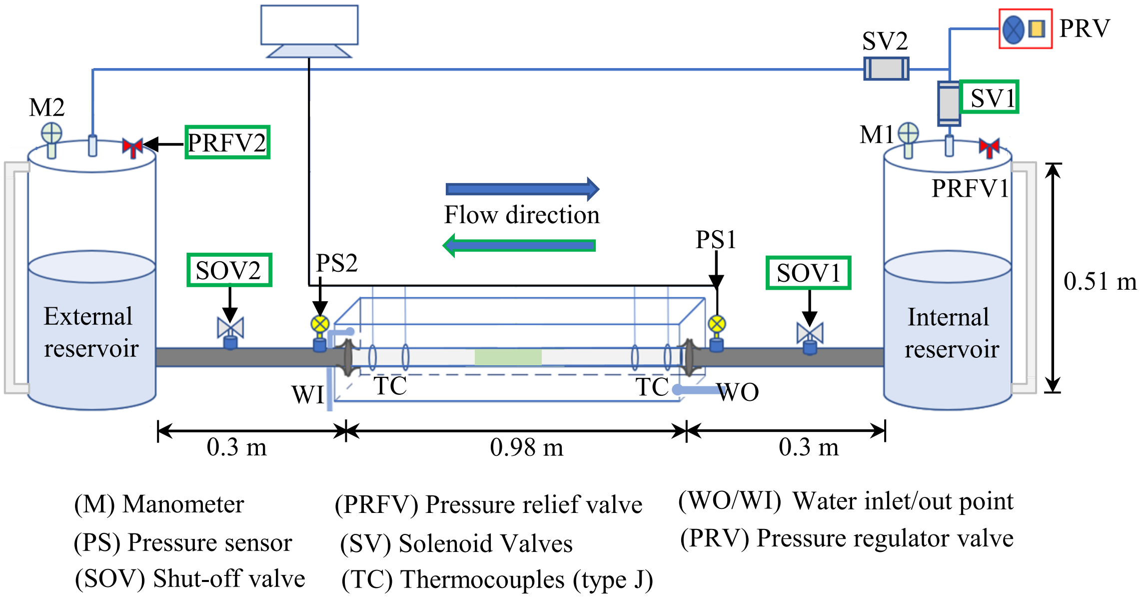

Source: Author (2021).

atmosphere to relieve the system's pressure. A pressure stabilization criterion was determined based on variation of the measurement of the pressure sensors (PS1 and PS2), in which it was considered that if the pressure varied less than 0.5% in 30 seconds, the pressures reached the permanent regime (PEREIRA et al., 2019).

An advantage of the experimental setup is that it allows the pre-tests to be performed in both directions, in other words, the fluid can be displaced from the internal reservoir to the external reservoir, and in the opposite direction. This operating advantage is possible due to the solenoid valves (SV) located after the pressure regulating valve (PRV).

4.4.2.2 Experimental procedure to obtain steady flow curve

In order to verify if the experimental setup could represent the phenomenon of study, steady flow curves were obtained, which were compared with the steady flow curves obtained in the rheometric tests. The experimental procedure to obtain the steady flow curves of each material in the experimental setup was performed, establishing some conditions of temperature and pressure. Regarding temperature, the tests were carried out at 22 ºC for the two fluids. Regarding pressure, constant values were applied for a period 600 seconds (t=600s), and the pressures measured by pressure sensors located at the inlet and outlet of the test section were recorded, using only the pressure drop values after the set time. The pressures values used for the fluids C-25 and C-50 are presented in Tab. 4.6.

According to the pressure measurements and volumetric flow rate during the circulation of the fluids through the test section was obtained the equivalent shear rate and shear stress, this data was allowed to obtain the steady flow curves of the experimental setup.

Based on the balance of forces given by Eq. (2.18) and written here for convenience, the wall shear stress was obtained as:

$$\tau_w = \left(\frac{-\Delta p}{L}\right)\left(\frac{R}{2}\right) \tag{4.12}$$

Δp is the pressure drop, L is the length between the two pressure sensors and R is the radius of the test section.

By differentiation of the Eq. (2.26) the relationship between the volumetric flow rate and the apparent shear rate at the wall is given by Eq. (4.13), but due to that experimental setup does not have a volumetric flow rate measurement system, it was first necessary to calculate it using the integration of the average velocity field obtained by the PIV technique on the cross-section of the tube (LIU; BRUYN, 2018), Eq. (2.20).

$$\dot{\gamma}_{aw} = \frac{4Q}{\pi D} \tag{4.13}$$

Q is the volumetric flow rate and D is the diameter of the test section.

However, it is possible to calculate an approximate conversion for the corrected shear rate at the wall using the Weissenberg-Rabinowitsch equation, considering incompressible, laminar, permanent, isothermal flow hypothesis, without slip on the walls and with velocity only in the axial direction of the pipe (MACOSKO; LARSON, 1994), as:

$$\dot{\gamma}_{corr} = \frac{\dot{\gamma}_{aw}}{4}\left(3 + \frac{\mathrm{dln}Q}{\mathrm{dln}\tau_w}\right) \tag{4.14}$$

where $\dot{\gamma}_{aw}$ and τ_w are the apparent shear rate and the shear stress in the pipe wall, respectively, Q is the volumetric flow rate measured in m^3/s. The term dln$Q$/dlnτ_w is the inclination of ln$Q$ as a function of lnτ_w, for each point. For Newtonian fluid, the inclination is 1. For non-Newtonian fluids the function can be expressed by ln$Q$ = a (ln$\tau_w)^2 + b$ ln$\tau_w + c$, where a , b and c are constants that can be adjusted for each case.

To avoid overpressure in the system that affects the measurements, during the experimental test to obtain Δp_{1-2}, the valves PRFV and SV remain closed or open according to the direction of displacement of fluid between the reservoir tanks. An example of operation is shown in Fig. 4.9, considering the direction of flow from the internal reservoir to external, locked inside in a green box, the valves SV1 and PRFV2 are open, the other valves are closed, allowing flow in that direction. The tests were performed, starting from the lower value to the highest value. The procedure performed to obtain steady flow curves can be summarized in the following steps:

1. Set the required pressure.
2. Starting the recording of pressure measurements 10 seconds (s) before imposing pressure.
3. Pressure regulator valve opens.
4. Start image recording when the pressure value remains slightly constant and varies less than 2.5% for 15 seconds. The parameters for visualization of images are shown in subsection 4.4.3.

Table 4.6 – Pressure drop values and corresponding wall shear stresses for fluids C-25 and C-50.

Fluid	Pressure drop [Pa]	Wall shear stress [Pa]
C-25	1281.3	6.15
	854.50	4.10
	423.45	2.03
	314.27	1.50
	213.45	1.02
	154.14	0.80
	131.25	0.62
	93.03	0.43
C-50	10460.72	50.25
	8347.61	40.10
	6190.91	29.74
	5214.40	25.05
	2933.06	14.09
	1647.49	7.91
	942.69	4.53
	728.16	3.50
	472.06	2.27

Source: Author (2021).

5. Finish recording of data.
6. Finally, close the pressure regulator valve.

The constant flow curve tests were obtained from the experimental configuration for fluids C-25 and C-50 and were compared with the rheometric tests, validating the performance of the experimental setup. The results are presented in section 5.2.1.

4.4.2.3 Experimental procedure to analyze the transient starting flow under constant pressure application

The start-up flow is a process that involves the temporal evolution of the flow fields when an external force is applied. In order to evaluate this transient response for C-25 and C-50 viscoplastic fluids as a function of pressure drop (wall shear stress), experimental tests were performed under the temperature conditions of 22 ºC following the protocol described below:

1. Set the required pressure.
2. Start recording of pressure measurements and recording of flow images using the PIV technique 10 s before imposing pressure up to t equal to the set value of wall shear stress. The parameters for visualization images are shown in subsection 4.4.3.
3. The pressure regulating valve opens
4. At t=300 s, record images using the PIV technique
5. At t=600 s, record images using the PIV technique

6. Finish recording of data, after t=600s.
7. Finally, close the pressure regulator valve.

As observed in the steps described, the measurement of the temporal evolution of the flow fields from the beginning of the pressure imposition (t=0) to the set value, at a value of $t = 300s$ and beyond at t=600s.

Figure 4.10 – Dimensionless time scale established to analyze the flow reset of fluids C-25 and C-50. The dimensionless time t' [-] was obtained from t_c[s]/t[s].

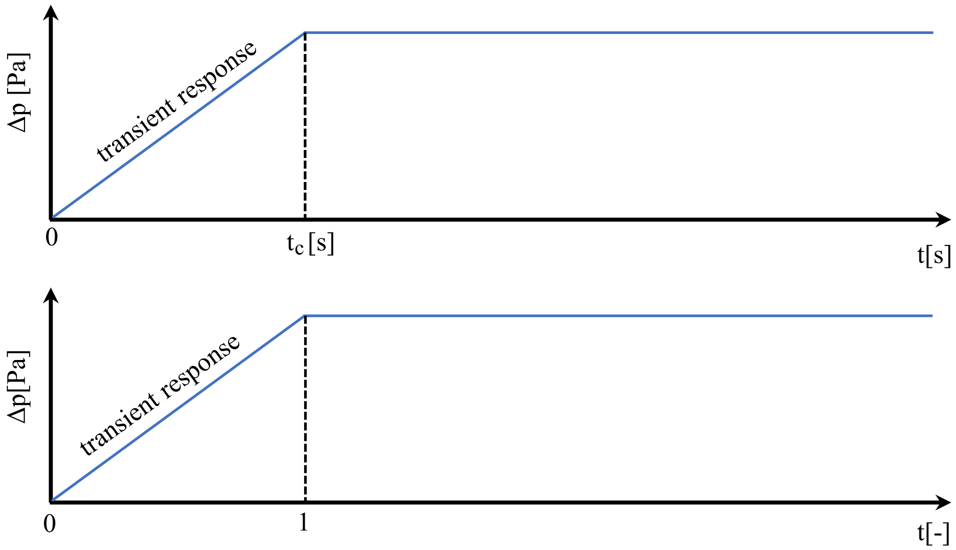

Source: Author (2021).

However, due to limitations in the experimental setup, the times for which the wall shear stresses reached the set values were different, and dimensionless time scale was established that allowed to compare the temporal evolution of the fluids at the same time. This dimensionless scale consisted of dividing the dimensional time scale (t) by the value of time until reaching the set wall shear stress, which was denominated critical time (t_c), in this way a dimensionless time scale ($t\,'$) from zero to one ($0 - 1$) was obtained, which allowed comparing the transient process of the fluids. This dimensionless time scale is described by Eq. 4.15 and Fig. 4.10 shows a diagram of how the pressure was imposed and the dimensionless time scale established.

$$t' = \frac{t_c[s]}{t[s]} \tag{4.15}$$

4.4.3 Velocity vector field measurements and flow patterns obtained by PIV technique

To obtain the mean velocity vector field, it was first necessary to acquire images showing the displacement of the seeded particles in the fluid. This image recording process was performed using the experimental setup shown in section 4.3. To visualize the seeded particles the synchronization between the laser and the camera was set by the *Dynamic Studio* software, ensuring that the laser beam occurs simultaneously as the camera shutter is opened. Furthermore, the acquisition frequency and the time between pulses were established according to the average velocity required at the entrance of the test section, which for the present study depended on the applied pressure ramps. The light laser beam reached the central plane of the pipe, located inside the visualization box, as shown in Fig. 4.7. Then, the displacement of the seeding particles at two different times were correlated by image post-processing.

Table 4.7 – Visualization parameters set

Type of test	Fluid	Reynolds number [-]	Pressure drop [Pa]	Time between pulse [μs]	Frequency [Hz]
Validation PIV methodology	Glycerine	1; 2; 4	1977.9; 4683.7; 7430,9	1950; 1641; 1357	70; 100; 100
Start-up flow	C-25	5.51; 1.20; 4.44×10^{-2}; 7.84×10^{-3}; 8.67×10^{-4}; 2.68×10^{-4}; 7.98×10^{-5}; 1.27×10^{-6}	1189.7; 840; 420; 310; 210; 150; 130; 90	1960	2; 3; 5; 40; 65
	C-50	2.78; 7.01×10^{-2}; 8.01×10^{-2} 2.04×10^{-2}; 2.58×10^{-3}; 1.06×10^{-3}; 2.0×10^{-4}; 9.27×10^{-5}; 2.22×10^{-5}	10460.72; 8347.61; 6190.91; 5214.40; 2933.06; 1647.49; 942.69; 728.16; 472.06	20; 40; 80	1960; 1970

Source: Author (2021).

Subsequently, through *Dynamic Studio* software, the image post-processing was performed, following the process described in subsection 4.3.4. Considering that during the visualization process some problems such as the refractive index of the materials and the curvature of the pipe even with the precautions taken for the execution of the tests could affect the quality of the images, it was necessary to perform a calibration process through the *Dewarping* function, which also allowed to establishing masks and define limits to evaluate the specific area of the acquired image.

Taking into account that the flow velocities correspond to low values of pressure drop, after the calibration process, the visualization area was established at $125mm \times 22mm$ and the final interrogation area was $32pixels \times 32pixels$ with an overlap of 50%. The result is a vector field of $0.0425 \times 0.0425mm^2/px^2$. The resulting mesh of the PIV data is 63×79 points (radial / axial).

In order to evaluate the PIV methodology, initial tests with Newtonian fluid were performed. For initial validation with Newtonian fluid in the experimental setup, the frequency were set at 70 and 100 Hz; Doorne and Westerweel (2007) recommended using of a frequency equal to or greater than 15 Hz. The time between pulses was established considering the displacement of the seed particles in an interrogation area and the integral time scale as the upper limit of the time between pulses. Table 4.7 shows a summary of the parameters set for the tested fluids.

Then, the correlation between the dependence of the average flow velocity on the pressure drop, and the dependence of the slip velocity on the shear stress was obtained from the image acquisition processing, as well as an analysis of the behavior of fluid in the different regimes of the yielding process solid-liquid. One parameter that was possible to obtain was the volumetric flow rate of each fluid calculated by integrating the velocity field measured on the cross-section of the pipe when the flow had reached a steady-state.

Finally, Fig. 4.11 summarizes the image acquisition and processing process as a series of 9 consecutive and fundamental steps that must be performed to obtain the mean velocity vector field and to be able to analyze the dynamics of flow.

Figure 4.11 – Process for image acquisition and post-processing steps with *Dynamic Studio* software.

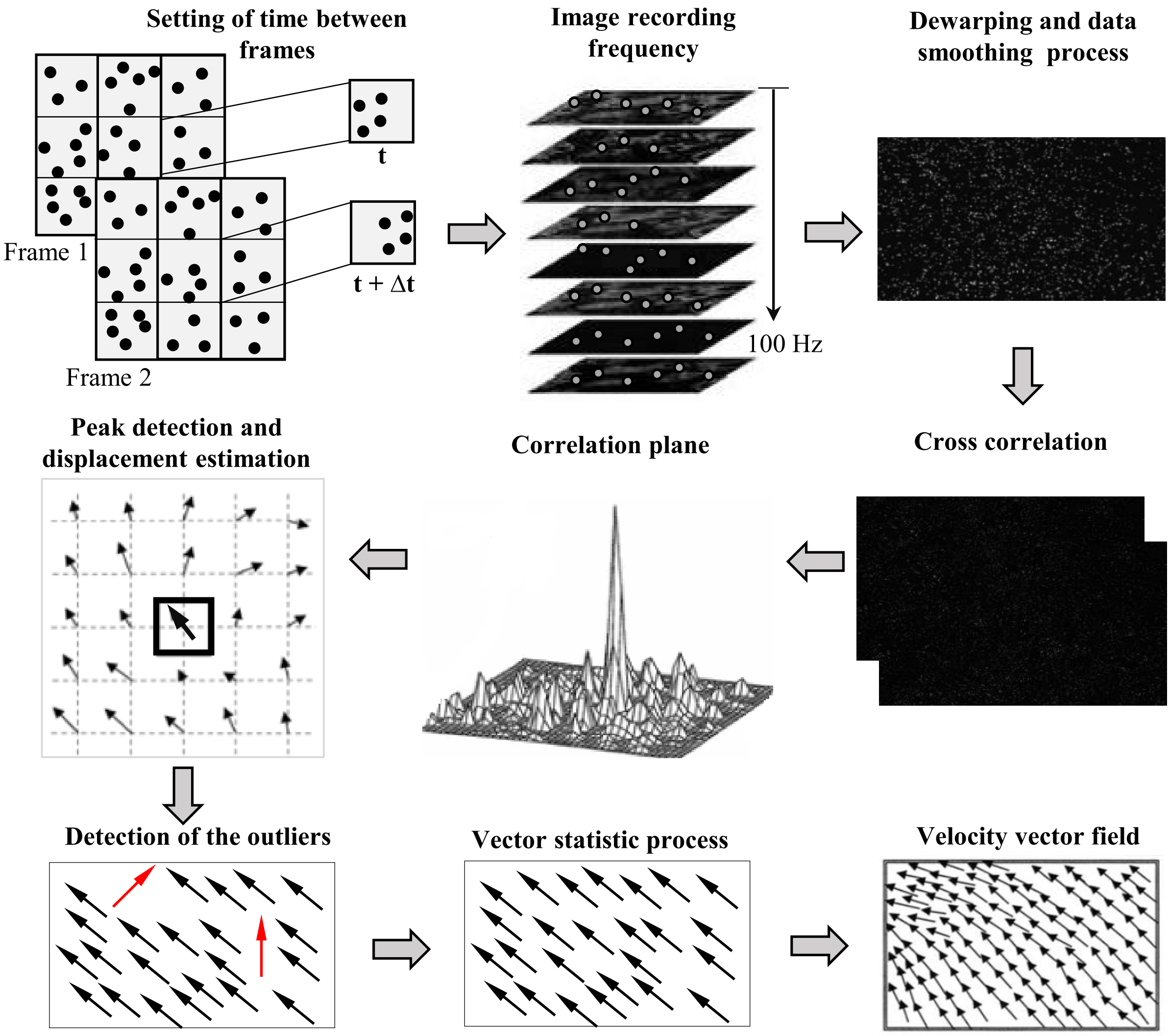

Source: Author (2021).

4.4.4 Validation of PIV measurements

In the evaluation of PIV methodology, the transient regime analytical solution for velocity and for Newtonian fluid (WATSON, 1995) will be used given by the Fourier-Bessel solution and expressed as:

$$u_z(r,t) = \frac{R^2 \Delta p}{4\mu L}\left[1 - \left(\frac{r}{R}\right)^2\right] - \sum_{n=0}^{\infty} C_n J_0(\lambda_n r) e^{\lambda_n t} \tag{4.16}$$

where C_n is expressed as:

$$C_n = \frac{8R^2}{\lambda_n^3 J_1(\lambda_n)} \tag{4.17}$$

Here Δp is a pressure differential, (R) is the radius of the pipe, (μ) is the dynamic viscosity, (L) test section length, (r) radius ratio, (J_0) and (J_1) are Fourier-Bessel function, (λ_n) eigenvalues and (t) is the time.

The Newtonian fluid chosen is pure glycerine with properties detailed in Table 4.1. The velocity profiles will be developed to evaluate the velocity in the test section taking into account the time to reach the permanent regime. Then, velocity profiles analytically calculated will be compared with the velocity profiles obtained through the PIV technique for the same time and pressure values. If the results between the solutions have a good agreement, it could be possible to say that the parameters (time between pulse and frequency) set in the PIV can represent the study phenomenon. The pressure drop values and the PIV parameters for the validation of the methodology are presented in Tab. 4.7.

4.5 Chapter Summary

Chapter 4, according to previous works, allowed to determine the viscoplastic fluids that were used in the tests, namely aqueous ultrasound gel solutions (25 and 50 wt%). The experimental setup was presented, and its main parts were described in detail. Finally, the types of tests that were performed were exposed and the protocols that had to be followed. The validation protocol of the PIV methodology with glycerine as Newtonian fluid was also described.

5 RESULTS

This chapter presents the results of the visualization of start-up flow of two viscoplastic ultrasound gel solutions by imposing different pressure drop through a smooth horizontal pipe.

The first section presents the results of the PIV methodology using glycerine. Section 5.2 presents the rheological results of the different viscoplastic fluid concentrations used. The steady flow curves obtained from the experimental setup are compared with the rheometric data. Finally, the flow kinematics using the PIV technique, the analysis of wall slip behavior as a function of the wall shear stress, and the calculation of wall shear stress through the velocity profiles are exposed and discussed in section 5.3.

In this chapter, the concept of absolute percentage error (APE) (see Appendix A.1) will be used to verify how close the experimental data are to the theoretical data. The equation used is:

$$APE\% = \left| \frac{x_{theo} - x_{exper}}{x_{theo}} \right| \tag{5.1}$$

where x_{theo} is the value theoretical and x_{exper} is the value measured on the experimental setup.

5.1 Validation PIV methodology

Before the measurements were taken, it was necessary to quantify the accuracy of transient velocity profiles obtained with the PIV. The experimental setup presented in Fig. 4.9 was used and glycerine as Newtonian fluid. Under a constant pressure drop (Δp), the verification could be achieved by comparing the velocity profiles captured by PIV measurements at different times with the analytical solution for unidirectional velocity in the transient flow regime for a Newtonian fluid given by Eq. (4.16), (BATCHELOR, 2000):

Fig. 5.1 shows the quantitative comparison between normalized velocity profiles obtained by visualizing the flow with the analytical solution given by Eq. (4.16) for the pressure values shown in Table 5.1. Initially, a good agreement is observed between the results of experimental and analytical velocity distributions at different times and steady-state. For the pressure values analyzed, the maximum absolute percentage error between the data was 6.88% when t' = 1.2, for a pressure drop ΔP = 1977.9 Pa and a Reynolds R_e = 1 (Table 5.1).

The error bars showed in the experimental velocity profiles indicate the standard deviation of velocity measured for three positions at each set time and considering the error of the visualization technique. The definition of uncertainty given by Coleman and Steele (2018), section 4.3.4.4 was used to perform the uncertainty analysis. However, since the accuracy of the measurements depends on the sensitivity of the measurement system PIV with respect to the movement of the particle, the error present in the evaluation of the PIV recordings is the bias of the displacement of the particle, commonly known as a *peak-locking* effect (WESTERWEEL, 1997). This error occurs when the particle image size is small for the pixel size and is leads to measurement errors up to 0.1 pixels (WESTERWEEL, 1997; SCARANO; RIETHMULLER, 2000). For times between pulses set, 0.1 pixels is translated to an uncertainty velocity

Figure 5.1 – Comparison between the evolution of the dimensionless velocity profiles u/U_{max} experimental (solid symbols) and analytical solution Eq. (4.17) (solid line) and Δp (a) 1977.9 Pa (R_e = 1), (b) 4683.7 Pa (R_e = 2) and (c) 7430.9 Pa (R_e = 4) for different dimensionless times.The error bars are defined by the root mean square deviation of the velocity profiles and the error of the PIV technique. In Figure S.S represent steady-state

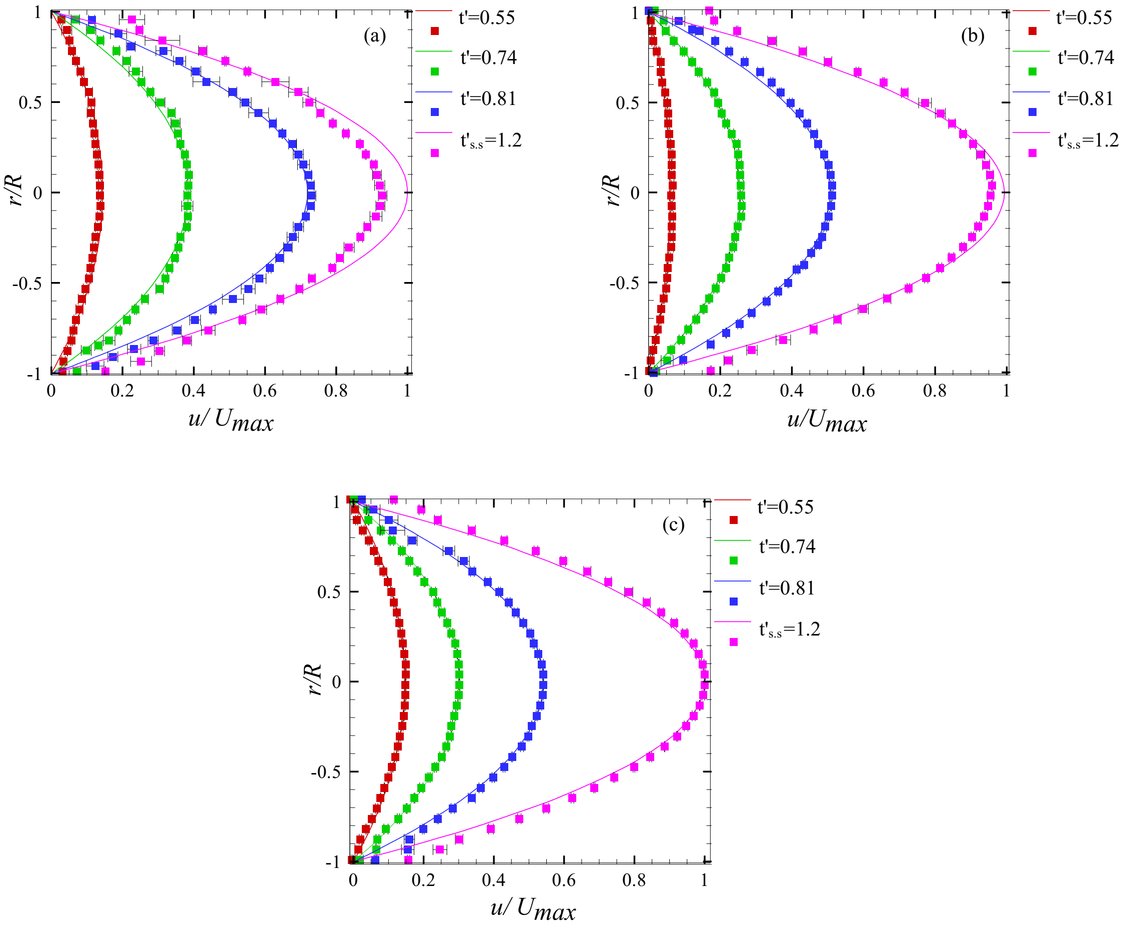

Source: Author (2021).

(δu) at a t'= 1.2 equal to 1.97×10^{-4}, 1.65×10^{-4}, and 1.99×10^{-4} for the flow conditions of Fig. 5.1a, 5.1b, and 5.1c, respectively. The results of the absolute percentage error and the uncertainty of the velocity for the other dimensionless times are also shown in Table 5.1.

For the discrepancy between experimental and analytical data at $r/R = \pm\ 1$, it may be related to the slip behavior caused by various factors as high shear rates, increasing viscosity of the liquid, and the curvature of the solid boundary (NETO et al., 2005). Also, this is caused by the low values of velocity measured in this region and the limitation of the PIV system to interpolates in the sub-pixel scale where high deviation of the velocity values can be found (NOGUEIRA et al., 2005; SCHRIJER; SCARANO, 2008). However, despite the refinement limitations of PIV technique, the results obtained showed that the accuracy of the velocity profiles in transient regime measurements is acceptable.

Table 5.1 – Uncertainty values of δu and APE for different Δp and dimensionless times.

ΔP [Pa]	R_e	Time between pulses [s]	δu [m/s]	Dimensionless time [t']	U_{max} [m/s]	δu [%]	APE [%]
1977.9	1	0.1365	1.97×10^{-4}	0.55	8.28×10^{-3}	2.39	4.74
				0.74	2.34×10^{-2}	0.84	5.63
				0.81	4.45×10^{-2}	0.44	3.54
				1.2	6.09×10^{-2}	0.32	6.88
4683.7	2	0.1651	1.65×10^{-4}	0.55	9.65×10^{-3}	1.71	8.52
				0.74	3.70×10^{-2}	0.45	3.68
				0.81	7.35×10^{-2}	0.22	12.93
				1.2	1.43×10^{-1}	0.11	4.10
7430.9	4	0.1357	1.99×10^{-4}	0.55	3.18×10^{-2}	0.63	2.27
				0.74	6.43×10^{-2}	0.31	4.33
				0.81	1.15×10^{-1}	0.17	3.17
				1.2	2.13×10^{-1}	0.09	2.31

Source: Author (2021).

5.2 Rheological measurements

5.2.1 Steady flow curve

The analysis begins with the steady flow curves of the materials. The results obtained in the experimental unit were compared with the data from the HR-3 rotational rheometer (TA Instruments). To obtain the steady flow curve of the Fig. 5.2a of fluid C-25, seven shear rates were used, calculated using the procedure described in section 4.4.2.2. It is observed that the curves have similar trends, however the difference of the shear stresses in the range of measured shear rates is practically constant and the absolute percentage error between the adjustments was 60.6%, which is considered high. The error bars shown in the graphs represent the uncertainty of the calculated stress values (Appendix A.3.1). The rheological data were obtained from single rheometric measurements, considered within ± 0.5% of the standard deviation according to the instruments calibration certificate, guaranteeing the results' reliability.

Figure 5.2b shows the steady flow curve for the fluid C-50, ten points were used to obtain the curve for the experimental setup. It is observed that for shear rates between 0.8 and 55 s^{-1}, the trend of the data is similar to the curve of fluid C-25, but for shear rates lower than 0.8 s^{-1}, the results differ strongly and the model HB does not fit well to the stress values corresponding to these shear rates, the percentage deviation from a known standard reaches a maximum between the fits greater than 70%. In order to have a better understanding of the role of wall slip in the flow of yield stress fluids, the steady flow curve was plotted using the S-PP geometry for the fluid C-50. The first relevant point is related to the good agreement between the data obtained from the experimental setup and the rheometric data with S-PP, which is proof that the fluid sliding pipe's wall. The second relevant point is that the yield stress measured with wall slip is about four times less than that measured without slip (data not shown here). Finally, it is observed that for shear rates greater than 0.8 s^{-1}, the results of the measurements performed with and without wall slip overlap, but only within a completely viscous regime. The point where the shear rates intersect is called the critical shear rate ($\dot{\gamma}_c$), and it coincides with the shear rate values found by Salmon et al. (2003) and Poumaere et al. (2014) for concentrated emulsion and Carbopol® solutions in rheometric flows. Then, based on the evidence that there is wall slip in the results obtained from the experimental setup and looking

Figure 5.2 – Steady flow curves for the fluid: C-25 (a) and C-50 (b), obtained by performing rheometric measurements and tests in the experimental setup and adjusted by the Herschel-Bulkley model (HB). The error bars are defined by the uncertainty of the calculation of the wall shear stress.

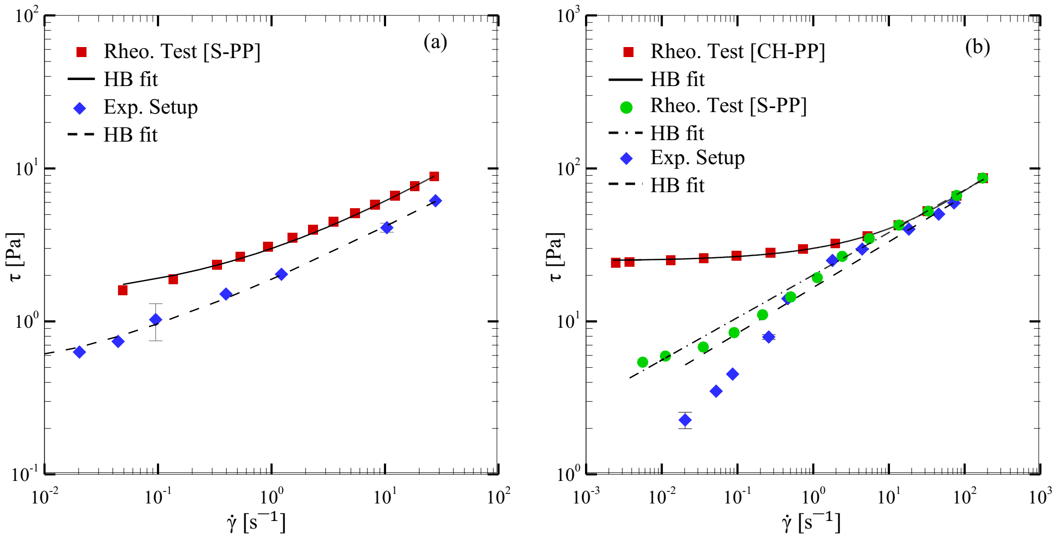

Source: Author (2021).

to obtain a better correlation with the data from rheometric measurements, the correction presented by Weissenberg-Rabinowitsch (WRC) (MACOSKO; LARSON, 1994), and described in section 4.4.2.2 by Eq. (4.14), was used to correct and obtain new values of the shear rate and plot a new steady flow curve.

Figure 5.3 – Steady flow curves for the fluid: C-25 (a) using S-PP and C-50 (b), performed with CH-PP para lower shear rate and S-PP for high shear rates. The experimental setup data for the two fluids were corrected for wall slip by WRC. The error bars are defined by the uncertainty of the calculation of the wall shear stress.

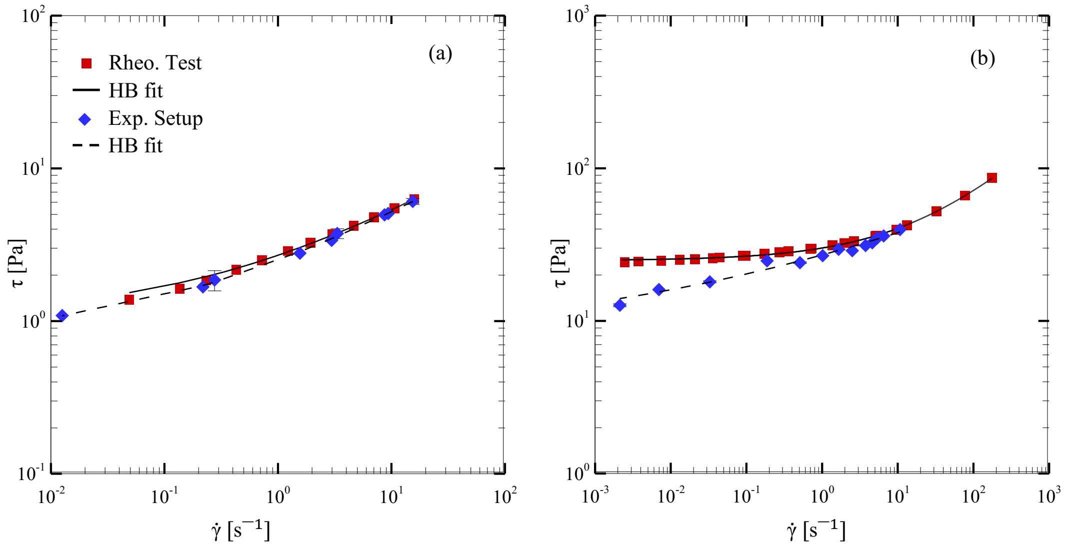

Source: Author (2021).

The corrected steady flow curves obtained from the experimental setup are presented in Fig. 5.3. A good agreement is observed between the new values of shear rate and shear stress with the rheometric results for the two fluids, and in particular for the fluid C-50 when compared to the curves of Fig. 5.2. New adjustments were made by HB model and new rheological parameters were obtained. Table 5.2 summarizes the calculated data and presents the percentage difference between the obtained values. However, it is observed that although the values were corrected, the percentage difference from the known standard value is still high for the fluid C-50 therefore, the hypothesis arose that the wall slip in the pipe of the experimental setup, would be reasonably higher for high concentrations of the ultrasound gel, although it is necessary to perform more tests with concentrations greater than 50 wt% to confirm this hypothesis.

Table 5.2 – Summary of the rheological parameters obtained by the HB fit of the steady flow curves of the two fluids used.

Fluid	Method of measurement	Yield stress (τ_0)[Pa]	Consistency index (k) [Pa.s^n]	Power law index (n) [-]	APE (τ_0) [%]	APE (k) [%]	APE (n) [%]
C-25	Rheometer	1.32	0.81	0.57	–	–	–
	Experimental setup	0.52	1.53	0.39	60.60	88.8	31.6
	Experimental setup (corrected)	1.22	0.98	0.53	7.57	21	7.01
C-50	Rheometer	24.85	5.19	0.45	–	–	–
	Experimental setup	8.66	18.39	0.20	>50	>50	55.5
	Experimental setup (corrected)	21.35	3.85	0.43	14.10	25.8	4.44

Source: Author (2021).

From the abrupt changes in the values of the rheological parameters presented in Tab. 5.2, it is observed that the wall slip complicates the determination of the yield stress for flows of viscoplastic materials in pipes with smooth walls. This is to be expected, due to several studies such as those performed by Yilmazer and Kalyon (1989), Kalyon et al. (1993) have shown that the slip phenomenon affects flows induced by drag (steady torsional) and by pressure (capillary), and the experimental setup used in the present study operates under similar principles to capillary flows. On the other hand, an interesting result of the steady flow curves is that the wall slip presents an increase when the shear stress required to overcome the yield stress of the material is greater, as in the case of fluid C-50. In the following sections, this relationship between the wall slip behavior with the shear stress will be analyzed.

5.2.2 Creep flow tests

In the previous subsection, the steady flow curve tests obtained by rheometric measurements and experimental setup were presented. The rheological parameters, namely yield stress, consistency index, and power-law index of each fluid, were calculated by extrapolating the results using the Herschel-Bulkley model fit for fluids having viscoplastic behavior. This section presents the results for the creep tests, which were performed in order to determine the behavior of the fluid before start-up flow.

Figure 5.4 – Creep flow tests using two types of geometries and applying different values of shear stress for fluids: C-25 a) S-PP, b) CH-PP, and C-50 c) S-PP, d) CH-PP . The symbols marking the highlighted regions denote the deformation regimes and are explained in the text: (S), solid; (S + F), solid-fluid coexistence; (F), fluid.

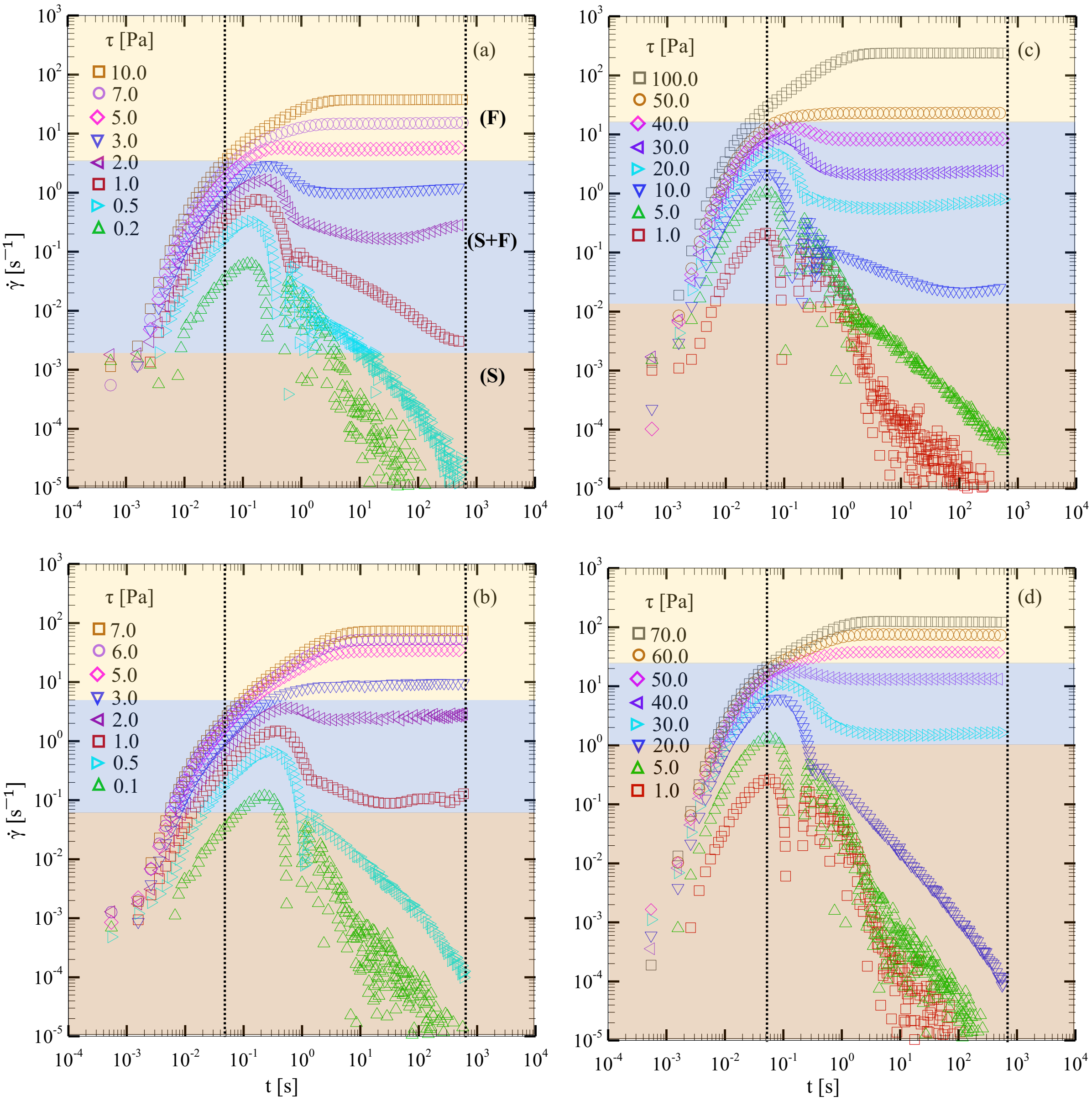

Source: Author (2021).

Figure 5.4 presents the results of the creep flow tests for the two fluids used. It is observed that the value of shear stress for which the shear rate tends to a non-zero value varies with the geometry used. The results obtained for the fluid C-25 with S-PP (Fig. 5.4a) show that when the shear stress equal to 2 Pa, the shear rate tends to a constant value, although for the stress equal to 1 Pa, the shear rate does not tend monotonically to zero and can also be considered as a start-up flow shear stress value, which coincides with the results obtained for CH-PP (Fig. 5.4b). The fluid C-50 has a different behavior than the fluid C-25, the value of shear stress for which the shear rate tends to a constant value is 10 Pa for tests with S-PP geometries (Fig. 5.4c), while for the CH-PP geometry is 30 Pa (Fig. 5.4d), which is twice as large. Based on the results of Fig. 5.4, were adopted the yield stress values τ_0 = 1 Pa for the fluid C-25 and τ_0 = 30 Pa for the fluid C-50. Using these yield stress values obtained from the creep tests and the HB fit, the rheological parameters, consistency index, and power-law, were calculated. For C-25, k = 0.63, n = 0.71, and for C-50, k = 2.62, n = 0.53. For the case of fluid C-25, the values are still close to those calculated in the previous subsection, while for the fluid C-50, the difference is notable mainly for the consistency index of the material. The subsequent calculations in this investigation that require the rheological parameters of the materials will be performed with the yield stress of the creep tests.

From Fig. 5.4, three different deformation regimes were identified, consistent with previous investigations (BENMOUFFOK-BENBELKACEM et al., 2010; PÉREZ-GONZÁLEZ et al., 2012; POUMAERE et al., 2014; YOUNES et al., 2020a). These regimes were determined considering the final behavior of the fluid for each value of applied shear stress between 0 seconds and 600 seconds. The dashed lines in Fig. 5.4 delimit the analyzed time period. As described in subsection 4.4.1.2, for shear stress values lower than the yield stress, the variation of the shear rate tends to zero, this corresponds to a solid behavior of the material [region (S) in Fig. 5.4]. When the shear stresses are greater than the yield stress, determined as τ_0 = 1 Pa and τ_0 = 30 Pa, for fluids C-25 and C-50 respectively, the shear rate increases monotonically for a constant value, indicating that the material a fully yielded [region (F) in Fig. 5.4].

It is observed that for values of shear stress that slightly exceed the yield stress, the shear rate reaches a peak and then decreases, remaining at a moderately constant value. This behavior is shown for the two fluids and is consequent with a regime of coexistence of regimes [region (S + F) in Fig. 5.4], in which the fluid does not behave as a solid-like, nor as a fluid, indicating that the start-up flow is not direct, but is a transition process between the solid and fluid phases. Recently, studies performed in a pipe flow with Carbopol solutions have also observed a similar yielding transition (AGARWAL; JOSHI, 2019; YOUNES et al., 2020b). It is also possible to say that from the results with S-PP geometries, that the main effect of wall slip is to shift the solid-fluid coexistence regime to lower values of applied shear stress, this is more evident for the fluid C-50 (Fig. 5.4c and d). Finally, and according to Poumaere et al. (2014), wall slip is an inevitable phenomenon in the flow of yield stress fluids, and to reach a complete state of deformation is difficult in the presence of this phenomenon. In the following sections, an attempt was performed to scale the rheological results obtained with pipes flows in the presence of wall slip, and from here on we use the term yielding transition as a reference to the start-up flow process.

5.3 Visualization of viscoplastic flow yielded in pipe with wall slip

In this subsection, the results obtained using the PIV technique are presented for the flow of pipes with wall slip. That is the flow vector field and the derived quantities as velocity profile, scalar map velocity, and deformation maps obtained in the meridional plane of the test section. The values obtained are non-dimensionalized by the mean velocity, shear rate corrected for wall slip, and the diameter at the entrance of the visualization section. The data obtained will be used to compare to what extent the findings on the yielding transition of rheometric flows can be extrapolated to industrially relevant settings.

5.3.1 Vector flow field measurements and derived quantities

To characterize the yielding transition in the flow of a pipeline, not only the temporal flow field was measured during the evolution to a determined value of wall shear stress (τ_w), but it was also measured after the period of imposition of *t′*=15, as described in subsection 4.4.2.3. This procedure closely mimics the controlled shear stress imposition used to characterize the yielding transition in the rheometric flow of the performed creep tests.

The analysis begins showing the dimensionless mean statistic velocity vector field in steady state for the fluid C-50 (Fig. 5.5a), it is observed that within the framework of laminar flow, the behavior of the material is consistent with the plug-like flow of yield stress fluids. The standard deviation of the velocity is shown in Fig. 5.5b, the deviation values are relatively low, and do not exceed 10% of the mean velocity. From Fig. 5.5a, it may also be seen that the flow is practically invariable in the axial direction, which is expected because the radial component of the velocity was at least 3 orders of magnitude smaller than the axial. Therefore, the velocity field is given by Eq.(5.2). As the velocity values are non-dimensionalized by $\bar{U}$, it is possible to analyze the dimensionless velocity in steady-state with studies found in the literature. When *Z/D* = -1.5, $u/\bar{U}$ ratio is equal to 2 at the centerline. This value is the same presented by Blanco (2019), where the dimensionless velocity value is 2 for laminar regimes using an ultrasound gel solution 30 wt%. Moisés et al. (2018), shows that for the steady-state flow of a Carbopol® solution 0.08% the value of $u/\bar{U}$= 1.5, which differs from the value found in the present study, but is very close to the value of $u/\bar{U}$= 1.4 for laminar flows presented by Peixinho et al. (2005). An explanation for the differences between the values of $u/\bar{U}$ ratio, is related to the rheological parameters, especially with the yield stress of the material. Then, it is possible to conclude that for high yield stress, the plug core size is larger and $u/\bar{U}$ ratio is lower.

$$u(r,z) = \frac{1}{N}\sum_{i=1}^{N} u_i(r,z) \tag{5.2}$$

where N is the number of instantaneous vector field measured, and r and z are the radial and axial coordinates, respectively.

In order to observe the destructuring of the material when the fluid reaches the steady-state, Fig. 5.5c shows the dimensionless deformation map. The maximum values of deformation are very close to the walls of the pipe, and minimum amounts of material are visible in the central plane of the pipe, possibly indicating that the process of breaking the material begins between the limits of the fluid and the solid surface, extending toward the central plane of the pipe as the shear rate increases in that region. Fluid C-25 presented similar results (not shown here). A broader view of the breaking process will be presented below. The results presented in Fig. 5.5 were obtained for a wall shear stress (τ_w) equal to 50.25 Pa, it was calculated using Eq. (4.12), described in subsection 4.4.2.2, and repeated here for convenience. The quantities derived from the PIV measurements were calculated using 700 pairs of images after a non-dimensional time t'= 15, which is large enough to allow studying the limit case of steady state. The parameters set for the flow visualization are found in the procedure described in subsection 4.4.3.

Figure 5.5 – a) Dimensionless mean statistic velocity vector field for the fluid C-50, and measured for τ_w= 50.25 Pa. b) Standard deviation of mean statistic velocity, and c) dimensionless deformation map. Results presented for the arithmetic mean over 600 instantaneous fields measured after to reach the steady state at t'= 15.

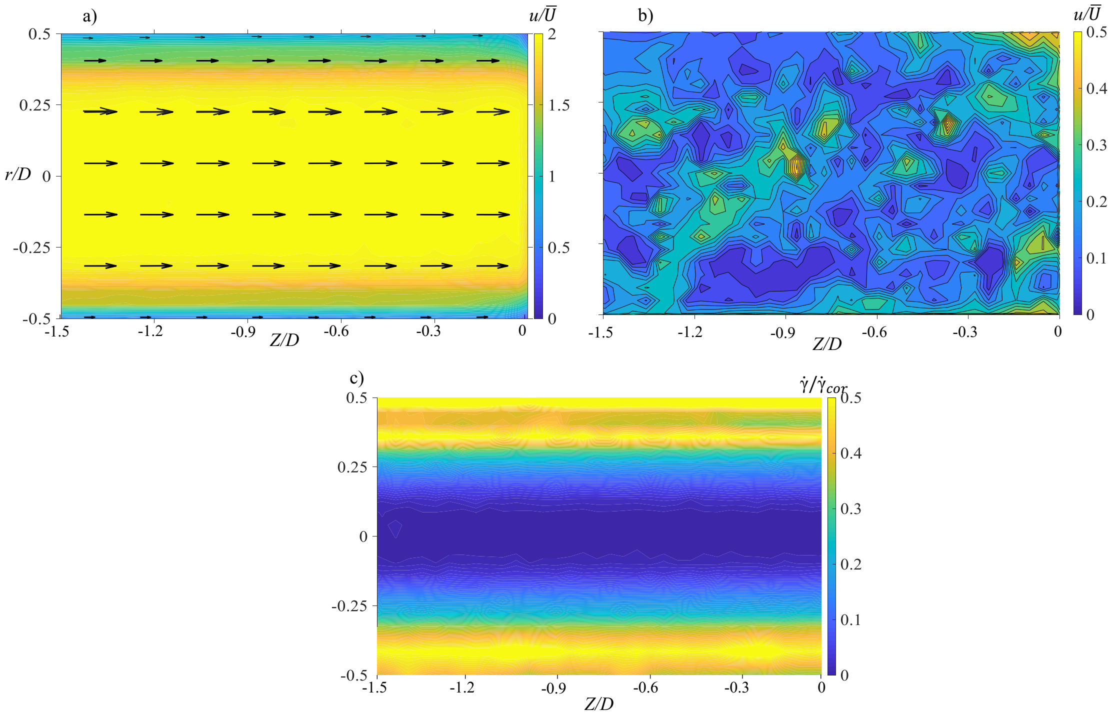

Source: Author (2021).

5.3.1.1 Temporal evolution of the velocity and deformation fields

The focus is on the temporal evolution of the velocity, and deformation fields are analyzed for a better understanding of the yielding transition of the viscoplastic fluids used in the present study. The results obtained for each fluid were obtained by applying eight values of wall shear stress. However, for practicality, the temporal analysis is shown for three values of τ_w for the two fluids, chosen as critical for two reasons: 1) they are values close to the yield stress calculated by creep tests, and 2) fluid displacement was visualized during the increase of wall shear stress to a set value.

Figure. 5.6 shows the behavior of velocity field for the C-25 fluid. The results were obtained following the procedure described in subsection 4.4.3, and plotted for six dimensionless times. Table 5.3 presents all the parameters set to obtain the velocity fields of the fluids C-25 and C-50. Figure. 5.6a to 5.6f shows the evolution of velocity field for τ_w= 0.43 Pa. It is observed that the values of $u/\bar{U}$ ratio fluctuate between one dimensionless time and other, this is more notable for Fig. 5.6b and Fig. 5.6d, where the dimensionless velocity reaches a value of 1.2×10^{-3} and 2×10^{-3} (color bar) respectively, but immediately this value decreases as shown in Fig. 5.6c and Fig. 5.6e. This behavior is similar for the velocity fields shown for Fig. 5.6g to 5.6l, measured when τ_w= 1.02 Pa is applied. The $u/\bar{U}$ values shift between 0 and 1.5×10^{-3}, which is moderately less than τ_w= 0.43 Pa.

Figure. 5.6m to 5.6r, present the results obtained for τ_w= 1.5 Pa, apparently the behavior of the velocity field shown with the two previous values of τ_w, is only noticeable in the early dimensionless

Table 5.3 – Visualization parameters set

Flow properties	Fluid	C-25 / C-50
	Yield stress [Pa]	1 / 30
	Wall shear stress [Pa] Fluid C-25	0.43;0.62;0.80;1.02;1.5;2.03;4.10;6.15
	Reynold number [-] Fluid C-25	5.51; 1.20; 4.44×10^{-2}; 7.84×10^{-3}; 8.67×10^{-4}; 2.68×10^{-4}; 7.98×10^{-5};1.27×10^{-6}
	Wall shear stress [Pa] Fluid C-50	4.3; 7.92; 14.10; 25.05; 29.74; 40.1; 50.25
	Reynold number [-] Fluid C-50	2.78; 7.01×10^{-2}; 8.01×10^{-2} 2.04×10^{-2}; 2.58×10^{-3}; 1.06×10^{-3}; 2.0×10^{-4}; 9.27×10^{-5}; 2.22×10^{-5}
Laser settings	Type	Double-Nd:YG
	Wavelength [nm]	532
	Energy [mJ]	70
	Laser beam thick [mm]	1
Camera settings	Resolution [Pixels]	2352 × 1728
	Trigger rate [Hz] Fluid C-25	2; 3; 5; 40; 65
	Trigger rate [Hz] Fluid C-50	20 ; 40; 80
Image	Visualization area [mm ×mm]	125 × 22
	Time between pulses [μs] Fluid C-25	1960
	Time between pulses [μs] Fluid C-50	1960; 1970
	Number images	1040
PIV analysis	Type of correlation	Central difference
	Interrogation area	32 ×32
	Overlap [%]	50
	Vector per image	3942

Source: Author (2021).

times, this leads to the conclusion that the fluctuations are originated for low values or close to the yield stress τ_0. However for wall shear stresses greater than τ_0, this behavior decreases or practically disappears. Due to the limitations of the PIV technique for transient phenomena, it is not possible to quantify the value of the fluctuation of the velocity field for each dimensionless time. However, these breakthroughs are consistent with the reported by Putz and Burghelea (2009), Poumaere et al. (2014) and Liu and Bruyn (2018), when performing tests in experimental and rheometric settings, respectively.

Figure. 5.7 shows the evolution of the velocity fields for the fluid C-50. It is observed that for τ_w= 14.10 Pa (Fig. 5.7a-f) the values of $u/\bar{U}$ show a fluctuation pattern similar to that observed for the fluid C-25 when τ_w is less than τ_0. A notable difference in the behavior of the flow fields is observed in Fig. 5.7g to Fig. 5.7k for τ_w= 25.05 Pa, which is close to the value of τ_0 of the material and that contrasts with the behavior observed for the fluid C-25 when a τ_w value close to τ_0 was applied. The fluctuations of the $u/\bar{U}$

Figure 5.6 – Velocity fields for the fluid C-25, measured as a function of time for: a)-f) τ_w=0.43 Pa; g)-l) τ_w=1.02 Pa, and m)-r) for τ_w=1.5 Pa. The values of velocity and time are dimensionless.

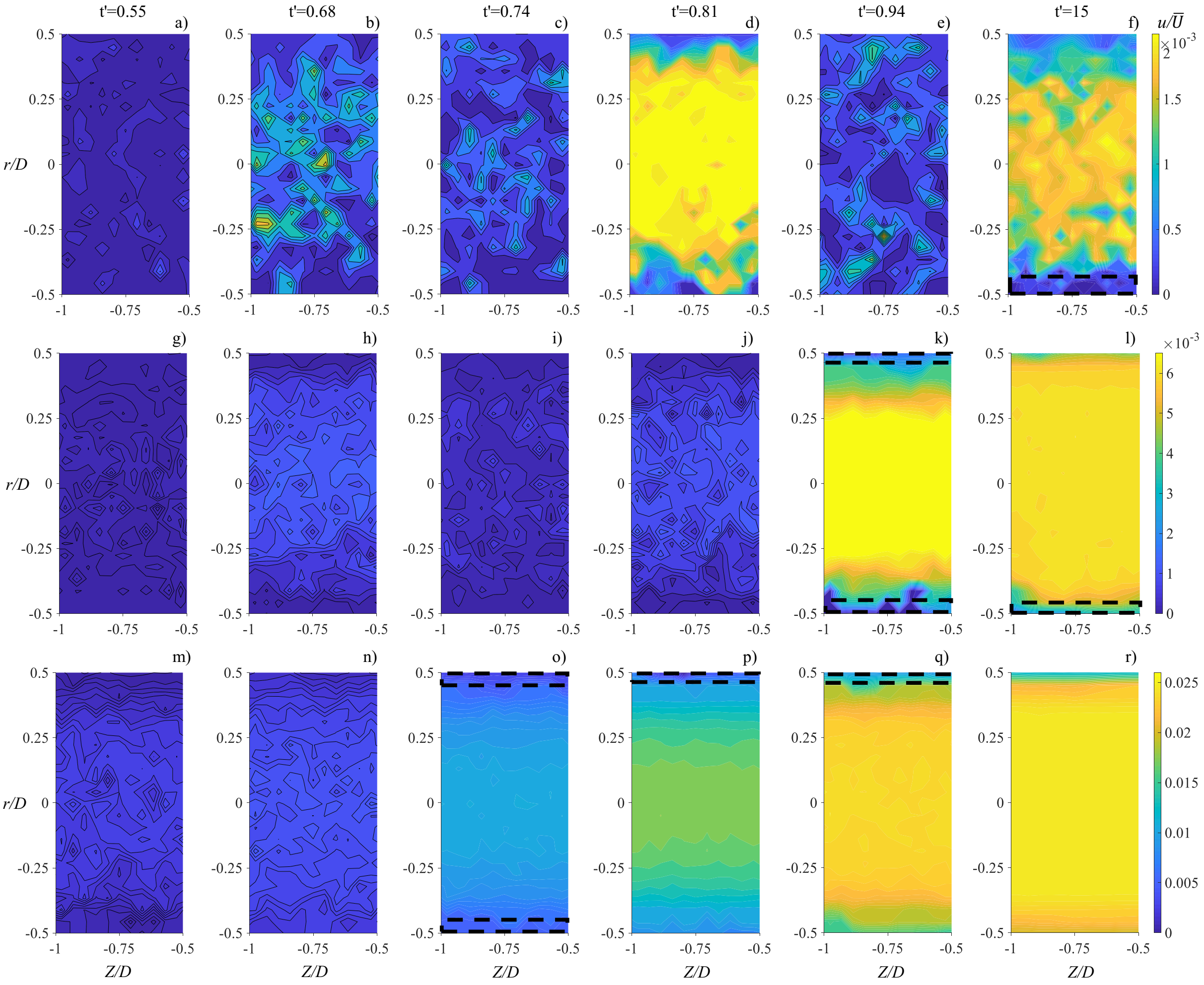

Source: Author (2021).

ratio were constant for all dimensionless times measured. The nature of this behavior may be related to a process of destructuring and restructuring of material. Also, elastic effects can also play an essential role in the velocity field fluctuations. For the creep tests performed, it is observed that for shear stress values located in the region (S + F), the shear rate values show increases and decreases, then tend to a slightly oscillating value, indicating that a destructuring process is taking place. Finally, and in accordance with the results for the fluid C-25, Fig. 5.7m-r shows the velocity fields for τ_w= 40.10 Pa, which is greater than the τ_0 of the material, the flow pattern is stable and does not present fluctuations of the $u/\bar{U}$ ratio. However, for the values of τ_w= 14.1 Pa and τ_w= 25.05 Pa, the $u/\bar{U}$ ratio varied between 1.7×10^{-2} and 7×10^{-2}, respectively, which are an order of magnitude greater than the registered for the fluid C-25. It is also important to note that for the wall shear stresses and for the maximum dimensionless time analyzed, it was only possible to reach the stable state for τ_w= 40.10 Pa (fluid C-50), for the other wall shear stresses a greater dimensionless time is necessary.

An important data that was visualized in the velocity fields for the two fluids, was the presence of static zones or with very low velocity (box of dashed line) when the ratio $r/R = \pm0.5$. The following statement

Figure 5.7 – Velocity fields for the fluid C-50, measured as a function of time for: a)-f) τ_w=14.10 Pa; g)-l) τ_w=25.05 Pa, and m)-r) for τ_w=40.10 Pa. The values of velocity and time are dimensionless.

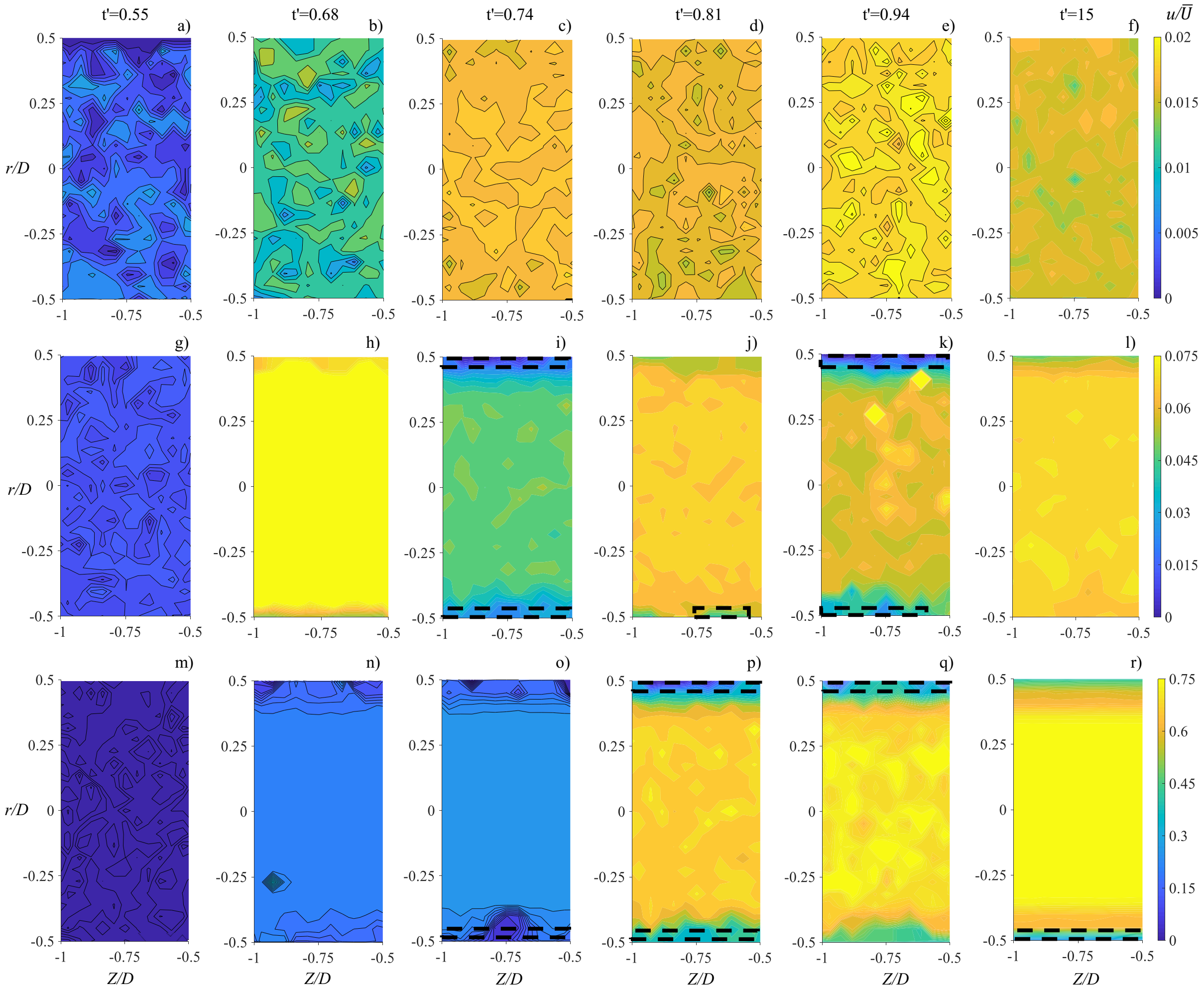

Source: Author (2021).

cannot be assured, because it is beyond the scope of the resolution of the PIV technique used, but could be slip zones and according to Bingham (1922) this could be the slip layer and "slip comes from a lack of adhesion between the material and the shearing surface. The result is that there is a layer of liquid between the shearing surface and the main body of the suspension". Taghavi et al. (2012), also observed this type of areas in the study of viscoplastic fluid displacements using the UDV technique, although in greater dimension and accuracy. Some problems caused by slip were discussed in the rheological results, but it was not possible to verify these sliding areas, the results obtained by the PIV technique allow "visualize" the existence of areas over which the fluid can slide. The graphs of the velocity profiles presented in the next section will allow us to understand a broader vision of what is observed in the velocity fields.

From the plotted temporal velocity fields, a vision of the behavior of the fluid was obtained when the wall shear stress increases. Now the temporal evolution of the dimensionless deformation fields for the fluids is analyzed. From Fig. 5.5, the assumption had been established that the destructuring of fluid began between the limits of the fluid and the solid surface, Fig. 5.8 and Fig. 5.9 confirm that for the wall shear stresses and times analyzed, the breakdown of the material begins near the wall. However, this breakdown

Figure 5.8 – Deformation fields for the fluid C-25, measured as a function of time for: a)-f) τ_w=0.43 Pa; g)-l) τ_w=1.02 Pa, and m)-r) for τ_w=1.5 Pa. The values of deformation and time are dimensionless.

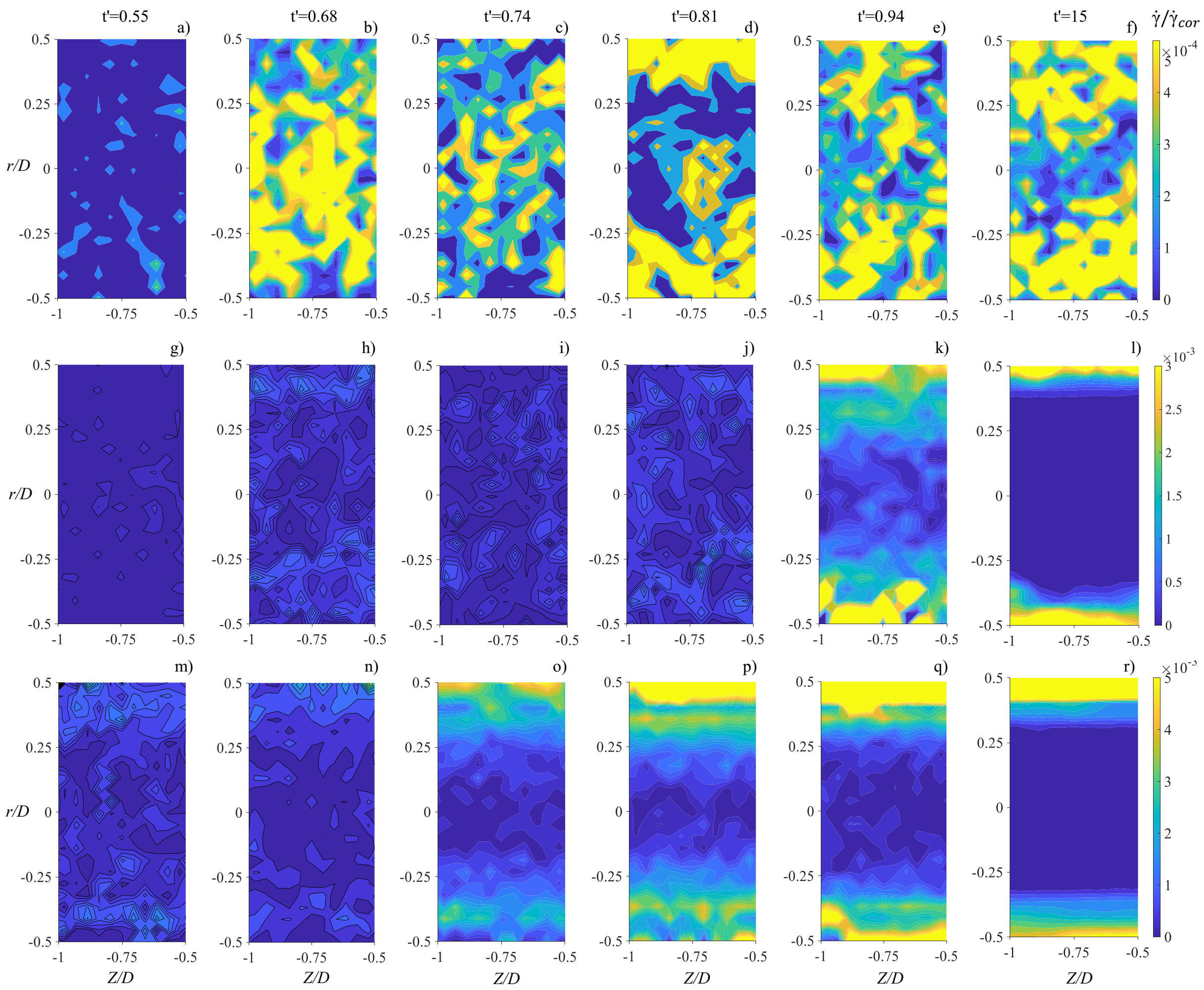

Source: Author (2021).

process also presents the same behavior observed in the velocity fields, that is, fluctuations for lower shear rate values and stability for shear rates higher than the critical shear rate ($\dot{\gamma}>\dot{\gamma}_c$) as shown in the rheological tests. Figure. 5.8a to Fig. 5.8f, and Fig. 5.9a to Fig. 5.9f present the results for the fluid C-25 and C-50 when τ_w = 0.43 Pa and τ_w = 14.1 Pa, it is shown that for the times analyzed, the fluid did not break the structure and only in Fig. 5.8d, it is possible to observe a higher of ratio $\dot{\gamma}/\dot{\gamma}_{corr}$= 4.50$\times$10^{-4}, which is located closest to the wall of the pipe. While for the fluid C-50 the $\dot{\gamma}/\dot{\gamma}_{corr}$ values are moderately high at early times (Fig. 5.9a and Fig. 5.9b) and remain oscillating between a value of $\dot{\gamma}/\dot{\gamma}_{corr}$= 2.2$\times$10^{-3}.

The deformation pattern for τ_w = 1.02 Pa and τ_w = 25.05 Pa, corresponding to fluids C-25 and C-50, also show differences. Initially, the fluid C-25 fluctuates between values $\dot{\gamma}/\dot{\gamma}_{corr}$= 0.5$\times$10^{-3} and $\dot{\gamma}/\dot{\gamma}_{corr}$= 1$\times$10^{-3} (Fig. 5.8g to Fig. 5.8j), but at t'= 0.94 the shear rate increases sharply to 2.5$\times$10^{-3} (Fig. 5.8k), this behavior could be caused by the avalanche effect, (see (COUSSOT et al., 2002)), Fig. 5.8*l*, justifies this assumption, although, for t'= 15 the stable state has not yet been reached, it will eventually be reached. In contrast to the previous behavior, the fluid C-50, from early time presents increases in $\dot{\gamma}/\dot{\gamma}_{corr}$ near the wall and destructuring of the material (Fig. 5.9h to Fig. 5.9*l*), which is not constant but indicates

Figure 5.9 – Deformation fields for the fluid C-50, measured as a function of time for: a)-f) τ_w=14.10 Pa; g)-l) τ_w=25.05 Pa, and m)-r) for τ_w=40.10 Pa. The values of deformation and time are dimensionless.

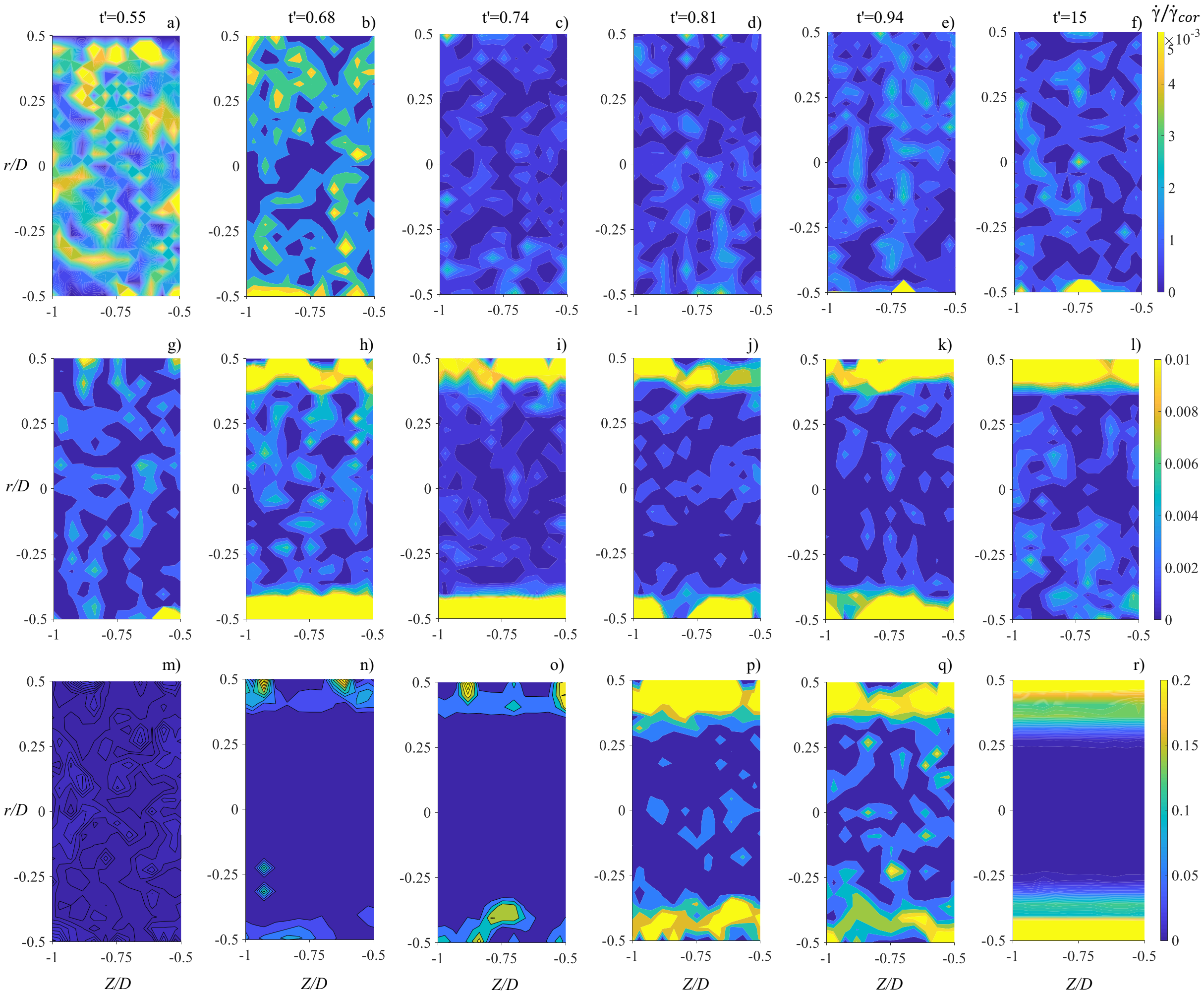

Source: Author (2021).

coexistence solid and fluid regions, as shown in rheological tests [region (S+F) in Fig. 5.4]. Finally, Fig. 5.8m to Fig. 5.8r and Fig. 5.9m to Fig. 5.9r show the evolution of the dimensionless deformation rate for the two fluids when τ_w> τ_0. It is important to highlight the very close flow pattern observed, initially the fluid shows a behavior as a solid (Fig. 5.8m and Fig. 5.9m), and in sequence, the destructuring of the fluid begins at the interface between the pipe wall and the material at the same time that $\dot{\gamma}/\dot{\gamma}_{corr}$ ratio increases close to of the wall, as observed in Figures Fig. 5.8n to Fig. 5.8q and Fig. 5.9n and Fig. 5.9q, for fluid C-25 and C-50 respectively. After, the fluid presents destruction with $\dot{\gamma}/\dot{\gamma}_{corr}$= 0 in the center of the pipe and $\dot{\gamma}/\dot{\gamma}_{corr}$ maximum in the pipe wall, indicating that the material flows entirely through the test section.

From the results obtained, it can be concluded mainly that the yielding transition is not a direct process but is mediated by deformation regimes. It is observed that for low-stress values, the material deformation rates are slightly constant and appear to increase with the applied wall stress value (PUTZ; BURGHELEA, 2009). Furthermore, the presence of static zones near the pipe wall in the velocity fields indicates that the flow of viscoplastic fluids can be affected by the slip phenomenon.

5.3.1.2 Temporal evolution of the flow regimes in presence of wall slip

To better appreciate the variations in the velocity fields, this section shows the evolution of the velocity profiles for several wall shear stresses described in Table 5.3. For the sake of simplicity, the results are presented only for three dimensionless times, t'=0.74, t'=0.94, and t'=15. The first is related to the wall shear stresses below the yield stress [region (S) in Fig. 5.4]. Figure 5.10a and Fig. 5.10d show that the velocity profiles for the fluid C-25 at t'=0.74 and t'=0.94 are irregular and fluctuate for values of the ratio $u/\bar{U}$=0 and $u/\bar{U}$= 2.5×10^{-3}, reaching negative values in some cases, as observed for the velocity profile (blue symbols). This negative value is related to flow reversal and is caused by the elastic-recoil effect of the material. Similar behavior is observed for the fluid C-50, although the fluctuation values of the ratio $u/\bar{U}$=0 are an order of magnitude greater and the reversal of flow is more evident (Fig. 5.11a and Fig. 5.11d). It is important to mention that during the rheological tests, these effects were not perceived. However, a similar behavior was reported by Poumaere et al. (2014), in the investigation of unstable pipe flows for Carbopol® gels, and also previously reported by Benmouffok-Benbelkacem et al. (2010) in rheometric studies, indicating that the elastic effects of material play an important role in the yield transition of viscoplastic fluids. Finally, at t'=15, the fluctuations are minimal and the velocity profiles for fluid C-25 (Fig. 5.10g) and fluid C-50 (Fig. 5.11g), have an almost flat or plug shape, which is characteristic of materials that flow with solid-like behavior. Under these circumstances, it is observed that the flow of the fluids is only due to wall slip (BARNES, 1995; PIAU, 2007) and that the dimensionless slip velocity (u'_s) is greater for the fluid C-50 compared to fluid C-25, which is to be expected due to high viscosity and according to (COHEN; METZNER, 1986; MEEKER et al., 2004) this is one of the factors that influence sliding in smooth-walled pipe flows. This flow regime is phenomenologically consistent with the observations presented by Pérez-González et al. (2012) and Younes et al. (2020a) for macro and microexperimental setups, respectively.

On the other hand, it is also important to highlight that the wall shear stress for which the velocity profile shows a moderate displacement in Fig. 5.10g (τ_w=0.8 Pa) and Fig. 5.11g (τ_w=14.10 Pa) is lower than the yield stresses calculated in rheological creep tests with CH-PP geometry (in the absence of slip). In contrast, these wall shear stress values are closer to the yield stress values calculated for S-PP (in the presence of slip). However, although the shape of the velocity profile appears almost flat, it is impossible to consider that these stress values correspond to the yield stress of material because there is a development of movement. The determination of exact yield stress value by rheometric tests requires many experimental tests, which would be unworkable. As an alternative, Pérez-González et al. (2012) proposes the use of the velocity profiles obtained from the flow visualization to calculate the yield stress. In subsection 5.3.2 this method is used to solve this problem.

The second flow pattern is observed when the applied wall shear stresses exceed the yield stress. The velocity profiles of Fig. 5.10b, Fig. 5.10e, and Fig. 5.10h show a flat or plug-like zone around the centerline of the pipe and a partially yielded region near the pipe wall, due to large values of the velocity gradients. This behavior is also observed for the fluid C-50, for the velocity profiles of Fig. 5.11b, Fig. 5.11c, Fig. 5.11e, and Fig. 5.11h. The shear stresses are not great enough to yield the material along the pipe in the measured dimensionless time. This flow pattern may be related to the coexistence of solid and fluid phases [region S+F in Fig. 5.4]. A particular case is observed for the fluid C-25 in Fig. 5.10c and Fig. 5.10f, initially the velocity profiles develop a more parabolic profile, similar to the velocity profile of a

Figure 5.10 – Evolution of velocity profile ($u/\bar{U}$) for the fluid C-25 measured in three dimensionless times: a), b), c) for t'= 0.74; d), e), f) for t'= 0.94, and g), h), i) for t'= 15. u'_s is the slip velocity dimensionless by the mean velocity ($u_s/\bar{U}$). The error bars are defined by the root mean square deviation of the velocity profiles and the error of the PIV technique.

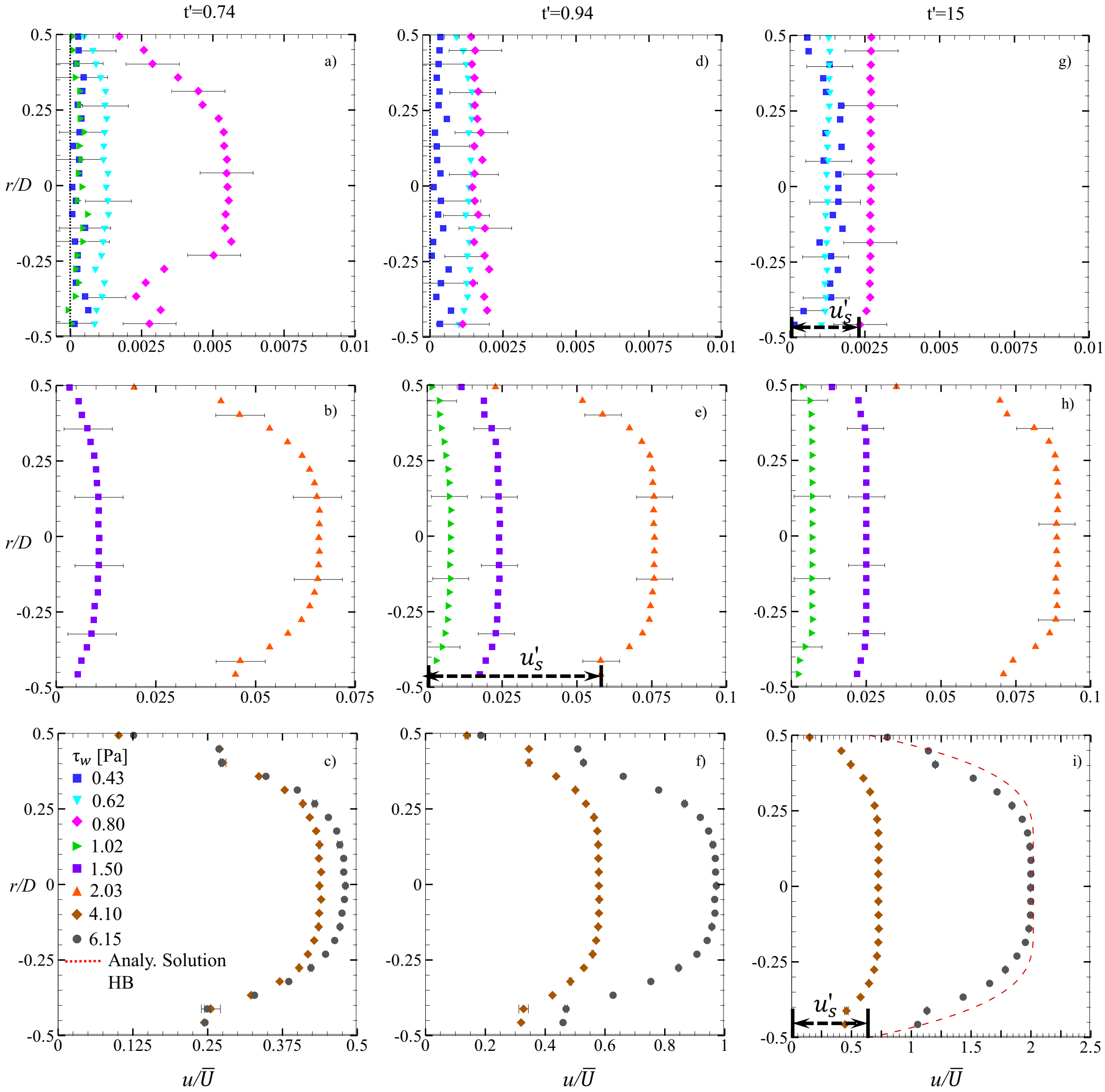

Source: Author (2021).

Newtonian fluid to later present plug-like flow. This behavior was also observed by Liu and Bruyn (2018) and discussed in more detail in work presented by Blanco (2019), where this fact is related to the low yield stress of the material. On the other hand, and according to Dinkgreve et al. (2017), a viscoelastic response of the material may also be responsible for this behavior because, in your research, the appearance of a Newtonian regime under the increase in shear stress was observed. Finally, the fluid C-25 (Fig. 5.10i) and the fluid C-50 (Fig. 5.11f and Fig. 5.11i) yielded completely, and the radius of central plug-like decreases, qualitatively indicating that the flow corresponds to the fluid regime (F) observed in the tests of the Fig. 5.4. As a quantitative argument, it is observed that in the framework of a yield stress fluid, the velocity profiles of Fig. 5.10i and Fig. 5.11i, are fitted with good agreement with the Hagen–Poiseuille flow of a Herschel–Bulkley fluid (DAMIANOU et al., 2014) and described by Eq.(5.3), with APE of 4% y 5%, respectively.

Figure 5.11 – Evolution of velocity profile ($u/\bar{U}$) for the fluid C-50 measured in three dimensionless times: a), b), c) for t'= 0.74; d), e), f) for t'= 0.94, and g), h), i) for t'= 15. u'_s is the slip velocity dimensionless by the mean velocity ($u_s/\bar{U}$). The error bars are defined by the root mean square deviation of the velocity profiles and the error of the PIV technique.

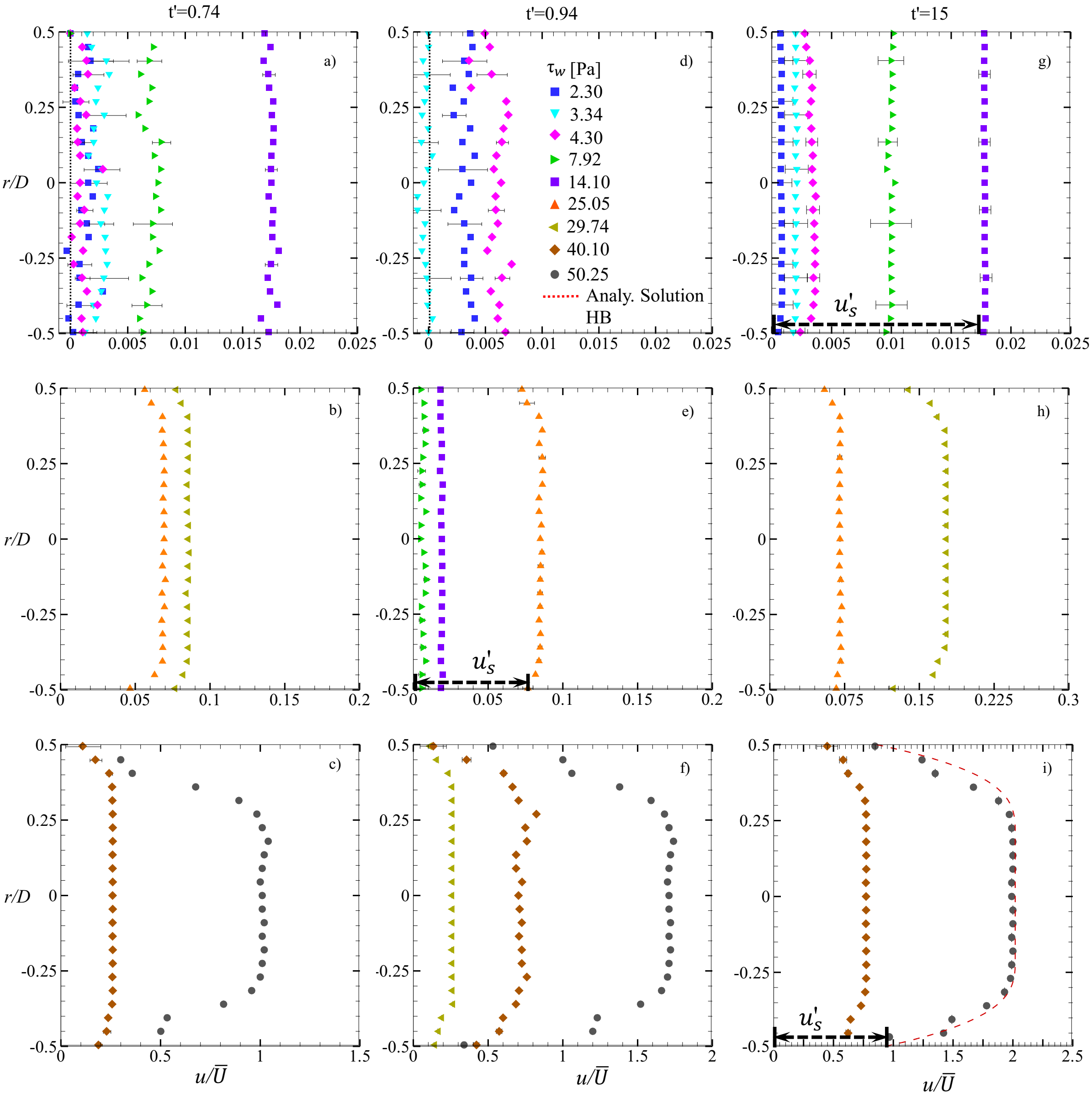

Source: Author (2021).

$$
u = u_s + \left\{ \begin{array}{ll} \frac{nR}{(n+1)}\left(\frac{\tau_w}{k}\right)^{1/n}(1-\phi)^{(n+1)/n} & \text{for } |\mathrm{r}| < \mathrm{R_p} \\ \frac{nR}{(n+1)}\left(\frac{\tau_w}{k}\right)^{1/n}\left[(1-\phi)^{(n+1)/n} - \left(\frac{r}{R}-\phi\right)^{(n+1)/n}\right] & \text{otherwise} \end{array} \right\} \tag{5.3}
$$

Concerning the wall slip of viscoplastic flows in acrylic pipe analyzed in the present study, it is observed that u'_s continues to increase beyond the yield stress and as a function of the wall shear stress, as reported by Pérez-González et al. (2012). The slip velocity values were estimated performing a second-order polynomial fit (Eq. 2.51) from the velocity profiles obtained by the PIV technique at $r=\pm R$. The Levenberg-Marquardt nonlinear fitting procedure, implemented under the OriginLab® and Matlab® software, were used to obtain the (u'_s) data. For the values of u'_s obtained, it is observed that the fluid C-25, when τ_w=2.03 Pa is applied at t'=0.94, the dimensionless slip velocity u'_s=0.058 and for τ_w=6.15 Pa at t'=15, u'_s=0.65, which is an order of magnitude greater, and represents 77.3% and 32.5% of the total dimensionless velocity, respectively. For the case of the fluid C-50, when τ_w=25.05 Pa at t'=0.94, the u'_s=0.079, and for τ_w=50.25 Pa at t'=15 u'_s=0.95, and represent 93% and 47.5% of the total dimensionless velocity, also respectively. These results show that in correspondence with each flow regime, the temporal evolution of the wall slip behavior is different from zero ($u'_s \neq 0$ in $r=\pm R$), which indicates that the slip phenomena must be considered in the yield transition of viscoplastic fluids.

5.3.1.3 Slip velocity behavior

Wall slip is quantified by the relative fluid-solid velocity at the interface. Section 5.3.1.2 presented the estimation of the slip velocity for the several flow conditions analyzed and a dependency relationship between u_s and τ_w was observed. In this section, the dependence of the wall slip velocity is scaled not only on the wall shear stress but also with the pressure drop and the velocity gradients. The scale laws obtained are compared with the results of other works.

Figure 5.12 – Dependence of the wall slip velocity as a function of dimensionless time when τ_w is applied. The red and green symbols refer to fluid C-25 (τ_w= 1.50 Pa) and fluid C-50 (τ_w= 25.05 Pa), respectively. The full line is the power-law fit for the fluids: C-25, $u_s \propto t'^{4.45\pm0.14}$; C-50, $u_s \propto t'^{1.61\pm0.18}$. The error bars are defined by the root mean square deviation of the slip velocity and the error of the PIV technique. The symbols marking the highlighted regions denote the deformation regimes and are explained in the text: (S)–solid, (S+F)–solid–fluid coexistence, (F) – fluid.

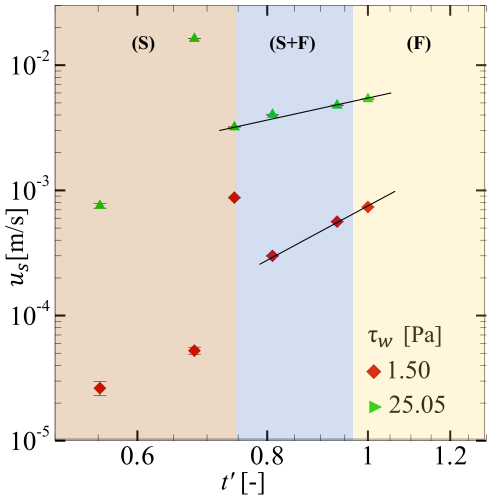

Source: Author (2021).

To obtain a vision of the dependence of the slip velocity on dimensionless time, the analysis is started by presenting the temporal evolution of u_s for two flow conditions. The red and green symbols are the results obtained for fluids C-25 and C-50, respectively. For simplicity and due to the behavior for the other flow conditions is similar, the data are presented for one wall shear stress value for each fluid. Figure 5.12

shows that for stress values lower than the yield stress (region S), the data are scattered, and it is not possible to scale the dependence of the slip velocity in this region. In contrast to the behavior in the solid region, as stress increases, within the solid-fluid transition regime (region S + F) and beyond in the fluid regime (region F), the velocity can be scaled with time as $u_s \propto t'^{4.45\pm0.14}$ for fluid C-25 and $u_s \propto t'^{1.61\pm0.18}$ for fluid C-50. This result is consistent with Liu and Bruyn (2018), they studied the Carbopol® gel flow using a smooth pipe as a function of time, they reported that for low wall shear stresses, the slip velocity slightly constant, but when the wall shear stress increases, the slip velocity also increases, and for a time interval [120-250 s, see Fig. 5 in your work] and before reach a plateau point, it is possible to scale the dependence as $u_s \propto t'^{2.46\pm0.22}$. This value differs from that obtained in the present study. However, as the scale law found is sensitive to fluid displacement rates, it is possible that this is the cause of this discrepancy. On the other hand, the rheological properties of the material can also influence (nearly 10 units difference in both the yield stress and the consistency). However, based on this comparison, it is evident that regardless of the condition flow (displacement rate), the slip velocity is correlated to the rheological properties and only scales with time when $\tau_w > \tau_0$.

Figure 5.13 – Dependence of the wall slip velocity on the pressure drop at two dimensionless times for a) fluid C-25 and b) fluid C-50. The green and blue square symbols refer to *t′*= 0.74 and the gray and brown diamonds refer to *t′*= 15. The full and dashed line in Fig. a) represents the power-law fit at *t′*= 15, $u_s \propto \Delta p^{2.88\pm0.19}$ and *t′*= 0.74, $u_s \propto \Delta p^{1.25\pm0.46}$, respectively. Fig. b), the full and dashed line is the power-law fit for $u_s \propto \Delta p^{2.01\pm0.36}$ and $u_s \propto \Delta p^{1.84\pm0.21}$ at same times. The error bars are defined by the root mean square deviation of the slip velocity and the error of the PIV technique.The symbols marking the highlighted regions denote the deformation regimes and are explained in the text: (S)–solid, (S+F)–solid–fluid coexistence, (F) – fluid.

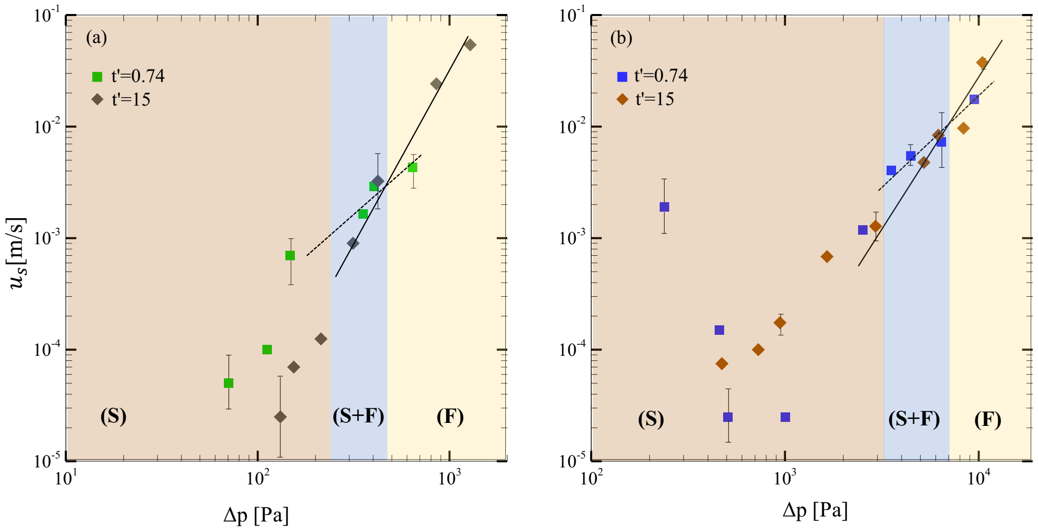

Source: Author (2021).

Figure 5.13 shows the dependence of the slip velocity of the pressure drop in the test section. The results obtained for the fluid C-25 and C-50 are shown in Fig 5.13a and Fig 5.13b, respectively. Initially, the same behavior of the dependence of the slip velocity on dimensionless time is observed, that is, only in the transition region (S+F) and in the fluid region (F), the sliding speed is scaled with pressure drop as $u_s \propto \Delta p^{2.88\pm0.19}$ (full line) and $u_s \propto \Delta p^{1.25\pm0.46}$ (dashed line), for fluid C-25 and as $u_s \propto \Delta p^{2.01\pm0.36}$ (full line) and $u_s \propto \Delta p^{1.84\pm0.21}$ (dashed line) for fluid C-50, at *t′*= 15 and *t′*= 0.74, respectively. An important detail is related to the shift in the value of the power-law coefficient, which increases with dimensionless time in both fluids, indicating that any significant alteration in the pressure drop is reflected in an increase in the slip velocity. These scales are very close to the scale obtained by Poumaere et al. (2014), in the unstable study of Carbopol® gels in the presence of wall slip, where $u_s \propto \Delta \mathrm{p}^2$. It is observed that the results for the fluid C-50 are in better agreement when compared to the fluid C-25. However, the scale law obtained by Pérez-González et al. (2012), in the investigation of yielded of Carbopol® gels in glass capillaries, $u_s \propto \Delta \mathrm{p}^{0.876}$, different from the results presented in this study and from Poumaere et al. (2014). Since the scale law is independent of the flow instability, which is verified due to similar results with Poumaere et al. (2014), it is believed that the cause of this discrepancy is also related to the rheological properties of the fluids used, which have differences close to an order of magnitude between the yield stress and the fluid consistency index. On the other hand, it is observed that the power-law fits overlap, this fact indicates that from this point the region of partial deformation (region S + F) ends and the fluid region begins, indicating that for all the values of pressure drop greater than this point the fluid flows without restrictions. Finally, the results indicate that independent of the flow stability, the slip velocity is affected by the rheological properties of the material and that only in the transition (region S+F) and fluid (region F) regimes, the slip velocity is scaled with the pressure drop.

Figure 5.14 – Dependence of the wall slip velocity on the velocity gradients at three dimensionless times for a) fluid C-25 and b) fluid C-50. The red and magenta square symbols refer to t'= 0.74; the green and cyan triangles refer to t'= 0.94; the blue and brown diamonds refer to t'= 15. The full and dashed line in Figure a) represents the power-law fit at t'= 15, $u_s \propto \frac{dU}{dr}\ |_{r=\pm R}{}^{1.38\pm0.10}$ and t'= 0.94, $u_s \propto \frac{dU}{dr}\ |_{r=\pm R}{}^{0.5\pm0.10}$. Figure b) $u_s \propto \frac{dU}{dr}\ |_{r=\pm R}{}^{3.75\pm0.10}$ at t'= 15; $u_s \propto \frac{dU}{dr}\ |_{r=\pm R}{}^{0.94\pm0.14}$ at t'= 0.94; $u_s \propto \frac{dU}{dr}\ |_{r=\pm R}{}^{0.39\pm0.02}$ at t'= 0.74. The error bars are defined by the root mean square deviation of the date. The symbols marking the highlighted regions denote the deformation regimes and are explained in the text: (S)–solid, (S+F)–solid–fluid coexistence, (F) – fluid.

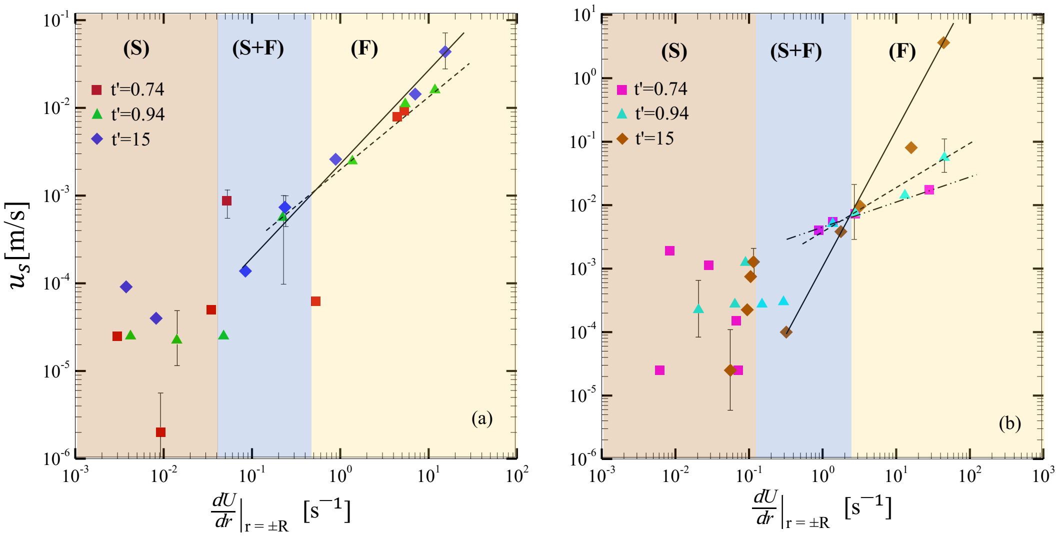

Source: Author (2021).

To get better insight of the previous correlation, the dependence of the slip velocity on the wall velocity gradients is analyzed. The $\frac{dU}{dr}\ |_{r=\pm R}$ measurements are shown for the fluid C-25 in Fig 5.14a, and for the fluid C-50 in Fig 5.14b. The results were obtained for three dimensionless times, t'=0.74,

t'=0.94, and t'=15, as described in Fig 5.14. For each dimensionless time, the values of $\frac{dU}{dr}\ |_{r=\pm R}$ were calculated using a second-order polynomial fit (Eq. 2.31) in r=$\pm R$, implementing under the classical Levenberg-Marquardt fit, using OriginLab® and Matlab® software. It is initially observed that for t'=0.74 in the region (S), the slip velocity does not show a relationship between the data, this behavior is the same for the two fluids and consistent with the results plotted in Fig 5.12 and Fig.5.13. Only in the region (S+F), the fluid C-50 shows a correlation that reaches up to the region (F), where a power-law fit was obtained as $u_s \propto \frac{dU}{dr}\ |_{r=\pm R}{}^{0.39\pm 0.02}$, in contrast to the fluid C-25 where due to the dispersion of the data it was not possible. For t' = 0.94, the slip velocity in the region (S) is slightly constant for the fluid C-25, which is related to the dimensionless time measured τ_w is almost reaching the set value. On the other hand, the fluid C-50 presents a peak before the region (S+F), and that breaks the slightly constant trend presented for the first values of the slip velocity, probably caused by the destructuring that is in process. Beyond the region (S), the slip velocity data correlates with good agreement, that is, in the regions (S+F) and (F) and is scaled as $u_s \propto \frac{dU}{dr}\ |_{r=\pm R}{}^{0.5\pm 0.10}$, for fluid C-25 and $u_s \propto \frac{dU}{dr}\ |_{r=\pm R}{}^{0.94\pm 0.14}$ for fluid C-50. Finally, for t' = 15, similar behavior is observed for the solid-like behavior regions and the slip velocity between the transition and fluid regions is scaled as $u_s \propto \frac{dU}{dr}\ |_{r=\pm R}{}^{1.38\pm 0.10}$ for fluid C-25 and as $u_s \propto \frac{dU}{dr}\ |_{r=\pm R}{}^{3.75\pm 0.10}$ for fluid C-50, the fits overlap and indicate the beginning of the region (F), where the fluid is completely viscous behavior. These results are in good agreement with the results reported by Younes et al. (2020a) in the study of Carbopol® gel flows in microchannels, which observes three deformation regimes. For the first regime, corresponding regime (S), it was not possible to obtain a correlation of the data, due to the data's dispersion. In the transition regime (S+F), the slip velocity was scaled as $u_s \propto \frac{dU}{dy}\ |_{w}{}^{0.5}$ and in regime (F), as $u_s \propto \frac{dU}{dy}\ |_{w}{}^{0.1}$. It is observed that these scales are close to those obtained for t'=0.94 and t'=0.74, due to similar rheological properties (yield stress and consistency index less than one order magnitude), this fact confirms that the discrepancies due to rheological properties are true. On the other hand, this comparison shows that the dependence of the slip velocity is affected by the deformation regimes and that it is not universal, as reported by Poumaere et al. (2014). Meeker et al. (2004) by macro-rheological observation confirms the existence of three deformation regimes; however, since the scales are obtained using a microelastohydrodynamic lubrication, and as the present protocol does not contemplate these characteristics, it is not possible to perform a comparison.

In contrast to studies conducted by (NGUYEN; BOGER, 1992; SETH et al., 2008; BALLESTA et al., 2012) that report the decrease in the slip velocity with the applied stresses (velocity gradients), beyond the yield stress, this investigation reports that the slip velocity continues to increase once the point of yield is exceeded, and this increase is marked by three deformation regimes as shown in Fig 5.14. This conclusion is consistent with the results reported by Pérez-González et al. (2012) and Poumaere et al. (2014) for the case of constant and unstable flows de Carbopol® gels. Although they report that the increase is monotonous even in the region of solid-like behavior, which was not evidenced here and neither in (YOUNES et al., 2020a). However, the statements are valid for the fact that the slip velocity increases beyond the yield stress.

As the results obtained, indicate a relationship between the slip velocity and the wall shear stress, and under the assumption that this relationship exists due to a depleted layer of width (δ) that prevents the fluid from adhering to the solid limit (BINGHAM, 1922), the relationship proposed by Kalyon (2005) and described in chapter 2 is used and repeated here for convenience, Eq.(5.4), to obtain a simple phenomenological scale of the behavior of the sliding of the wall of the viscoplastic fluids analyzed.

$$u_s = \beta(\tau_w)^{\frac{1}{n_b}} \tag{5.4}$$

where β is expressed as:

$$\beta = \frac{\delta}{k_b^{\frac{1}{n_b}}} \tag{5.5}$$

and β relates the width of the slip layer δ to the consistency index k_b and the power-law index n_b of binder fluid. As Carbopol® is considered as a jammed system of swollen gel microparticles (PIAU, 2007), and the solvent used to obtain the fluids was distilled water ("binder fluid"), it is considered Newtonian fluid, k_b=1×10^{-3} Pa.s and n_b=1.

Figure 5.15 – Dependence of the wall slip velocity on the wall shear stress at three dimensionless times for a) fluid C-25 and b) fluid C-50. The red and magenta square symbols refer to t'= 0.74; the green and cyan triangles refer to t'= 0.94; the blue and brown diamonds refer to t'= 15. The full and dashed line in Figure a) represents the power-law fit at t'= 15, $u_s \propto {\tau_w}^{1.13\pm0.04}$ and t'= 0.94, $u_s \propto {\tau_w}^{1.52\pm0.22}$, respectively. Figure b) the full line, the dashed line, and dot-dashed line are $u_s \propto {\tau_w}^{1.45\pm0.10}$ at t'= 15; $u_s \propto {\tau_w}^{0.91\pm0.14}$ at t'= 0.94; $u_s \propto {\tau_w}^{0.39\pm0.02}$ at t'= 0.74. The error bars are defined by the root mean square deviation of the slip velocity and the error of the PIV technique.The symbols marking the highlighted regions denote the deformation regimes and are explained in the text: (S)–solid, (S+F)–solid–fluid coexistence, (F) – fluid.

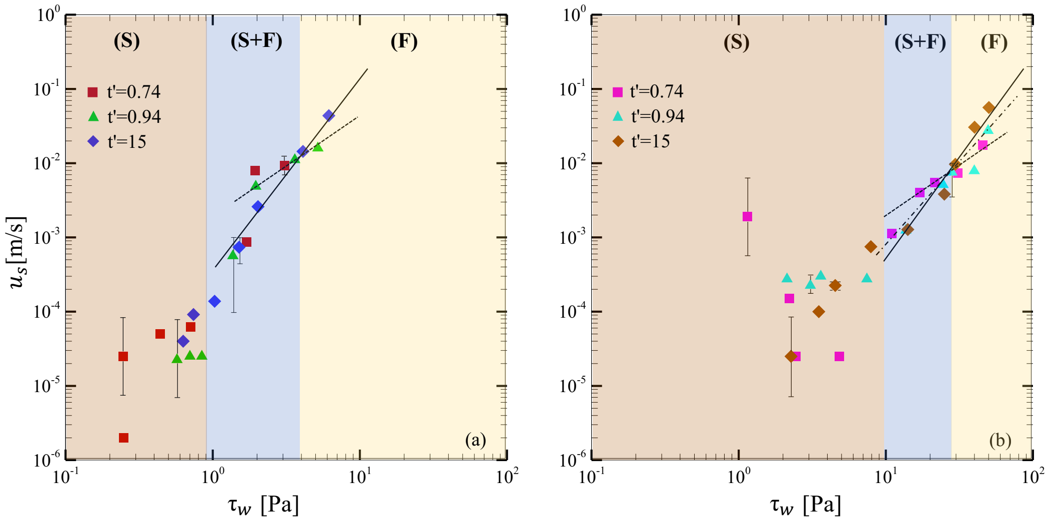

Source: Author (2021).

The dependence of the slip velocity on the wall shear stress is shown in Fig. 5.15a for fluid C-25, and for fluid C-50 in Fig. 5.15b. The three regimes of deformation observed previously in the two fluids are again perceived. For t'=0.74, the data's dispersion does not follow any correlation in the two fluids (region S). For the same dimensionless time in the region (S+F), the increase in the slip velocity is observed and only for the fluid C-50 the data correlated as $u_s \propto {\tau_w}^{0.39\pm0.02}$. For t'=0.94 the behavior of the slip velocity is scaled from the transition region as $u_s \propto {\tau_w}^{1.52\pm0.22}$, for the fluid C-25 and as $u_s \propto {\tau_w}^{0.91\pm0.14}$ for the fluid C-50. For t'=15, again the data overlaps and marks the start of the fluid region (F). Power-law scales equivalent to $u_s \propto {\tau_w}^{1.13\pm0.04}$ for the fluid C-25 and $u_s \propto {\tau_w}^{1.45\pm0.10}$ for the C-50 fluid are obtained. It is generally observed that the power-law scales are almost linear, which is in good agreement with the assumption that the binder fluid is Newtonian, n_b=1. A similar scale law was obtained by Poumaere et al. (2014) and Pérez-González et al. (2012), $u_s \propto {\tau_w}^{1.32\pm0.26}$ and $u_s \propto {\tau_w}^{0.9}$, respectively. Although both the scale law obtained by them and the scale law presented here, differ from those predicted theoretically by Piau (2007), $u_s \propto {\tau_w}^{0.33}$ for a loosely packed system and $u_s \propto {\tau_w}^{2}$ for a closely packed system. In contrast, Younes et al. (2020a), obtained a perfectly linear power-law scale, $u_s \propto \tau_w$, but only in the fluid regime. The difference between the experimental and theoretical data may be related to the fact that the fluid was considered non-Newtonian in Piau (2007). On the other hand, it is observed that as the dimensionless time increases, the scale index also increases, reinforcing the fact that the slip velocity is sensitive to shift in the wall shear stresses.

In this study the factor β measured for the fluid C-25 is β=1.01$\times$10^{-4} mPa.s^{-1}, which leads to a slip layer thickness $\delta \approx$0.101μm. For the fluid C-50 β=5.15$\times$10^{-4} mPa.s^{-1}, and the estimated slip layer thickness is $\delta \approx$0.329 μm. The thickness of the slip layer found is of the same width order as reported by Jiang et al. (1986), ($\delta \approx$0.1μm), Poumaere et al. (2014), ($\delta \approx$0.23μm), and Younes et al. (2020a), ($\delta \approx$0.07μm). The estimation of the thickness of the slip layer was carried out for t'=15. However, the thickness of the slip layer calculated by simple estimates is too small to be directly visualized from the flow, and the hypothesis underlying the prediction of this scale is simply hypotheses for now. According to (YOUNES et al., 2020a), the best practice is to relate the rheological behavior in steady-state with the results obtained experimentally from the velocity gradients.

5.3.2 Calculation of shear stress required for yielding transition from PIV measurements

As discussed in the previous section, obtaining the yield stress from rheometric tests would require a large number of experimental points, which would make it impractical to perform. Another method that also requires many points is proposed by Kalyon (2005), where if $Q_s/Q < 1$, the fluid flows. To found this ratio, the contribution of slip to the total flow rate (Q) is calculated, and then Q_s/Q, and where Q_s=($\pi u_s D^2$)/4, with u_s estimated from the non-linear fit of the velocity profiles at r=$\pm R$. According to Pérez-González et al. (2012) a simple method that can be used to calculate yield stress is using the velocity profiles obtained by visualizing the flow field. This method requires the calculation of the first derivative of velocity profile, which corresponds to the true shear rate (velocity gradient) for unidirectional flow, as shown in Fig. 2.15, of chapter 2.

The first derivative of the velocity as a function of ratio r_p/R is presented in Fig. 5.16a for fluid C-25, and for fluid C-50 in Fig. 5.16b, for the wall shear stress values, τ_w=6.5 Pa and τ_w=50 Pa, respectively. The ratio value at which the velocity gradient $\frac{dU}{dr}\ |_r$= 0, for fluids C-25 and C-50 is r_p/R=$\pm$0.28 for fluid C-25 and r_p/R=$\pm$0.45, and correspond to aτ_0=1.16$\pm$0.05 Pa and τ_0=22.14$\pm$0.9 Pa, respectively. These yield stress values differ significantly from the values calculated by creep tests for the S-PP and CH-PP geometries. However, if the same procedure is performed for the velocity profiles assuming symmetry in Fig. 5.10 and Fig. 5.10, except Fig. 5.10a; Fig. 5.11a; Fig. 5.10d; Fig. 5.11d and Fig. 5.10g; Fig. 5.11g, the value of yield stress is τ_0=0.76$\pm$0.038 Pa for fluid C-25 and τ_0=10.14$\pm$0.51 for fluid C-50. The significant discrepancy of the data does not indicate that the rheological tests are wrong, it indicates that

Figure 5.16 – Velocity gradient as a function of the dimensionless radial position for the velocity profile obtained at t'= 15 for a) fluid C-25, τ_w= 6.15 Pa and b) fluid C-50, τ_w= 50.25 Pa. The vertical lines indicate the value of r_p/R at which $\frac{dU}{dr}\ |_r$= 0. The value of r_p/R ratio and of the yield stress when $\frac{dU}{dr}\ |_r$= 0 for the fluids C-25 and C-50 are r_p/R = ±0.28 (τ_y = 0.76 Pa) and r_p/R = ±0.45 (τ_y = 10.14 Pa), respectively. The error bars are defined by the root mean square deviation of the velocity gradient for three positions *Z/D*.

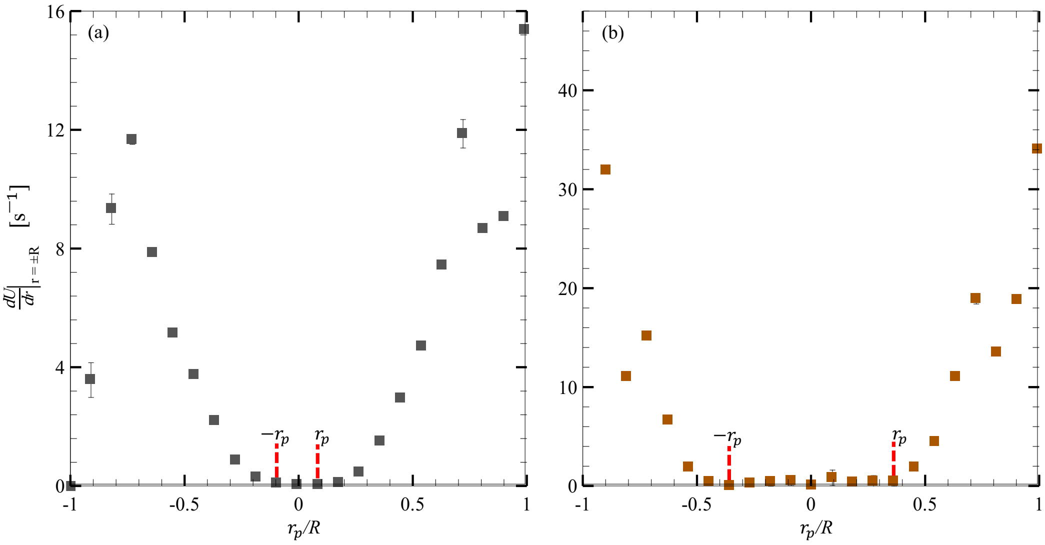

Source: Author (2021).

more points were needed to be measured to obtain the true yield stress value, but as discussed before, it is impracticable and could delay the investigation. On the other hand, the presence of wall slip is evident and the yield stress value calculated through the velocity profiles is in better agreement with the creep tests using S-PP, with a percentage deviation for the fluid C-25 equal to 4% and 1.4% for the fluid C-50. This confirms that under the experimental conditions setup in this investigation, the yield transition is a process coupled with wall slip.

Note that the plug radius r_p is a function of wall shear stress τ_w. The dependence of r_p on τ_w for two dimensionless times is presented in Fig.5.17a, for fluid C-25 and Fig.5.17b for fluid C-50. It is observed that for t'=0.74 (red symbols) Fig.5.17a, the plug radius presents very low values for low wall shear stresses, which contrasts with the dependence of the plug radius for yield stress fluids (COUSSOT, 2005). However, this atypical behavior is consistent with that shown in Fig.5.10c and Fig.5.10f, where the fluid presents a more parabolic profile with almost no presence of a central plug. The causes of this behavior were previously discussed. For the case of fluid C-50 at the same t' (magenta symbols) in Fig.5.17b, the behavior of plug radius is more consistent with a yield stress fluid, it is observed that for low values of wall shear stress the plug radius is practically independent on applied stress and the movement is solid-like (core un-yielded fluid). For t'=15, the plug radius of fluid C-25 (blue symbols), presents a behavior as solid-like (region S), but beyond the critical value of wall shear stress the size of plug radius decrease monotonically and fits in good agreement with the prediction for HB model, given by r_p=$R\tau_0/\tau_w$, with a APE qual to 10%. For the fluid C-50, similar behavior is observed, and the adjustment presents a APE of 15%. The decrease in plug radius size is consistent with fluid behavior when the shear stresses associated with the yielded wall layers exceed the total yield stress of the fluid and the yielded region approaches the

Figure 5.17 – Variation of the plug radius on the wall shear stress at two dimensionless times for a) fluid C-25 and b) fluid C-50. The red and magenta square symbols refer to t'= 0.74 and the blue and brown diamonds refer to t'= 15. The full line represents the Herschel–Bulkley fit. The error bars are defined by the root mean square deviation of plug radius. The symbols marking the highlighted regions denote the deformation regimes and are explained in the text: (S)–solid, (S+F)–solid–fluid coexistence, (F) – fluid.

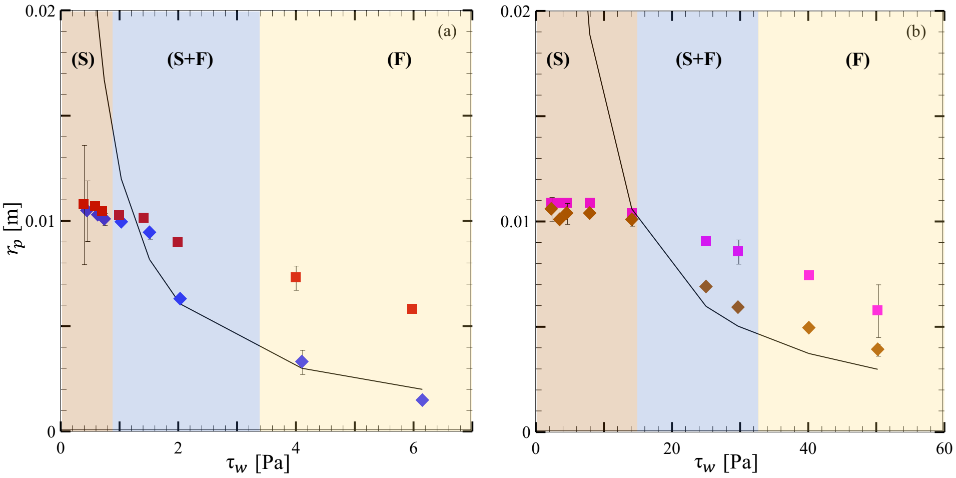

Source: Author (2021).

center of the pipe.

On the other hand, it is observed that the differences between the sizes of the final plug in the fluid regime of each material analyzed depend on the value of the apparent viscosity (consistency index), as is the case of the fluid C-50 for which $k = 2.62$ is greater compared to fluid C-25, $k = 0.63$. Finally, it is possible to conclude that the presented method based on the first derivative of the velocity profiles is reliable and allows obtaining a yield stress value that is consistent with the yielded of the materials in a smooth pipe with the presence of wall slip. Furthermore, it is also possible to say that whenever the velocity profiles are available this method can be used for other fluids.

6 FINAL REMARKS

In the present work, the start-up flow of two viscoplastic materials in a smooth pipe with the presence of wall slip were analyzed and compared using different flow conditions given by the imposition of pressure drop (wall shear stresses).

As part of the methodology to achieve the proposed objectives, an experimental configuration was built and the PIV technique was used as a visualization method. The methodology was tested with Newtonian fluid flow in a straight pipe. The data obtained were compared and validated with the analytical solution in a transient regime for a Newtonian fluid displaced by a pressure drop, showing a good agreement and validating the methodology. For the tests, a commercial ultrasound gel composed of Carbopol® in two different concentrations was used. Test protocols were developed to obtain the steady flow curves of the materials in the experimental setup, perform the start-up flow tests, and record the flow visualization images.

The steady flow curves obtained experimentally for the materials (fluids C-25 and C-50) were compared with the rheometric data. It was observed that the two fluids presented values lower than the data measured in the rheometer, indicating a slip of the gel on the internal walls of the pipe. The data were corrected for the slip based on the truly shear volumetric flow rate (MACOSKO; LARSON, 1994; AKTAS et al., 2014), resulting in a better comparison with the rheometric data. Additionally, the behavior of the fluids as shear stress is applied was analyzed by rheological creep tests. The results showed that for low values of shear stress, i.e., lower than the yield stress, the fluids had a solid-like behavior (region S). This behavior changed when the shear stress was slightly greater than the yield stress, and it was consistent with a region of coexistence of solid and fluid states (region S + F). Beyond yield stress, for greater shear stress values, the material showed a totally fluid behavior (region F).

The visualization of the start flow of the fluids in the experimental setup also identified three states of deformation consistent with states found in the rheometric tests. These states of deformation were first observed through the evolution of the flow and deformation fields obtained from the visualization of the fluids in six dimensionless times. For the C-25 fluid, it was observed that for wall shear stresses below the yield stress, the dimensionless velocity values ($u/\bar{U}$) showed fluctuations, but these fluctuations decrease or practically disappear for wall shear stresses greater than the yield stress. The same behavior was observed for the C-50 fluid, the dimensionless velocity ($u/\bar{U}$), fluctuated with greater intensity. This fluctuating nature for the first dimensionless times was related to the beginning of a process of destructuring of the materials and to the elastic effects that can arise when the material is exposed to an external force, this behavior was attributed to the region (S) and It was also observed in the creep tests. For wall shear stresses slightly greater than the yield stress, the fluctuations for the two fluids smoothed out, (region S + F). Finally, for shear stresses beyond the yield stress, a consistent flow pattern was observed, where the material flows (region F) without restrictions.

On the other hand, the following question arose: does the fluid break from the center towards the wall or from the wall towards the center? The answer was obtained through the deformation fields ($\dot{\gamma}/\dot{\gamma}_{corr}$) of the fluids. The results showed that the temporal evolution of the fluid deformation begins near the wall where the highest velocity gradients are observed and then extends towards the central plane of the pipe. This confirms that the structure of a viscoplastic gel, at least within the framework of the study carried out, presents an adhesive failure, that is, the gel breaks at the interface of the surface of the pipe and the gel network. The deformation pattern was the same for the two fluids, and as in the flow fields, fluctuations were observed for values below the critical shear rate (region S), decreasing in the region (S + F) and practically disappearing. in the region (F). Finally, the visualization of the yield of viscoplastic fluids made it possible to pose the assumption of "static" or non-sheared areas over which the fluid could be sliding, which is a phenomenon normally present in yield stress fluids.

In order to better appreciate the results shown in the flow and deformation fields, the temporal evolution of the dimensionless velocity profiles for all the flow conditions studied were plotted. The data allowed to verify the three deformation regimes and that the apparently "visualized" wall slip in macroscopic layers with no or almost zero movement in the flow fields was present in the yielding of the fluids. The dimensionless velocity profiles also showed that wall slip increases with the wall shear stress.

From the slip behavior observed in the evolution of the dimensionless velocity profiles, scaling was performed with other hydrodynamic quantities such as shear stress and velocity gradients in the wall. The data showed that the slip velocity is scaled in the form of a power-law only between the regions (S+F) and the region (F), due to that in the solid region, the slip velocity is independent of the values of shear stress and the velocity gradient. Based on the dependence of the slip velocity on the shear stress, a phenomenological picture of the slip behavior was established and the value of the thickness of the slip layer was estimated, whose value was on the order of microns, a minimal value for being observed within the resolution of the visualization technique used.

A method to calculate yield stress was also presented in this study. This practical and easy method proposed to use the first derivative (true shear rate) of the velocity profiles and find where it was zero, i.e., where the wall shear stress reached the value of the yield stress. The value found for each fluid was relatively less than that calculated by the creep tests, which indicated that under the established experimental conditions, the flow reset occurs on the influence of the slip. This data also confirmed that to find the true yield stress through rheometric tests, a large number of points is necessary, which makes the process impractical. Additionally, it was obtained that the plug radius in regime (F) is greater for the fluid C-50 compared to the fluid C-25, due to the consistency index values and that it decreases as a function of the wall shear stress.

Finally, this experimental research showed that it is possible to obtain relevant information in relation to the complex behavior of viscoplastic fluids. This information allows it possible to reduce the gap of experimental data available under such flow conditions. In addition, it was possible to use some methodologies to obtain quantitative data on yield stress and factors that affect its calculation, such as wall slip velocity. These data prove that within the framework of a transient process the PIV technique can be used to represent phenomena of this type.

6.1 Suggestions for future research

For the flow of viscoplastic material through a smooth straight pipe the following topics could be considered in future research:

1. Perform tests with other viscoplastic fluid concentrations in order to obtain more comparative data.
2. Visualize the start-up flow with more complex fluids, for examples: thixotropic fluids, and perform a comparative analysis with the data obtained from studies with viscoplastic fluid
3. Couple a thermostatic bath to the experimental configuration, with the purpose of evaluate the start-up flow at low temperatures.
4. Use a rough straight pipe with viscoplastic and thixotropic fluids for the purpose of obtain data that can be compared with the results for the smooth pipe.

REFERENCES

ABEDI, B.; MENDES, R.; MENDES, P. R. de S. Startup flow of yield-stress non-thixotropic and thixotropic materials in a tube. *Journal of Petroleum Science and Engineering*, Elsevier, v. 174, p. 437–445, 2019.

ADRIAN, R. J. Particle-imaging techniques for experimental fluid mechanics. *Annual review of fluid mechanics*, Annual Reviews 4139 El Camino Way, PO Box 10139, Palo Alto, CA 94303-0139, USA, v. 23, n. 1, p. 261–304, 1991.

AGARWAL, M.; JOSHI, Y. M. Signatures of physical aging and thixotropy in aqueous dispersion of carbopol. *Physics of Fluids*, AIP Publishing LLC, v. 31, n. 6, p. 063107, 2019.

AKTAS, S.; KALYON, D. M.; MARÍN-SANTIBÁÑEZ, B. M.; PÉREZ-GONZÁLEZ, J. Shear viscosity and wall slip behavior of a viscoplastic hydrogel. *Journal of Rheology*, The Society of Rheology, v. 58, n. 2, p. 513–535, 2014.

ALBA, K.; TAGHAVI, S.; BRUYN, J. R. de; FRIGAARD, I. Incomplete fluid–fluid displacement of yield-stress fluids. part 2: Highly inclined pipes. *Journal of Non-Newtonian Fluid Mechanics*, Elsevier, v. 201, p. 80–93, 2013.

BAGNATO, G.; IULIANELLI, A.; SANNA, A.; BASILE, A. Glycerol production and transformation: a critical review with particular emphasis on glycerol reforming reaction for producing hydrogen in conventional and membrane reactors. *Membranes*, Multidisciplinary Digital Publishing Institute, v. 7, n. 2, p. 17, 2017.

BALLESTA, P.; PETEKIDIS, G.; ISA, L.; POON, W.; BESSELING, R. Wall slip and flow of concentrated hard-sphere colloidal suspensions. *Journal of Rheology*, The Society of Rheology, v. 56, n. 5, p. 1005–1037, 2012.

BALMFORTH, N. J.; FRIGAARD, I. A.; OVARLEZ, G. Yielding to stress: recent developments in viscoplastic fluid mechanics. *Annual Review of Fluid Mechanics*, Annual Reviews, v. 46, p. 121–146, 2014.

BARNES, H. A. A review of the slip (wall depletion) of polymer solutions, emulsions and particle suspensions in viscometers: its cause, character, and cure. *Journal of Non-Newtonian Fluid Mechanics*, Elsevier, v. 56, n. 3, p. 221–251, 1995.

BARNES, H. A. The yield stress—a review or '$\pi\alpha\nu\tau\alpha\ \rho\varepsilon\iota$'—everything flows? *Journal of Non-Newtonian Fluid Mechanics*, Elsevier, v. 81, n. 1-2, p. 133–178, 1999.

BATCHELOR, G. *An Introduction to Fluid Dynamics*. [S.l.]: Cambridge University Press, 2000.

BENMOUFFOK-BENBELKACEM, G.; CATON, F.; BARAVIAN, C.; SKALI-LAMI, S. Non-linear viscoelasticity and temporal behavior of typical yield stress fluids: Carbopol, xanthan and ketchup. *Rheologica acta*, Springer, v. 49, n. 3, p. 305–314, 2010.

BERKER, A.; ARSDALE, W. V. Phenomenological models of viscoplastic, thixotropic, and granular materials. *Rheologica acta*, Springer, v. 31, n. 2, p. 119–138, 1992.

BHATTACHARYA SAYANTAN Y CHARONKO, J. J. y. V. P. P. cuantificación de la incertidumbre de la velocimetría de la imagen de partículas (piv) utilizando el plano del momento de correlación (mc). *Measurement Science and Technology*.

BINGHAM, E. C. *Fluidity and plasticity*. [S.l.]: McGraw-Hill, 1922. v. 2.

BIRD, R. B.; DAI, G.; YARUSSO, B. J. The rheology and flow of viscoplastic materials. *Reviews in Chemical Engineering*, De Gruyter, v. 1, n. 1, p. 1–70, 1983.

BLANCO, Y. J. G. *Visualization of viscoplastic fluid flow in an abrupt contraction using particle image velocimetry*. Dissertação (Mestrado) — Universidade Tecnológica Federal do Paraná, 2019.

BONN, D.; DENN, M. M.; BERTHIER, L.; DIVOUX, T.; MANNEVILLE, S. Yield stress materials in soft condensed matter. *Reviews of Modern Physics*, APS, v. 89, n. 3, p. 035005, 2017.

BROMWICH, T. An application of heaviside's methods of viscous fluid motion. *Journal of the London Mathematical Society*, Wiley Online Library, v. 1, n. 1, p. 10–13, 1930.

CATON, F.; BARAVIAN, C. Plastic behavior of some yield stress fluids: from creep to long-time yield. *Rheologica Acta*, Springer, v. 47, n. 5-6, p. 601–607, 2008.

CHANG, C.; BOGER, D. V.; NGUYEN, Q. D. The yielding of waxy crude oils. *Industrial & engineering chemistry research*, ACS Publications, v. 37, n. 4, p. 1551–1559, 1998.

CHEN, L.; DUAN, Y.; ZHAO, C.; YANG, L. Rheological behavior and wall slip of concentrated coal water slurry in pipe flows. *Chemical Engineering and Processing: Process Intensification*, Elsevier, v. 48, n. 7, p. 1241–1248, 2009.

CHHABRA, R. P.; RICHARDSON, J. F. *Non-Newtonian flow and applied rheology: engineering applications*. [S.l.]: Butterworth-Heinemann, 2011.

CHURAEV, N.; SOBOLEV, V.; SOMOV, A. Slippage of liquids over lyophobic solid surfaces. *Journal of Colloid and Interface Science*, Elsevier, v. 97, n. 2, p. 574–581, 1984.

CLARKE, P.; CHADA, S.; MENANDER, K.; SOBOL, R.; ZHANG, S. *Topical administration permitting prolonged exposure of target cells to therapeutic and prophylactic nucleic acids*. [S.l.]: Google Patents, 2007. US Patent App. 11/336,664.

COHEN, Y.; METZNER, A. An analysis of apparent slip flow of polymer solutions. *Rheologica acta*, Springer, v. 25, n. 1, p. 28–35, 1986.

COLEMAN, H. W.; STEELE, W. G. *Experimentation, validation, and uncertainty analysis for engineers*. [S.l.]: John Wiley & Sons, 2018.

COUSSOT, P. *Rheometry of pastes, suspensions, and granular materials: applications in industry and environment*. [S.l.]: John Wiley & Sons, 2005.

COUSSOT, P.; MALKIN, A. Y.; OVARLEZ, G. *Introduction: yield stress—or 100 years of rheology*. [S.l.]: Springer, 2017.

COUSSOT, P.; NGUYEN, Q.; HUYNH, H.; BONN, D. Viscosity bifurcation in thixotropic, yielding fluids. *Journal of rheology*, SOR, v. 46, n. 3, p. 573–589, 2002.

CURRAN, S.; HAYES, R.; AFACAN, A.; WILLIAMS, M.; TANGUY, P. Properties of carbopol solutions as models for yield-stress fluids. *Journal of food science*, Wiley Online Library, v. 67, n. 1, p. 176–180, 2002.

DALLA, L. *Análise Experimental da Tensão Mínima para Escoamento de Materiais Viscoplásticos em Tubos: Carbopol e Óleo Parafínico Gelificado*. Dissertação (Mestrado) — Universidade Federal do Espírito Santo, 2018.

DAMIANOU, Y.; PHILIPPOU, M.; KAOULLAS, G.; GEORGIOU, G. C. Cessation of viscoplastic poiseuille flow with wall slip. *Journal of Non-Newtonian Fluid Mechanics*, Elsevier, v. 203, p. 24–37, 2014.

DESHPANDE, A. P. Oscillatory shear rheology for probing nonlinear viscoelasticity of complex fluids: Large amplitude oscillatory shear. In: *Rheology of complex fluids*. [S.l.]: Springer, 2010. p. 87–110.

DINKGREVE, M.; DENN, M. M.; BONN, D. “everything flows?”: elastic effects on startup flows of yield-stress fluids. *Rheologica Acta*, Springer, v. 56, n. 3, p. 189–194, 2017.

DINKGREVE, M.; PAREDES, J.; DENN, M. M.; BONN, D. On different ways of measuring “the” yield stress. *Journal of non-Newtonian fluid mechanics*, Elsevier, v. 238, p. 233–241, 2016.

DIVOUX, T.; BARENTIN, C.; MANNEVILLE, S. From stress-induced fluidization processes to herschel-bulkley behaviour in simple yield stress fluids. *Soft Matter*, Royal Society of Chemistry, v. 7, n. 18, p. 8409–8418, 2011.

DIVOUX, T.; TAMARII, D.; BARENTIN, C.; MANNEVILLE, S. Transient shear banding in a simple yield stress fluid. *Physical review letters*, APS, v. 104, n. 20, p. 208301, 2010.

DOORNE, C. V.; WESTERWEEL, J. Measurement of laminar, transitional and turbulent pipe flow using stereoscopic-piv. *Experiments in Fluids*, Springer, v. 42, n. 2, p. 259–279, 2007.

DORAN, S. J.; YATIGAMMANA, D. N. Eliminating the need for refractive index matching in optical ct scanners for radiotherapy dosimetry: I. concept and simulations. *Physics in Medicine & Biology*, IOP Publishing, v. 57, n. 3, p. 665, 2012.

DZUY, N. Q.; BOGER, D. V. Yield stress measurement for concentrated suspensions. *Journal of Rheology*, SOR, v. 27, n. 4, p. 321–349, 1983.

FERNANDES, R. R.; TUREZO, G.; ANDRADE, D. E.; FRANCO, A. T.; NEGRÃO, C. O. R. Are the rheological properties of water-based and synthetic drilling fluids obtained by the fann 35a viscometer reliable? *Journal of Petroleum Science and Engineering*, Elsevier, v. 177, p. 872–879, 2019.

FORDHAM, E. J.; BITTLESTON, S. H.; TEHRANI, M. A. Viscoplastic flow in centered annuli, pipes, and slots. *Industrial & engineering chemistry research*, ACS Publications, v. 30, n. 3, p. 517–524, 1991.

FOX, R. W.; MCDONALD, A. T.; MITCHELL, J. W. *Fox and McDonald’s introduction to fluid mechanics*. [S.l.]: John Wiley & Sons, 2020.

FRITZ, G.; MARANZANO, B.; WAGNER, N.; WILLENBACHER, N. High frequency rheology of hard sphere colloidal dispersions measured with a torsional resonator. *Journal of non-newtonian fluid mechanics*, Elsevier, v. 102, n. 2, p. 149–156, 2002.

GAO, X.; XIE, Y.; WANG, S.; WU, M.; WANG, Y.; TAN, C.; ZUO, X.; CHEN, T. Offshore oil production planning optimization: An minlp model considering well operation and flow assurance. *Computers & Chemical Engineering*, Elsevier, v. 133, p. 106674, 2020.

GIUSEPPE, E. D.; CORBI, F.; FUNICIELLO, F.; MASSMEYER, A.; SANTIMANO, T.; ROSENAU, M.; DAVAILLE, A. Characterization of carbopol® hydrogel rheology for experimental tectonics and geodynamics. *Tectonophysics*, Elsevier, v. 642, p. 29–45, 2015.

GREATED, C.; SKYNER, D.; BRUCE, T. Particle image velocimetry (piv) in the coastal engineering laboratory. In: *Coastal Engineering 1992*. [S.l.: s.n.], 1993. p. 212–225.

HATZIKIRIAKOS, S. G. The onset of wall slip and sharkskin melt fracture in capillary flow. *Polymer Engineering & Science*, Wiley Online Library, v. 34, n. 19, p. 1441–1449, 1994.

ISLAM, M. T.; RODRIGUEZ-HORNEDO, N.; CIOTTI, S.; ACKERMANN, C. Rheological characterization of topical carbomer gels neutralized to different ph. *Pharmaceutical research*, Springer, v. 21, n. 7, p. 1192–1199, 2004.

JASTRZEBSKI, Z. D. Entrance effects and wall effects in an extrusion rheometer during flow of concentrated suspensions. *Industrial & Engineering Chemistry Fundamentals*, ACS Publications, v. 6, n. 3, p. 445–454, 1967.

JIANG, T.; YOUNG, A.; METZNER, A. The rheological characterization of hpg gels: Measurement of slip velocities in capillary tubes. *Rheologica acta*, Springer, v. 25, n. 4, p. 397–404, 1986.

JR, L. B.; JR, A. H. Capillary flow instability of ethylene polymer melts. *Polymer Engineering & Science*, Wiley Online Library, v. 10, n. 4, p. 193–203, 1970.

KALYON, D. M. Apparent slip and viscoplasticity of concentrated suspensions. *Journal of Rheology*, The Society of Rheology, v. 49, n. 3, p. 621–640, 2005.

KALYON, D. M.; YARAS, P.; ARAL, B.; YILMAZER, U. Rheological behavior of a concentrated suspension: A solid rocket fuel simulant. *Journal of rheology*, The Society of Rheology, v. 37, n. 1, p. 35–53, 1993.

KISSI, N. E.; PIAU, J. Slip and friction of polymer melt flows. In: *Rheology Series*. [S.l.]: Elsevier, 1996. v. 5, p. 357–388.

KOZICKI, W.; CHOU, C.; TIU, C. Non-newtonian flow in ducts of arbitrary cross-sectional shape. *Chemical Engineering Science*, Elsevier, v. 21, n. 8, p. 665–679, 1966.

LAM, Y.; WANG, Z.; CHEN, X.; JOSHI, S. Wall slip of concentrated suspension melts in capillary flows. *Powder Technology*, Elsevier, v. 177, n. 3, p. 162–169, 2007.

LARSSON, M.; DUFFY, J.; AB, M. An overview of measurement techniques for determination of yield stress. *Annu. Trans. Nordic Rheol. Soc*, v. 21, p. 125–138, 2013.

LAWAL, A.; KALYON, D. M. Squeezing flow of viscoplastic fluids subject to wall slip. *Polymer Engineering & Science*, Wiley Online Library, v. 38, n. 11, p. 1793–1804, 1998.

LINDNER, A.; COUSSOT, P.; BONN, D. Viscous fingering in a yield stress fluid. *Physical Review Letters*, APS, v. 85, n. 2, p. 314, 2000.

LITVINOV, A.; FILATOV, B. Calculation of the velocity gradient in pipes with study-state structural flow of viscoplastic fluids. 1980.

LIU, Y.; BRUYN, J. R. de. Start-up flow of a yield-stress fluid in a vertical pipe. *Journal of Non-Newtonian Fluid Mechanics*, Elsevier, v. 257, p. 50–58, 2018.

LIU, Y.; KOH, C. M. J.; JI, L. Bioconversion of crude glycerol to glycolipids in ustilago maydis. *Bioresource technology*, Elsevier, v. 102, n. 4, p. 3927–3933, 2011.

LÓPEZ-DURÁN, J.; PÉREZ-GONZÁLEZ, J.; MARÍN-SANTIBÁÑEZ, B.; RODRÍGUEZ-GONZÁLEZ, F. A new method to determine the yield stress of a fluid from velocity profiles in a capillary. *Revista Mexicana de Ingeniería Química*, Universidad Autónoma Metropolitana Unidad Iztapalapa, v. 12, n. 1, p. 121–128, 2013.

LUK, S.; MUTHARASAN, R.; APELIAN, D. Experimental observations of wall slip: tube and packed bed flow. *Industrial & engineering chemistry research*, ACS Publications, v. 26, n. 8, p. 1609–1616, 1987.

MACIEL, A.; SALAS, V.; SOLTERO, J.; GUZMÁN, J.; MANERO, O. On the wall slip of polymer blends. *Journal of Polymer Science Part B: Polymer Physics*, Wiley Online Library, v. 40, n. 4, p. 303–316, 2002.

MACOSKO, C. W.; LARSON, R. G. Rheology: principles, measurements, and applications. Vch New York, 1994.

MAGNIN, A.; PIAU, J. Cone-and-plate rheometry of yield stress fluids. study of an aqueous gel. *Journal of Non-Newtonian Fluid Mechanics*, Elsevier, v. 36, p. 85–108, 1990.

MALKIN, A.; KULICHIKHIN, V.; ILYIN, S. A modern look on yield stress fluids. *Rheologica Acta*, Springer Nature BV, v. 56, n. 3, p. 177–188, 2017.

MALKIN, A. Y. *Rheology fundamentals*. [S.l.]: ChemTec Publishing, 1994.

MARCHESINI, F. H.; ALICKE, A. A.; MENDES, P. R. de S.; ZIGLIO, C. M. Rheological characterization of waxy crude oils: Sample preparation. *Energy & Fuels*, ACS Publications, v. 26, n. 5, p. 2566–2577, 2012.

MEEKER, S. P.; BONNECAZE, R. T.; CLOITRE, M. Slip and flow in pastes of soft particles: Direct observation and rheology. *Journal of Rheology*, The Society of Rheology, v. 48, n. 6, p. 1295–1320, 2004.

MENDES, P. R. de S. Modeling the thixotropic behavior of structured fluids. *Journal of Non-Newtonian Fluid Mechanics*, Elsevier, v. 164, n. 1-3, p. 66–75, 2009.

MENDES, P. R. de S. Thixotropic elasto-viscoplastic model for structured fluids. *Soft Matter*, Royal Society of Chemistry, v. 7, n. 6, p. 2471–2483, 2011.

MENDES, P. R. de S.; THOMPSON, R. L. A unified approach to model elasto-viscoplastic thixotropic yield-stress materials and apparent yield-stress fluids. *Rheologica Acta*, Springer, v. 52, n. 7, p. 673–694, 2013.

MENDES, R.; VINAY, G.; OVARLEZ, G.; COUSSOT, P. Modeling the rheological behavior of waxy crude oils as a function of flow and temperature history. *Journal of Rheology*, SOR, v. 59, n. 3, p. 703–732, 2015.

MEWIS, J.; SPAULL, A. Rheology of concentrated dispersions. *Advances in Colloid and interface Science*, Citeseer, v. 6, n. 3, p. 173–200, 1976.

MITISHITA, R. S.; OLIVEIRA, G. M.; SANTOS, T. G.; NEGRÃO, C. O. Pressure transmission in yield stress fluids-an experimental analysis. *Journal of Non-Newtonian Fluid Mechanics*, Elsevier, v. 261, p. 50–59, 2018.

MITISHITA, R. S. et al. *Avaliação experimental da transmissão de pressão em tubulações preenchidas por fluidos viscoplásticos*. Dissertação (Mestrado) — Universidade Tecnológica Federal do Paraná, 2017.

MOISÉS, G.; ALENCAR, L.; NACCACHE, M.; FRIGAARD, I. The influence of thixotropy in start-up flow of yield stress fluids in a pipe. *Journal of Petroleum Science and Engineering*, Elsevier, v. 171, p. 794–807, 2018.

MØLLER, P.; FALL, A.; BONN, D. Origin of apparent viscosity in yield stress fluids below yielding. *EPL (Europhysics Letters)*, IOP Publishing, v. 87, n. 3, p. 38004, 2009.

MOONEY, M. Explicit formulas for slip and fluidity. *Journal of Rheology (1929-1932)*, The Society of Rheology, v. 2, n. 2, p. 210–222, 1931.

NETO, C.; EVANS, D. R.; BONACCURSO, E.; BUTT, H.-J.; CRAIG, V. S. Boundary slip in newtonian liquids: a review of experimental studies. *Reports on progress in physics*, IOP Publishing, v. 68, n. 12, p. 2859, 2005.

NGUYEN, Q.; BOGER, D. Measuring the flow properties of yield stress fluids. *Annual Review of Fluid Mechanics*, Annual Reviews 4139 El Camino Way, PO Box 10139, Palo Alto, CA 94303-0139, USA, v. 24, n. 1, p. 47–88, 1992.

NIMDEO, Y. M.; JOSHI, Y. M.; MURALIDHAR, K. Refractive index measurement of sol forming laponite js dispersion using interferometry. *Applied Clay Science*, Elsevier, v. 123, p. 272–278, 2016.

NOBACH, H.; BODENSCHATZ, E. Limitations of accuracy in piv due to individual variations of particle image intensities. *Experiments in fluids*, Springer, v. 47, n. 1, p. 27–38, 2009.

NOGUEIRA, J.; LECUONA, A.; RODRIGUEZ, P. Limits on the resolution of correlation piv iterative methods. fundamentals. *Experiments in fluids*, Springer, v. 39, n. 2, p. 305–313, 2005.

OLIVEIRA, G. M. de; NEGRAO, C. O. The effect of compressibility on flow start-up of waxy crude oils. *Journal of Non-Newtonian Fluid Mechanics*, Elsevier, v. 220, p. 137–147, 2015.

OVARLEZ, G.; COHEN-ADDAD, S.; KRISHAN, K.; GOYON, J.; COUSSOT, P. On the existence of a simple yield stress fluid behavior. *Journal of Non-Newtonian Fluid Mechanics*, Elsevier, v. 193, p. 68–79, 2013.

PAGLIARO, M.; ROSSI, M. Glycerol: properties and production. *The future of glycerol*, p. 20–21, 2010.

PALACIOS, F. Estudo experimental do escoamento de fluido newtoaniano em contração abrupta axissimétrica com a técnica de velocimetria por imagem de partículas. *Federal University of Technology-Parana*, 2011.

PASHIAS, N.; BOGER, D.; SUMMERS, J.; GLENISTER, D. A fifty cent rheometer for yield stress measurement. *Journal of rheology*, The Society of Rheology, v. 40, n. 6, p. 1179–1189, 1996.

PEIXINHO, J.; NOUAR, C.; DESAUBRY, C.; THÉRON, B. Laminar transitional and turbulent flow of yield stress fluid in a pipe. *Journal of Non-Newtonian Fluid Mechanics*, Elsevier, v. 128, n. 2-3, p. 172–184, 2005.

PEREIRA, L. G. et al. *Avaliação experimental do reinício de escoamento de fluidos dependentes do tempo em tubulações*. Dissertação (Mestrado) — Universidade Tecnológica Federal do Paraná, 2019.

PÉREZ-GONZÁLEZ, J.; LÓPEZ-DURÁN, J. J.; MARÍN-SANTIBÁÑEZ, B. M.; RODRÍGUEZ-GONZÁLEZ, F. Rheo-piv of a yield-stress fluid in a capillary with slip at the wall. *Rheologica acta*, Springer, v. 51, n. 11-12, p. 937–946, 2012.

PHAM, K.; PETEKIDIS, G.; VLASSOPOULOS, D.; EGELHAAF, S.; PUSEY, P.; POON, W. Yielding of colloidal glasses. *EPL (Europhysics Letters)*, IOP Publishing, v. 75, n. 4, p. 624, 2006.

PIAU, J. Carbopol gels: Elastoviscoplastic and slippery glasses made of individual swollen sponges: Meso-and macroscopic properties, constitutive equations and scaling laws. *Journal of non-newtonian fluid mechanics*, Elsevier, v. 144, n. 1, p. 1–29, 2007.

POUMAERE, A.; MOYERS-GONZÁLEZ, M.; CASTELAIN, C.; BURGHELEA, T. Unsteady laminar flows of a carbopol® gel in the presence of wall slip. *Journal of Non-Newtonian Fluid Mechanics*, Elsevier, v. 205, p. 28–40, 2014.

PRITCHARD, P. J.; MITCHELL, J. W. *Fox and McDonald's Introduction to Fluid Mechanics, Binder Ready Version*. [S.l.]: John Wiley & Sons, 2016.

PUTZ, A. M.; BURGHELEA, T. I. The solid–fluid transition in a yield stress shear thinning physical gel. *Rheologica Acta*, Springer, v. 48, n. 6, p. 673–689, 2009.

RAFFEL, M.; WILLERT, C. E.; SCARANO, F.; KÄHLER, C. J.; WERELEY, S. T.; KOMPENHANS, J. *Particle image velocimetry: a practical guide*. [S.l.]: Springer, 2018.

ROBERT, L.; DEMAY, Y.; VERGNES, B. Stick-slip flow of high density polyethylene in a transparent slit die investigated by laser doppler velocimetry. *Rheologica Acta*, Springer, v. 43, n. 1, p. 89–98, 2004.

ROBERTS, G. P.; BARNES, H. A. New measurements of the flow-curves for carbopol dispersions without slip artefacts. *Rheologica Acta*, Springer, v. 40, n. 5, p. 499–503, 2001.

ROCQUIGNY, E. D.; DEVICTOR, N.; TARANTOLA, S. *Uncertainty in industrial practice: a guide to quantitative uncertainty management*. [S.l.]: John Wiley & Sons, 2008.

RØNNINGSEN, H. P. Rheological behaviour of gelled, waxy north sea crude oils. *Journal of Petroleum Science and Engineering*, Elsevier, v. 7, n. 3-4, p. 177–213, 1992.

RUIZ-VIERA, M.; DELGADO, M.; FRANCO, J.; GALLEGOS, C. Evaluation of wall slip effects in the lubricating grease/air two-phase flow along pipelines. *Journal of Non-Newtonian Fluid Mechanics*, Elsevier, v. 139, n. 3, p. 190–196, 2006.

RYAN, T. P. *Statistical methods for quality improvement*. [S.l.]: John Wiley & Sons, 2011.

SALMON, J.-B.; BÉCU, L.; MANNEVILLE, S.; COLIN, A. Towards local rheology of emulsions under couette flow using dynamic light scattering. *The European Physical Journal E*, Springer, v. 10, n. 3, p. 209–221, 2003.

SCARANO, F.; RIETHMULLER, M. L. Advances in iterative multigrid piv image processing. *Experiments in Fluids*, Springer, v. 29, n. 1, p. S051–S060, 2000.

SCHOWALTER, W. The behavior of complex fluids at solid boundaries. *Journal of Non-Newtonian Fluid Mechanics*, Elsevier, v. 29, p. 25–36, 1988.

SCHRIJER, F.; SCARANO, F. Effect of predictor–corrector filtering on the stability and spatial resolution of iterative piv interrogation. *Experiments in fluids*, Springer, v. 45, n. 5, p. 927–941, 2008.

SCIACCHITANO, A. Uncertainty quantification in particle image velocimetry. *Measurement Science and Technology*, IOP Publishing, v. 30, n. 9, p. 092001, 2019.

SCIACCHITANO, A.; WIENEKE, B.; SCARANO, F. Piv uncertainty quantification by image matching. *Measurement Science and Technology*, IOP Publishing, v. 24, n. 4, p. 045302, 2013.

SETH, J. R.; CLOITRE, M.; BONNECAZE, R. T. Influence of short-range forces on wall-slip in microgel pastes. *Journal of Rheology*, The Society of Rheology, v. 52, n. 5, p. 1241–1268, 2008.

SIERRA, A. G.; VARGES, P. R.; RIBEIRO, S. S. Startup flow of elasto-viscoplastic thixotropic materials in pipes. *Journal of Petroleum Science and Engineering*, Elsevier, v. 147, p. 427–434, 2016.

SOCHI, T. Slip at fluid-solid interface. *Polymer Reviews*, Taylor & Francis, v. 51, n. 4, p. 309–340, 2011.

SOUZA, A. *Fundamentos de Metrologia científica e industrial*. [S.l.]: Editora Manole, SP, 2008.

STAMHUIS, E. J. Basics and principles of particle image velocimetry (piv) for mapping biogenic and biologically relevant flows. *Aquatic Ecology*, Springer, v. 40, n. 4, p. 463–479, 2006.

SZYMANSKI, G. Quelques solutions exactes des équations d'hydrodynamique du fluide visqueux dans le cas d'un tube cylindrique. *Journal de mathématiques pures et appliquées*, v. 11, p. 67–108, 1932.

TAGHAVI, S.; ALBA, K.; MOYERS-GONZALEZ, M.; FRIGAARD, I. Incomplete fluid–fluid displacement of yield stress fluids in near-horizontal pipes: experiments and theory. *Journal of Non-Newtonian Fluid Mechanics*, Elsevier, v. 167, p. 59–74, 2012.

TAKAMURA, K.; FISCHER, H.; MORROW, N. R. Physical properties of aqueous glycerol solutions. *Journal of Petroleum Science and Engineering*, Elsevier, v. 98, p. 50–60, 2012.

TANNER, R. I. *Engineering rheology*. [S.l.]: OUP Oxford, 2000. v. 52.

TASAKA, Y.; KIMURA, T.; MURAI, Y. Estimating the effective viscosity of bubble suspensions in. *Experiments in fluids*, Citeseer, v. 56, p. 1, 1867.

TAYLOR, J. *Introduction to error analysis, the study of uncertainties in physical measurements*. [S.l.: s.n.], 1997.

VISINTIN, R. F.; LAPASIN, R.; VIGNATI, E.; D'ANTONA, P.; LOCKHART, T. P. Rheological behavior and structural interpretation of waxy crude oil gels. *Langmuir*, ACS Publications, v. 21, n. 14, p. 6240–6249, 2005.

WALLS, H.; CAINES, S. B.; SANCHEZ, A. M.; KHAN, S. A. Yield stress and wall slip phenomena in colloidal silica gels. *Journal of Rheology*, The Society of Rheology, v. 47, n. 4, p. 847–868, 2003.

WATSON, G. N. *A treatise on the theory of Bessel functions*. [S.l.]: Cambridge university press, 1995.

WESTERWEEL, J. Fundamentals of digital particle image velocimetry. *Measurement science and technology*, IOP Publishing, v. 8, n. 12, p. 1379, 1997.

WESTERWEEL, J. Theoretical analysis of the measurement precision in particle image velocimetry. *Experiments in Fluids*, Springer, v. 29, n. 1, p. S003–S012, 2000.

WESTERWEEL, J.; DRAAD, A.; HOEVEN, J. T. Van der; OORD, J. V. Measurement of fully-developed turbulent pipe flow with digital particle image velocimetry. *Experiments in Fluids*, Springer, v. 20, n. 3, p. 165–177, 1996.

WESTERWEEL, J.; ELSINGA, G. E.; ADRIAN, R. J. Particle image velocimetry for complex and turbulent flows. *Annual Review of Fluid Mechanics*, Annual Reviews, v. 45, p. 409–436, 2013.

YILMAZER, U.; KALYON, D. M. Slip effects in capillary and parallel disk torsional flows of highly filled suspensions. *Journal of Rheology*, The Society of Rheology, v. 33, n. 8, p. 1197–1212, 1989.

YOUNES, E.; BERTOLA, V.; CASTELAIN, C.; BURGHELEA, T. Slippery flows of a carbopol gel in a microchannel. *Physical Review Fluids*, APS, v. 5, n. 8, p. 083303, 2020.

YOUNES, E.; HIML, M.; STARY, Z.; BERTOLA, V.; BURGHELEA, T. On the elusive nature of carbopol gels:"model", weakly thixotropic, or time-dependent viscoplastic materials? *Journal of Non-Newtonian Fluid Mechanics*, Elsevier, p. 104315, 2020.

APPENDIX A – UNCERTAINTY ANALYSIS

In this experimental study, the concepts of absolute percentage error (APE) were used to determine how close the experimental data were to the theoretical values. Additionally, to measure the dispersion of the data in relation to the mean, the concept of relative standard deviation (RSD) was used. On the other hand, to determine the uncertainties of the measurement instruments and the variables measured, the concepts of type A and type B uncertainties are also used. In the following subsections these concepts are discussed.

A.1 Absolute percentage error

Percent error or absolute percentage error (APE) expresses as a percentage the difference between an approximate or measured value and an exact or known value. It is used in science to report the difference between a measured or experimental value and a true or exact value.

$$APE\% = \left| \frac{x_{theo} - x_{exper}}{x_{theo}} \right| \tag{A.1}$$

A.2 Type A uncertainties of measuring instruments

According to Taylor (1997), the term "error", used in the scientific context, represents the uncertainty associated with each and every one of the measured quantities. These uncertainties, however careful the procedure, cannot be completely eliminated. Therefore, it must be evaluated in what range are the uncertainties associated with the measurement.

A.2.1 Uncertainties of the experimental parameters

In order to calculate type A uncertainties, two types of experimental errors are taken into account: systematic and random. Systematic errors are related to the precision of the measuring instrument and do not vary from test to test. In contrast, random errors can vary with each repetition, being detected through a statistical analysis of the data (TAYLOR, 1997). These errors are caused, for example, by electrical noise affect the acquisition system or human reading error, in the case of an analog instrument. Considering the two sources of error, the value of the total uncertainty of a variable “x” (δx) can be calculated by means of the quadratic sum of the values of the systematic (δx_{sys}) and random (δx_{ran}) uncertainties (TAYLOR, 1997).

$$\delta_x = \sqrt{(\delta x_{sys})^2 + (\delta x_{ran})^2)} \tag{A.2}$$

As mentioned, random errors are verified by statistical analysis of the data. Thus, some concepts are presented such as the arithmetic mean ($\bar{x}$), the standard deviation (σ_x), and the standard error ($\bar{\sigma}_x$) of any variable “x”:

$$\bar{x} = \sum_{i=1}^{N} \frac{x_i}{N} \tag{A.3}$$

$$\sigma_x = \sqrt{\frac{\sum_{i=1}^{N}(x_i - \bar{x})^2}{N}} \tag{A.4}$$

$$\bar{\sigma_x} = \frac{\sigma_x}{\sqrt{N}} \tag{A.5}$$

where N is the total of measurements. Based on the concepts shown, the standard error is adopted as representative of the random uncertainty. That is, the expression that provides the best estimate for a variable that presents only random uncertainties would be: ($x = \bar{x} + C_c \pm \delta x_{ran}$), which can be rewritten as: ($x = \bar{x} + C_c \pm \bar{\sigma_x}$), when C_c is the combined correction (TAYLOR, 1997). According to the above information and with the purpose of determining the uncertainty of the measurement, the steps described below were followed:

1. Analyze the measurement process.
2. Identify sources of uncertainty.
3. Estimate the correction for each source of uncertainty.
4. Calculate the combined correction.
5. Estimate the standard uncertainty for each source of uncertainty.
6. Calculate the combined standard uncertainty and the number of effective degrees of freedom.
7. Calculate the expanded uncertainty.
8. Express the measurement result.

However, due to the data in this study come from tests performed a single measurement, the following question arises: how do you determine and report this uncertainty? According with Taylor (1997) , any measurement you make will have some uncertainty associated with it, no matter the precision of your measuring tool. In consequence, the uncertainty of a single measurement is limited by the precision and accuracy of the measuring instrument, along with any other factors that might affect the ability of the experimenter to make the measurement. Table A.1 presents as an example the calculate performed for one of the variables measured in this study, it is to be assumed that the calculations for the other variables were performed in the same way.

The experimental uncertainty values shown in Tab. A.1 describe the systematic and random errors of the pressure measurement. To compensate for systematic errors, this value is added to the result obtained (see equation in the table). The zero in the description values indicates that the source of uncertainty has no systematic errors. The value of the indication divided by two allows to know the value above

Table A.1 – Type A uncertainties calculated for P_{in} (inlet pressure) P_{out} (outlet pressure) of one of the flow conditions used in the experimental analysis ($\Delta p = 93Pa$ or $\tau_w = 0.43Pa$). Here, (ν) are the degrees of freedom that depend on the type of distribution, (a) is the value of the limitation.

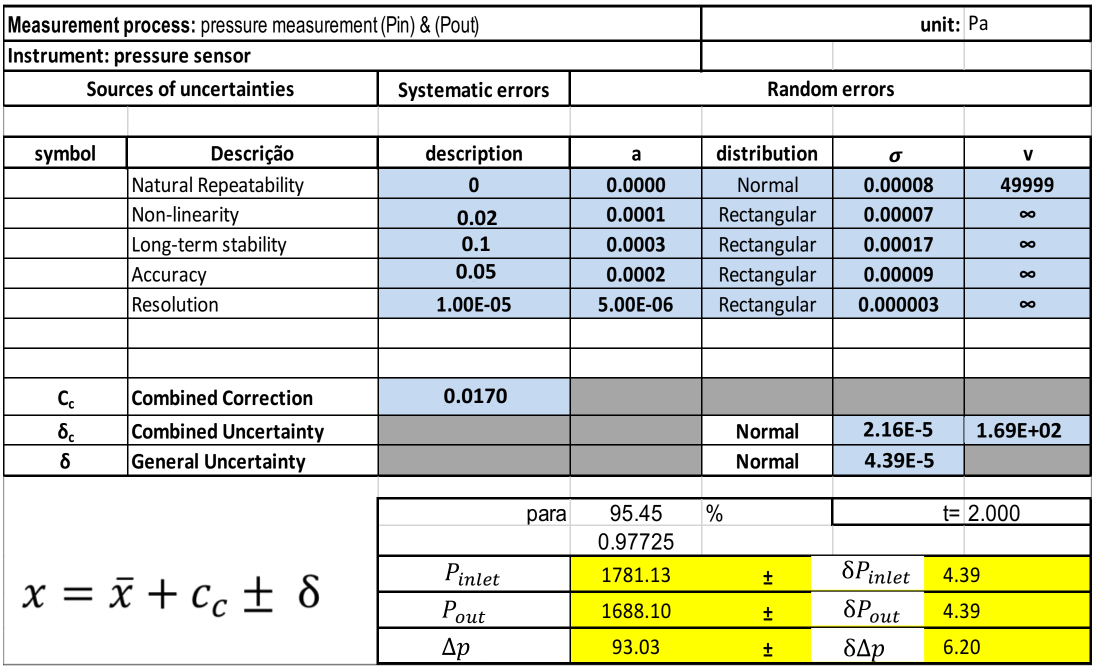

Measurement process: pressure measurement (Pin) & (Pout)					**unit:**	Pa
Instrument: pressure sensor						
Sources of uncertainties		**Systematic errors**	**Random errors**			
symbol	**Descrição**	**description**	**a**	**distribution**	**σ**	**v**
	Natural Repeatability	**0**	**0.0000**	Normal	**0.00008**	**49999**
	Non-linearity	**0.02**	**0.0001**	Rectangular	**0.00007**	**∞**
	Long-term stability	**0.1**	**0.0003**	Rectangular	**0.00017**	**∞**
	Accuracy	**0.05**	**0.0002**	Rectangular	**0.00009**	**∞**
	Resolution	**1.00E-05**	**5.00E-06**	Rectangular	**0.000003**	**∞**
C_c	**Combined Correction**	**0.0170**				
δ_c	**Combined Uncertainty**			**Normal**	**2.16E-5**	**1.69E+02**
δ	**General Uncertainty**			**Normal**	**4.39E-5**	
$x = \bar{x} + c_c \pm \delta$		para	95.45	%	t=	2.000
			0.97725			
		P_{inlet}	1781.13	±	δP_{inlet}	4.39
		P_{out}	1688.10	±	δP_{out}	4.39
		Δp	93.03	±	$\delta \Delta p$	6.20

Source: Author (2021).

and below the measurement. The type of distribution for random errors from natural repeatability was assumed to be normal considering the number of points recorded by the sensors and the other distributions as rectangular, taking into account the sources of uncertainty, are perfectly known values (obtained from the device manual) (SOUZA, 2008). In relation to the degrees of freedom, was considered $(n-1)$ for normal distribution and infinities for a rectangular distribution. The $t-$student coefficient for a reliability interval of 95.45% was calculated as two. The general uncertainty was acquired as 6.20 Pa for the pressure drop and 4.39 Pa for the pressure sensors at the inlet and outlet of the test section. The uncertainty values for the other quantities measured are presented in Tab. A.2.

Table A.2 – Measured parameters and experimental uncertainty values.

Parameter	δ
Temperature [°C]	4.45
Diameter test section [m]	2.23×10^{-4}
Test section length [m]	2.53×10^{-3}

Source: Author (2021).

Finally, the concept of relative standard deviation or percentage relative standard deviation will be used to measure the dispersion of the data around the mean.

If the product comes to a higher relative standard deviation, that means the numbers are very widely spread from its mean. If the product comes lower, then the numbers are closer than its average. It is also knows as the coefficient of variation. The formula for the same is given as:

$$RSD = \frac{\sigma_x}{\bar{x}} \times 100 \tag{A.6}$$

A.2.2 Axial velocity uncertainties

In this subsection, the uncertainty analysis is divided into two parts. The first part discusses the error that the PIV technique introduces in the velocity profiles and that varies as a function of the time between pulses, which is a parameter set to the visualization system. The second part presents an argument to justify that the data obtained from a single experimental test are reliable.

Considering that the velocity of an object is the rate of change of its position with respect to a frame of reference, and is a function of time. Then, it is possible to write this definition in the form of an equation as:

$$u = \frac{\Delta x}{\Delta t} \tag{A.7}$$

whereΔx is the displacement of the object in direction x and Δt is time. Thus, the displacement of the object can be associated with that of the tracer particle that was used to visualize the flow of the pipe in this study and determine the displacement bias error when the size of the particle image is small with respect to the size of the pixel and that it is responsible for measurement errors of up to 0.1 pixels. This phenomenon is known as *peak-locking* (WESTERWEEL, 1997). Then, if pixels are converted to meters, it is obtained that 0.1 pixels is equal to 2.7×10^{-5} meters and Eq. (A.7) can be rewritten as:

$$\delta u = \frac{2.70 \times 10^{-5}}{\Delta t} \tag{A.8}$$

where Δt is the time between pulses. Eq. (A.8) indicates that the uncertainty of the PIV technique due to displacement, at least for the analysis performed in this study, is a function of the time between pulses set for each flow condition (τ_w). Then it is possible to express the general uncertainty of the velocity as:

$$\delta u = \sqrt{(\delta_{u-std})^2 + (\delta_{u-PIV})^2} \tag{A.9}$$

the expression δ_{u-std} is the uncertainty due to the standard deviation of the velocity profiles obtained from three different positions (*Z/D*) and δ_{u-PIV} is generated by the peak-locking. Table A.3 presents the results for the two fluids.

From the data, it is observed that the uncertainties of the fluid C-25 are two orders of magnitude greater for mean velocity values between 3.82×10^{-6} and 2.62×10^{-4}, which it is caused by the very low velocity of the particle and within the resolution of the visualization technique the displacement is practically unmeasurable. This explication is valid also for the fluid C-50. In general, it is observed that a larger time between pulses produces lows uncertainty. On the other hand, the uncertainty data associated with the pressure drops that were calculated in the previous section are also presented, however, they are presented here with the purpose of shows the percentage variation as a function of increase in the pressure drop.

Table A.3 – Uncertainty values of average velocity for different Δp and fluids.

Fluid	Time between pulses [s]	Δp [Pa]	$\delta\Delta p$	$\delta\Delta p\%$	u_{av}[m/s] from PIV	δu_{av}	$\delta u_{av}\%$
C-25	0.00588	93.03	6.20	6.66	3.82E-06	4.61E-04	12070.75
		131.25		4.72	5.59E-05	4.59E-04	822.12
	0.00392	154.14		4.02	1.22E-04	6.89E-04	562.89
		213.71		2.90	2.62E-04	6.89E-04	262.59
	0.0098	314.27		1.97	1.09E-03	2.76E-04	25.20
		423.45		1.46	3.36E-03	2.76E-04	8.19
	0.0784	854.50		0.73	2.86E-02	5.93E-05	0.21
	0.1274	1281.30		0.48	7.66E-02	3.99E-04	0.52
C-50	0.0392	472.06	6.20	1.31	5.61E-05	7.23E-05	128.95
		728.16		0.85	1.43E-04	6.90E-05	48.14
	0.0788	942.69		0.66	2.37E-04	3.46E-05	14.58
		1647.49		0.38	7.11E-04	3.91E-05	5.50
		2933.06		0.21	1.27E-03	3.43E-05	2.70
		5214.40		0.12	4.94E-03	5.87E-05	1.19
		6190.91		0.10	1.22E-02	6.16E-05	0.50
	0.1576	8347.61		0.07	5.05E-02	1.30E-04	0.26
		10460.72		0.06	1.25E-01	2.72E-04	0.22

Source: Author (2021).

Figure A.1 – Velocity profiles obtained under the flow condition given by $\Delta p = 423.45$Pa for the fluid C-25 at three dimensionless times. The velocity profiles are the result of perform the same tests three times. The gray, brown, and orange symbols refer to tests 1, 2, and 3, respectively. The error bars are defined by the square root of the standard deviation of the velocity profiles in three different positions (Z/D) and the error of the PIV technique.

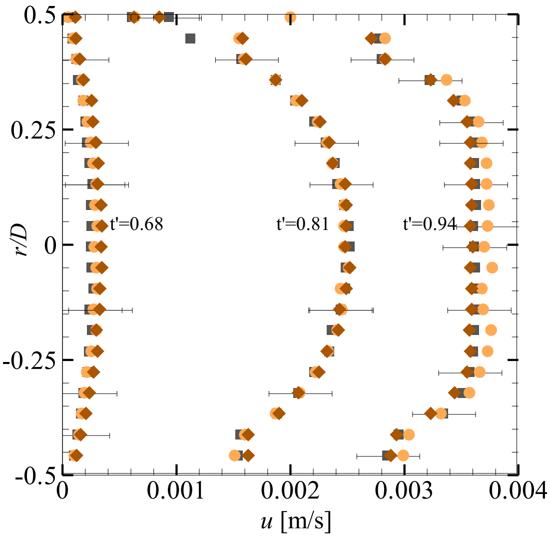

Source: Author (2021).

Attention is now focused on the argument related to the fact that the data obtained from a single test in this study are sufficiently reliable to be considered valid. For this purpose, we performed two analyzes, the first related to the velocity profiles obtained by the PIV technique and the other based on the recorded pressure drop data. Figure A.1 presents the velocity profiles obtained for the flow condition given by the pressure drop Δp=423.45 Pa measured three times. The results show a good agreement between the three tests, evidenced by the overlap of the velocity profiles, being more evident for t'=0.81. However, in order

Table A.4 – Relative standard deviation, mean and 95% confidence interval for profiles velocity at t'=0.68.

Test No.1	Test No. 2	Test No. 3	Confidence interval			Relative standard deviation RSD [%]
u [m/s]	u [m/s]	u [m/s]	Lower limit	Mean	Upper limit	
1.84E-04	1.93E-04	2.36E-04	1.52E-04	2.05E-04	2.34E-04	13.49
2.19E-04	2.13E-04	2.73E-04	1.70E-04	2.35E-04	2.68E-04	14.02
2.30E-04	2.52E-04	3.07E-04	1.93E-04	2.63E-04	3.12E-04	15.19
2.57E-04	2.96E-04	2.97E-04	2.52E-04	2.84E-04	3.30E-04	8.03
2.35E-04	2.71E-04	3.26E-04	2.03E-04	2.78E-04	3.39E-04	16.44
2.72E-04	3.04E-04	3.28E-04	2.62E-04	3.01E-04	3.46E-04	9.31
2.53E-04	2.96E-04	3.45E-04	2.27E-04	2.98E-04	3.65E-04	15.53
2.49E-04	2.79E-04	3.39E-04	2.11E-04	2.89E-04	3.47E-04	15.81
2.52E-04	3.05E-04	3.46E-04	2.34E-04	3.01E-04	3.75E-04	15.79
2.47E-04	2.85E-04	3.38E-04	2.17E-04	2.90E-04	3.54E-04	15.85
2.63E-04	2.95E-04	3.08E-04	2.60E-04	2.89E-04	3.30E-04	8.13
2.37E-04	2.68E-04	3.15E-04	2.10E-04	2.73E-04	3.26E-04	14.28
2.14E-04	2.46E-04	2.93E-04	1.87E-04	2.51E-04	3.05E-04	15.82
2.00E-04	2.18E-04	2.67E-04	1.66E-04	2.29E-04	2.70E-04	15.25
1.83E-04	1.82E-04	2.56E-04	1.19E-04	2.07E-04	2.46E-04	20.51
1.34E-04	1.71E-04	1.85E-04	1.32E-04	1.63E-04	2.10E-04	15.96

Source: Author (2021).

to show statistical evidence of the repeatability of the tests, the relative standard deviation (RSD) of the velocity profiles was calculated for each dimensionless time. In addition, the definition of the confidence interval was used to estimate a range of values and the probability within which the obtained data are found. The statistical results are shown in Tab. A.4, A.5, and A.6 .

The statistical analysis shows that the mean of the relative standard deviation of the velocity profiles for t'=0.64 is 15.39%, this value is considered "high" when compared with the RSD of t'=0.81 and t'=0.94, where it is equal to 0.83% and 1.83%, respectively. The possible causes of a high RSD in the early times are possibly due to velocity fluctuations (a phenomenon explained in 3), *peak-locking*, among others. However, this error can be considered acceptable (RYAN, 2011) considering the precision of the visualization technique used. On the other hand, the confidence intervals allowed estimate with a probability of 95% that the values of the velocity profiles were within the statistical limits calculated. In simple terms, the confidence interval indicated that the sample values are in a certain range of values with 95% certainty.

In order to complement this analysis, Fig. A.2 presents the evolution of the pressure drop applied to obtain the velocity profiles. As in Fig. A.1, it is observed that the data overlap during the transient increase of the pressure. The statistical evaluation of the data shows that all the values are within a confidence interval of 95% and the mean relative standard deviation is 4.96%, considered as an acceptable error (RYAN, 2011). Table A.7 presents the results obtained, but only 20 data because for each test performed there are more than four thousand measured points and it is impractical to place such a large number of values in the text. Finally, and based on the tests carried out and the statistical analysis presented, it can be concluded that the results obtained from a single test are consistent and can be considered valid.

Table A.5 – Relative standard deviation, mean and 95% confidence interval for profiles velocity at t'=0.81.

Test No.1	Test No. 2	Test No. 3		Confidence interval		Relative standar deviation RSD [%]
u [m/s]	u [m/s]	u [m/s]	Lower limit	Mean	Upper limit	
2.07E-03	2.08E-03	2.07E-03	2.07E-03	2.08E-03	4.15E-03	0.33
2.21E-03	2.22E-03	2.25E-03	2.20E-03	2.23E-03	4.43E-03	1.09
2.34E-03	2.33E-03	2.32E-03	2.32E-03	2.33E-03	4.64E-03	0.43
2.36E-03	2.41E-03	2.42E-03	2.36E-03	2.40E-03	4.76E-03	1.36
2.44E-03	2.45E-03	2.43E-03	2.42E-03	2.44E-03	4.87E-03	0.57
2.48E-03	2.44E-03	2.49E-03	2.44E-03	2.47E-03	4.91E-03	1.10
2.48E-03	2.51E-03	2.52E-03	2.48E-03	2.50E-03	4.98E-03	0.95
2.52E-03	2.47E-03	2.48E-03	2.46E-03	2.49E-03	4.95E-03	0.96
2.51E-03	2.47E-03	2.49E-03	2.47E-03	2.49E-03	4.96E-03	0.72
2.47E-03	2.47E-03	2.49E-03	2.46E-03	2.48E-03	4.93E-03	0.54
2.41E-03	2.44E-03	2.48E-03	2.40E-03	2.44E-03	4.85E-03	1.40
2.39E-03	2.37E-03	2.37E-03	2.36E-03	2.37E-03	4.74E-03	0.41
2.31E-03	2.32E-03	2.34E-03	2.30E-03	2.32E-03	4.63E-03	0.61
2.21E-03	2.24E-03	2.26E-03	2.21E-03	2.24E-03	4.45E-03	1.06
2.04E-03	2.05E-03	2.10E-03	2.03E-03	2.06E-03	4.09E-03	1.43
1.87E-03	1.87E-03	1.87E-03	1.86E-03	1.87E-03	3.73E-03	0.20

Source: Author (2021).

Table A.6 – Relative standard deviation, mean and 95% confidence interval for profiles velocity at t'=0.94.

Test No.1	Test No. 2	Test No. 3		Confidence interval		Relative standar deviation RSD [%]
u [m/s]	u [m/s]	u [m/s]	Lower limit	Mean	Upper limit	
3.51E-03	3.57E-03	3.44E-03	3.43E-03	3.51E-03	6.94E-03	1.94
3.57E-03	3.66E-03	3.55E-03	3.53E-03	3.59E-03	7.12E-03	1.64
3.60E-03	3.73E-03	3.58E-03	3.54E-03	3.63E-03	7.17E-03	2.26
3.61E-03	3.76E-03	3.57E-03	3.54E-03	3.65E-03	7.18E-03	2.67
3.65E-03	3.69E-03	3.59E-03	3.59E-03	3.64E-03	7.23E-03	1.38
3.61E-03	3.68E-03	3.59E-03	3.57E-03	3.63E-03	7.20E-03	1.39
3.62E-03	3.77E-03	3.58E-03	3.54E-03	3.66E-03	7.20E-03	2.74
3.61E-03	3.70E-03	3.60E-03	3.57E-03	3.64E-03	7.21E-03	1.57
3.60E-03	3.73E-03	3.58E-03	3.54E-03	3.63E-03	7.18E-03	2.20
3.63E-03	3.74E-03	3.59E-03	3.57E-03	3.65E-03	7.22E-03	2.11
3.62E-03	3.72E-03	3.59E-03	3.57E-03	3.64E-03	7.21E-03	1.82
3.61E-03	3.72E-03	3.58E-03	3.55E-03	3.63E-03	7.19E-03	1.95
3.62E-03	3.68E-03	3.58E-03	3.57E-03	3.63E-03	7.20E-03	1.33
3.58E-03	3.65E-03	3.55E-03	3.54E-03	3.59E-03	7.13E-03	1.38
3.50E-03	3.53E-03	3.43E-03	3.42E-03	3.49E-03	6.91E-03	1.55
3.22E-03	3.37E-03	3.23E-03	3.18E-03	3.27E-03	6.46E-03	2.47

Source: Author (2021).

Table A.7 – Relative standard deviation, mean and 99% confidence interval for pressure drop (Δp).

Test No.1	Test No. 2	Test No. 3	Confidence interval			Relative standar deviation RSD [%]
Δp [Pa]	Δp [Pa]	Δp [Pa]	Lower limit	Mean	Upper limit	
30.30	17.80	9.70	7.52	19.27	31.01	53.86298
52.80	35.80	24.20	21.32	37.60	53.88	38.25722
198.00	179.70	166.90	163.85	181.53	199.22	8.610455
207.10	189.30	181.90	178.11	192.77	207.42	6.719385
227.70	209.60	207.30	202.22	214.87	227.51	5.200123
235.90	219.90	218.90	214.11	224.90	235.69	4.241615
300.30	285.50	307.50	285.07	297.77	310.46	3.766927
314.50	307.30	332.70	303.35	318.17	332.98	4.114499
343.50	335.00	368.30	329.35	348.93	368.51	4.958575
411.30	410.30	431.60	404.13	417.73	431.33	2.877264

Source: Author (2021).

Figure A.2 – Evolution of the pressure drop for a fluid C-25 as a function of dimensionless time when a $\Delta p = 423.45$Pa is applied and repeated three times. The error bars are defined as the square root of the standard deviation between the three tests and the error of the pressure sensors.

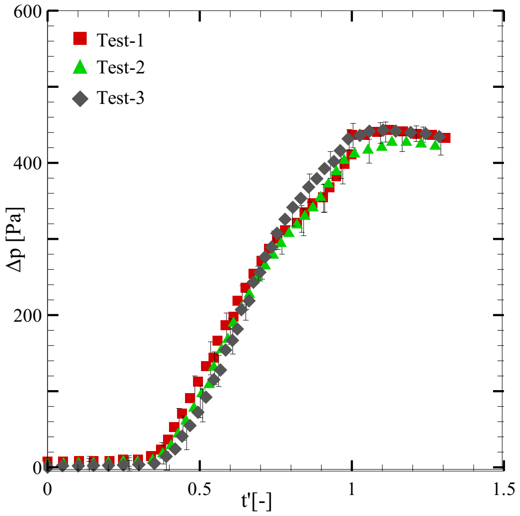

Source: Author (2021).

A.2.3 Uncertainties of the PIV methodology validation

Using Eq. (A.7), Table A.8 presents the δu corresponding to the velocity profiles plotted in the validation of the PIV methodology (Fig. 5.1). From the results it is possible to perceive that δu has the same order of magnitude for the three flow conditions studied and the percentage of δu with respect to U_{max} does not exceed 3%, which can be considered low and within the framework of the studied phenomenon the PIV technique can be used.

On the other hand, to verify the relationship between the experimental and theoretical data, the relative standard deviation was calculated. The results show a good agreement where the %RSD value does not exceed 13% for all the pressure drops and dimenensionless time analyzed (TABLE A9).

A.3 Type B uncertainties of measuring instruments

Based on the definition given by section 4.3.4.4, this appendix presents the calculations for type B uncertainties.

A.3.1 Measurement of wall shear stress and derived uncertainties

Using the methodology described in subsection 4.3.5.2 and Eq. 2.18 for the wall shear stress, it is possible to calculate the uncertainty ($\delta\tau_w$) for this variable. Then, Eq. 2.18 can be rewritten as a function of the diameter:

$$\tau_w = \frac{\Delta p D}{4L} \tag{A.10}$$

where (Δp) is the pressure drop, (L) is the length between the pressure sensors, and (D) is the diameter of the pipe. Using the Eq. 4.7, the uncertainty of τ_w is given by:

$$(\delta\tau_w)^2 = \left(\frac{\partial\tau_w}{\partial\Delta p}\right)^2 (\delta\Delta p)^2 + \left(\frac{\partial\tau_w}{\partial D}\right)^2 (\delta D)^2 + \left(\frac{\partial\tau_w}{\partial L}\right)^2 (\delta L)^2 \tag{A.11}$$

$\delta\Delta p$, δD y δL, are the uncertainties for the measurement of pressure drop, pipe diameter, and length, respectively. Finding the partial derivative of Eq. A.10 for each variable and substituting in Eq. A.12, a new expression for $\delta\tau_w$ is obtained:

Table A.8 – Uncertainty values of δu and RSD for different Δp and dimensionless times.

ΔP [Pa]	R_e	Time between pulses [s]	δu [m/s]	Dimensionless time [t']	U_{max} [m/s]	δu [%]	RSD [%]
1977.9	1	0.1365	1.97×10^{-4}	0.55	8.28×10^{-3}	2.39	4.74
				0.74	2.34×10^{-2}	0.84	5.63
				0.81	4.45×10^{-2}	0.44	3.54
				1.2	6.09×10^{-2}	0.32	6.88
4683.7	2	0.1651	1.65×10^{-4}	0.55	9.65×10^{-3}	1.71	8.52
				0.74	3.70×10^{-2}	0.45	3.68
				0.81	7.35×10^{-2}	0.22	12.93
				1.2	1.43×10^{-1}	0.11	4.10
7430.9	4	0.1357	1.99×10^{-4}	0.55	3.18×10^{-2}	0.63	2.27
				0.74	6.43×10^{-2}	0.31	4.33
				0.81	1.15×10^{-1}	0.17	3.17
				1.2	2.13×10^{-1}	0.09	2.31

Source: Author (2021).

$$(\delta\tau_w)^2 = \left(\frac{D}{4L}\right)^2 (\delta\Delta p)^2 + \left(\frac{\Delta p}{4L}\right)^2 (\delta D)^2 + \left(\frac{-\Delta p D}{4L^2}\right)^2 (\delta L)^2 \tag{A.12}$$

Solving Eq. A.12 for the square root, the equation to calculate the uncertainty of the wall shear stress is obtained as:

$$\delta\tau_w = \sqrt{\left(\frac{D}{4L}\right)^2 (\delta\Delta p)^2 + \left(\frac{\Delta p}{4L}\right)^2 (\delta D)^2 + \left(\frac{-\Delta p D}{4L^2}\right)^2 (\delta L)^2} \tag{A.13}$$

Table A.9 summarizes the values obtained for $\delta\tau_w$. As a general observation, the uncertainty values increase as the wall shear stress values increases, while the percentage uncertainty decreases, which is to be expected because the value of the error percentage compared to the applied shear stress value is low.

Table A.9 – Uncertainty values of τ_w for different flow conditions and fluids.

Fluids	Average Shear Stress τ_w [Pa]	$\delta\tau_w$ [Pa]	$\delta\tau_w\%$
C-25	0.43	0.039	9.20
	0.62	0.040	6.40
	0.80	0.040	5.01
	1.02	0.041	4.05
	1.50	0.044	2.91
	2.03	0.047	2.32
	4.10	0.067	1.63
	6.15	0.088	1.44
C-50	2.30	0.038	1.66
	3.34	0.046	1.39
	4.30	0.056	1.30
	7.92	0.088	1.11
	14.09	0.148	1.05
	25.05	0.262	1.05
	29.74	0.304	1.02
	40.10	0.418	1.04
	50.25	0.512	1.02

Source: Author (2021).

A.3.2 Apparent shear rate uncertainties

The apparent shear rate is another quantity to which uncertainty must be calculated. As it depends on the volumetric flow rate, the following expression can be written:

$$\delta\dot{\gamma_{app}} = \sqrt{\left(\frac{\delta Q}{Q}\right)^2 + \left(\frac{-3\delta D}{D}\right)} \tag{A.14}$$

where Q is calculated as a function of the average velocity through $Q = \bar{U}\pi R^2$. The uncertainty related to the apparent shear rate is shown in Tab. A.10. From the data it is observed that the $\delta\dot{\gamma}_{app}\%$ values practically remains constant for the flow conditions of the fluid C-50, this fact may be related to the fact that the volumetric flow rates are very low, the same behavior was perceived for the fluid C-25.

A.4 PIV uncertainty

The error associated with the acquisition of images can be calculated using the definition described in section 4.3.5.3 for flow in steady-state or fully developed regime (WESTERWEEL et al., 1996). Therefore, due to the fact that the phenomenon analyzed in this study is transient nature, the data obtained lack a sufficient number of independent images necessary to produce reasonable average statistics. For this reason, the uncertainty analysis given in A.2.2 presented a better appreciation of the effect of the errors of the PIV technique in the evaluated problem. However, as within the investigation performed, two

Table A.10 – Uncertainty values of τ_w for different flow conditions and fluids.

Fluid	$\dot{\gamma}_{app}$	$\delta\dot{\gamma}_{app}$	$\delta\dot{\gamma}_{app}\%$
C-25	0.0014	2.03E-05	1.46
	0.02	2.07E-05	0.10
	0.04	3.18E-05	0.07
	0.10	3.70E-05	0.04
	0.40	8.97E-05	0.02
	1.22	2.74E-04	0.02
	10.39	2.32E-03	0.02
	27.86	6.23E-03	0.02
C-50	0.02	5.55E-06	0.03
	0.05	1.20E-05	0.02
	0.09	1.93E-05	0.02
	0.26	5.78E-05	0.02
	0.46	1.03E-04	0.02
	1.80	4.02E-04	0.02
	4.44	9.92E-04	0.02
	18.35	4.10E-03	0.02
	45.35	1.01E-02	0.02

Source: Author (2021).

flow conditions reached the condition of fully developed, the corresponding analysis is presented below, following the steps:

1. Define measurement time.

$$M_t = \frac{X_D N_T}{\bar{U}} \tag{A.15}$$

2. Calculate the integral time scale

$$I_t = \frac{D}{\bar{U}} \tag{A.16}$$

3. Obtain the sampling error

$$e_s = \frac{1}{\sqrt{\frac{M_t}{I_t}}} \tag{A.17}$$

Table A.11 presents the error due to the acquisition of images for the two fluids used. It is observed that the sampling error is slightly higher for the fluid C-25 compared to the fluid C-50, which is strange because if the sampling error depends on the visualization region, and for both fluids X_D and D are the same, the error would be expected to be the same. Therefore, it is possible to say that not only the geometric aspect influences the error value, but also the number of images (WESTERWEEL et al., 1996).

Table A.11 – Values obtained for M_t, I_t, and e_s as a function of the wall shear stress for the viscoplastic fluids C-25 and C-50.

Fluid	Δp [Pa]	τ_w [Pa]	$\bar{U}$ [m/s]	M_t [s]	I_t [s]	e_s [%]
C-25	1281.30	6.15	0.077	835.89	0.29	1.85
C-50	10460.72	50.25	0.12	880.35	0.18	1.42

Source: Author (2021).